A Wideband Direction of Arrival Technique for Multibeam, Wide-Swath Imaging of Ice Sheet Basal Morphology

By

Theresa Stumpf

Submitted to the graduate degree program in Electrical Engineering and Computer Science and the Graduate Faculty of the University of Kansas in partial fulfillment of the requirements for the degree of Master of Science.

_____

Chairperson: Prasad Gogineni

_____

John Paden

_____

Carl Leuschen

Date Defended: 6 July 2015

The Thesis Committee for Theresa Stumpf

certifies that this is the approved version of the following thesis:

A Wideband Direction of Arrival Technique for Multibeam Wide-Swath Imaging of Ice Sheet Basal Morphology

_____

Chairperson: Prasad Gogineni

Date approved: 6 July 2015

Abstract

Multichannel, ice sounder data can be processed to three-dimensionally map ice sheet bed topography and basal reflectivity using tomographic imaging techniques. When ultra-wideband (UWB) signals are used to interrogate a glaciological target, fine resolution maps can be obtained. These data sets facilitate both process studies of ice sheet dynamics and also continental-scale ice sheet modeling needed to predict future sea level. The socioeconomic importance of these data as well as the cost and logistical challenge of procuring them justifies the need to image ice sheet basal morphology over a wider swath. Imaging wide swaths with UWB signals poses challenges for the array processing methods that have been used to localize scattering in the cross-track dimension. Both MUltiple SIgnal Classification (MUSIC) and the Maximum Likelihood Estimator (MLE) have been applied to the ice sheet tomography problem. These techniques are formulated assuming a narrowband model of the array that breaks down in wideband signal environments when the direction of arrival (DOA) increases further off nadir.

The Center for Remote Sensing of Ice Sheets (CReSIS) developed a UWB multichannel SAR with a large cross-track array for sounding and imaging polar ice from a Basler BT-67 aircraft. In 2013, this sensor collected data in a multibeam mode over the West Antarctic Ice Sheet to demonstrate wide swath imaging. To reliably estimate the arrival angles of echoes from the edges of the swath, a parametric space-time direction of arrival estimator was developed that obtains an estimate of the DOA by fitting the observed space-time covariance structure to a model. This thesis focuses on the development and optimization of the algorithm and describes its predicted performance based on simulation. Its measured performance is analyzed with 3D tomographic basal maps of an ice stream in West Antarctica that were generated using the technique.

Table of Contents

List of Figures

List of Symbols

Symbol	Description
u	Along-track position of measurement
ρ	Range to target
θ	Direction of arrival of a single source
$[\hat{\mathbf{x}}_{FCS}, \hat{\mathbf{y}}_{FCS}, \hat{\mathbf{z}}_{FCS}]^T$	Basis of SAR flight coordinate system
$\Delta\rho$	Range resolution
BW	Bandwidth of received chirp
α	Window widening factor that describes the coarsening of range resolution when a frequency domain window is applied during pulse compression,
c	Speed of light
N_t	Number of fast-time samples in a complex SAR image
N_a	Number of along-track samples in a complex SAR image
N_s	Number of sources impinging on array (taken to be the number of distinct scattering patches contributing to a pixel in the SAR image)
$\mathbf{x_m}(n) \in \mathbb{C}^{N_t \times 1}$	The n^{th} entry of a complex valued vector of N_t elements corresponding to an arbitrary column of the SAR image $\mathbf{X_m}$
M	Number of cross-track measurements available for array processing
θ_{bed}	Arrival angle of a scattering patch at the ice-bed interface
ϕ_{HP}	Half power beamwidth of antenna
$\mathbf{r}_m$	Position vector of m^{th} antenna measured with respect to some origin on the array
K	Snapshots
f_s	Sampling frequency
f_0	Start frequency of transmit chirp
f_1	Stop frequency of transmit chirp
$\tau_m(\theta_i)$	Delay of a signal arriving from direction θ_i between the reference of the array and the m^{th} receiver
$\tau_{k,l}(\theta_i)$	Interelement delay between the k^{th} and l^{th} sensors due to a signal from θ_i defined as $\tau_l(\theta_i) - \tau_k(\theta_i)$
$\hat{\theta}_i$	Estimated arrival angle of i^{th} source

$\widehat{\boldsymbol{\Theta}} = [\hat{\theta}_1, \ldots, \hat{\theta}_{N_s}]$	$N_s \times 1$ vector of estimates
N_b	Number of sub bands
$H(f)$	Frequency domain windowing used in pulse compression (typically Hanning)

Chapter 1

Introduction

1.1 Motivation

Over the last decade, both ICESat and IceBridge altimetry and gravimetry data from GRACE have revealed increases in mass loss from the Greenland and West Antarctic ice sheets [1]. This thinning coincides with rapid changes being observed at the margins and raises practical socioeconomic concerns for the contributions of the large ice sheets to future sea level. Sea level rose approximately 1.5 cm over the last century. It is expected to continue rising over the next century but the projections in global mean sea level by the year 2,100 range from 25 cm to more than 95 cm [2]. Because policymakers rely on these predictions to pass legislation that will mitigate the risks associated with rising sea levels, reducing the uncertainty in these estimates is a key factor in protecting the large concentrations of communities and national assets residing in coastal regions.

The largest source of uncertainty in ice sheet modeling is attributed to dynamics. To accurately model ice flow, scientists need to know information about the underlying bed both in shape and composition. Pinning points, slopes, grounding lines, subglacial channels and the presence or absence of water all determine how ice will flow from the interior out to the margins. Multichannel ice-penetrating synthetic aperture radars (SARs) are capable of three dimensionally mapping ice bed topography and basal reflectivity with very fine resolution. Managing the socioeconomic impacts of sea level rise over the next century hinges on the scientific community's ability to reliably predict the responses of the large ice sheets to warming. The importance of the data required by scientists to improve ice-sheet models for more accurately forecasting future sea levels justifies the need to map these parameters over large extents [3].

1.2 The Radar Depth Sounder/Imager

The Center for Remote Sensing of Ice Sheets (CReSIS) relies on a Multichannel Coherent Radar Depth Sounder/Imager (MCoRDS/I) for profiling ice sheet thickness and mapping ice sheet basal characteristics. Developed by CReSIS researchers at the University of Kansas, this sensor is operable over the Very High Frequency (VHF) range as well as P-Band with varying resolution and has been integrated onto a number of airborne platforms each with a distinct cross-track array.

Over time, improvements to this system have enabled operation over wider bandwidths and with larger cross-track apertures both of which provide more detailed information about the basal properties of an ice sheet. Increases in the bandwidth of the illuminating signal and increases in the cross-track aperture size both allow bottom topography and reflectivity to be mapped in finer detail. Additionally if the bandwidth is made large enough, the dielectric properties of the bed may be estimated to determine characteristics of the materials at the ice bed interface that influence ice sheet dynamics.

While wider bandwidths and wider arrays serve to increase the scientific utility of the radar, they pose new challenges in the array processing needed to estimate the geophysical properties of interest. Parametric signal processing techniques offer finer angular resolution than Fourier imaging methods for localizing scatterers across the track. The use of these algorithms is desirable for imaging a wide swath in a single pass. This is because without displacing the phase center on transmit, the resolution of the conventional matched filter is limited by the length of the cross-track array whose geometry must work within the confines of the airborne platform. Parametric signal processing is traditionally formulated based on a narrowband model which does not accurately describe the wideband signal used by the wider bandwidth versions of MCoRDS/I.

1.3 Scope

The challenges that arise in ultra-wideband, wide-swath imaging of ice sheet basal morphology are addressed as a part of this thesis. The research undertaking that is summarized here has focused on improving array processing methods needed to generate tomographic basal maps of several ice streams in West Antarctica using wide swath data from CReSIS's ultra-wideband (UWB) depth sounder/imager. In particular a wideband direction of arrival (WDOA) method was developed to handle imaging at the larger incidence angles. This thesis gives an overview of the use of multibeam configurations for imaging a wide swath and offers a detailed description of wideband imaging geometries. The array theory needed to formulate the direction of arrival problem is provided and a discussion of existing wideband approaches is

also presented. The algorithm is presented in Chapter 3 as the major portion of the methodology. Simulations are used to predict the performance in simplified scattering scenarios in Chapter 4. In Chapter 5, results are presented from the 2013 Antarctic mission during which the UWB radar depth sounder/imager collected wide swath data in a multibeam, high altitude configuration. This thesis closes with recommendations and possible improvements for future work.

Chapter 2

Background and Theory

MCoRDS/I is used both for measuring ice thickness and for swath imaging of ice sheet basal morphology [4]. This work focuses on the former application and in particular presents a new array processing strategy for handling the challenges that emerge when the ultra-wideband (UWB) version of MCoRDS/I is used to map the subsurface of polar ice over a large area with finer resolution. This chapter sets up the geometry and array theory needed to derive the direction of arrival (DOA) estimator used herein.

2.1 Multibeam, Wide-Swath Imaging

To image a wider swath the footprint of the transmit antenna must increase so that a larger area is illuminated as the platform traverses the scene. The engineering challenge that is often associated with wide-swath imaging is a trade-off between Doppler resolution and swath width that arises when the maximum unambiguous range increases to capture returns from the edges of the swath thereby forcing the Doppler sampling to degrade [5]. This however is not the issue in mapping the ice bed over large extents. Rather the specific concern for our application is accurately measuring the arrival angle of weak bed echoes at the edges of swath, especially when they compete with surface clutter. The performance of the DOA estimators used to measure arrival angle is heavily dependent on the signal-to-noise ratio (SNR) of the received signal as documented in literature [6]. This is also shown through simulation in Chapter 4. For this reason any transmit beamforming strategy that degrades SNR is clearly undesirable (for both sounding and imaging).

A larger footprint can be obtained by transmitting a single broad beam but this is not the preferred solution for several reasons. Creating the broader beam would require transmitting on fewer elements. Without increasing the transmit power per element this approach would compromise the coherent gain of the array, thereby reducing the SNR of the basal returns. To implement this would require changes to

existing hardware which may not be practical so an approach that uses the existing system configuration would be preferred. But even if we were not required to implement something within the current hardware framework, the use of a single broad transmit beam would still not be the most desirable way to cover a larger swath. This is because the combination of a wide transmit beam and a narrow receive beam has undesirable isolation properties that can degrade the signal-to-clutter ratio (SCR) of our cross-track measurements. For any radar, SNR is directly related to the power-aperture product. The use of a small aperture to detect weak targets must be compensated with a corresponding increase in transmit power. The generation of high peak powers, even with pulse compression, is extremely difficult to accomplish with the limited funds available for building radar systems at a university for civilian applications such as ice-sheet sounding and imaging.

Instead, wide-swath imaging is realized by operating MCoRDS/I from high altitude and using the full array to cover the swath with multiple narrow beams that are scanned over the effective pulse interval. During the 2013 field season in Antarctica, the UWB depth sounder was run in multibeam mode from approximately 1.8 km above ground level (the maximum allowable altitude for operating a BT-67 aircraft without oxygen masks), over several ice streams, including Kamb and Whillians that drain ice from the West Antarctic Ice Sheet. In the multibeam configuration, three beams were scanned over the swath during a pulse interval to increase the footprint at the ice-bed interface. The look angles for the sidelooking beams were ±20°. The beams of an effective pulse interval are illustrated in the cross-track plane in the figure below.

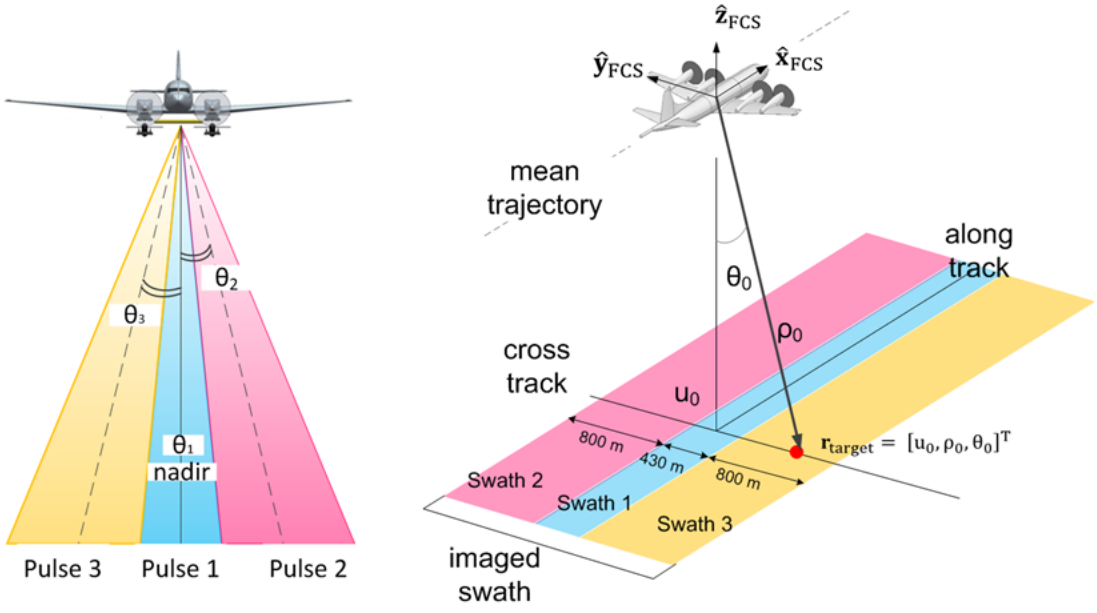

Figure 2-1 Transmit beams and imaged swaths in multibeam mode

The corresponding subswaths of the total imaged swath are also presented with effective swath widths at the ice-bed interface assuming a height above surface of 1.8 km and an ice thickness of 600 m (chosen as a typical value for the surveyed areas that were studied for this project). The geometry in this example shows how the sidelooking beams facilitate imaging over a larger extent. The footprint of the sounding beam is 430 m at the ice-bed interface while the footprint of one of the sidelooking beams is 800 m. The total illuminated area that echoes back from within the half power beamwidth of the antenna (taken to be 20°) is 2.03 km which is more than four times wider than the illumination footprint in sounding mode.

2.2 3D Imaging Problem Formulation

Tomographic processing enables a multichannel airborne SAR to image the spatial distribution of an extended target's reflectivity in three dimensional space. The tomographic formulation for fine resolution terrain mapping dates back as early as 1983 [7]. Examples of the tomographic technique for imaging subsurface targets have also been demonstrated in the literature for evaluating the structural integrity of bridges [8] [9]. The tomographic technique involves 1) the formation of a 3D image of a body from a stack of its 2D slices and 2) extraction of a surface from that 3D image. Each slice is obtained by applying array processing to a set of cross-track pixels taken from the SAR images formed from each channel.

2.2.1 Imaging Geometry

The 3D imaging geometry used to formulate the SAR tomography problem is shown in Figure 2-1 for a point target, shown in red at a range ρ_0 and at an angle θ_0 off nadir, at along track position u_0[1]. The platform coordinate system is specified using the SAR flight coordinate system where $\hat{\mathbf{x}}_{\mathrm{FCS}}$ points along the mean trajectory, $\hat{\mathbf{z}}_{\mathrm{FCS}}$ is the elevation up vector projected orthogonal to $\hat{\mathbf{x}}_{\mathrm{FCS}}$ and $\hat{\mathbf{y}}_{\mathrm{FCS}}$ completes the right handed coordinate system. After SAR processing, the scene is uniformly sampled in slant range and along-track. Targets are assumed to be focused to their zero-Doppler positions along range shells with thickness $\Delta\rho = \alpha\frac{c}{2BW}$, where c is the speed of light, BW is the bandwidth of the illuminating pulse, and α is a widening factor used to describe the broadening of the range resolution element relative to a rectangular window[2].

The tomography problem then reduces to the 2D geometry of the y-z or cross-track plane shown in Figure 2-2. Scattering from the red point target maps to the pixel associated with the (u_0, ρ_0) pair associated

[1] The scalar variable u is used instead of x to denote the position along the track and x is reserved as a data variable. Later the vector **u** is used to describe the directional cosines vector and shouldn't be confused with along-track position.

[2] Typically, a Hanning window is applied in pulse compression. In this case, α = 1.62.

with the range shell highlighted in gray. The missing coordinate that is needed for 3D localization of the scatter is the angle of arrival, θ_0, obtained through array processing provided that the number of cross-track measurements is greater than the number of targets. In the absence of a DOA measurement, targets with the same (u, ρ) coordinates are not resolvable.

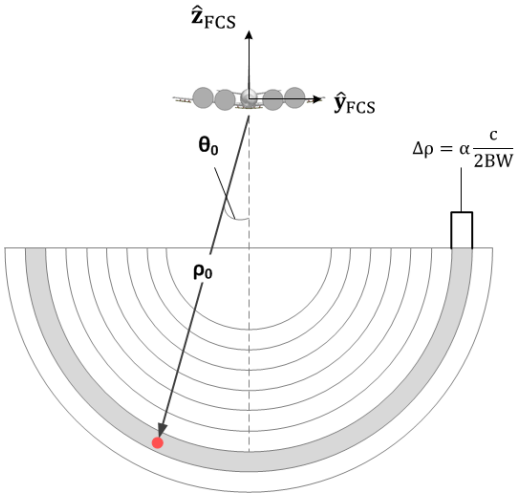

Figure 2-2 Cross-track geometry used to formulate the 3D imaging problem of a point target

2.2.2 Scattering Order of Pixels

In the application of imaging terrain, we are interested in three-dimensionally locating echoes from scattering patches along an extended surface. Each channel or cross-track measurement provides a complex SAR image of the scene stored in a matrix of data whose columns correspond to a position along the track and rows correspond to the range dimension. The complex SAR image obtained from an extended area target contains contributions from multiple scattering cells at the intersection of a surface and the gray range shell (indicated with red circles in Figure 2-3).

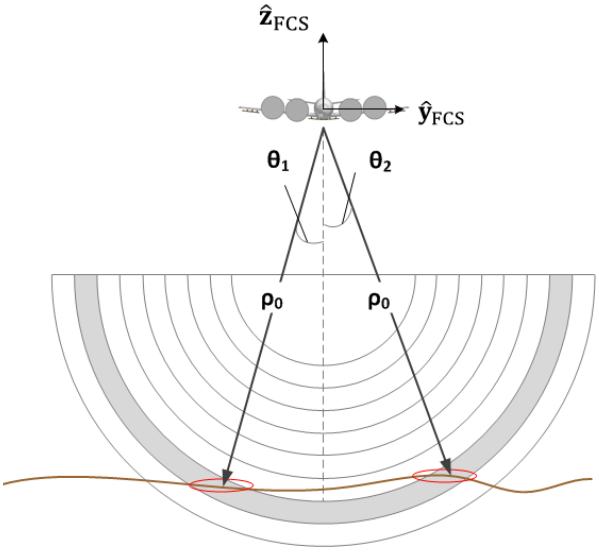

Figure 2-3 Scattering patches in SAR image

Close to nadir where the ground range resolution is coarser, the area of scattering patches is larger (as compared to a sidelooking case). When the scattering interface is rough, a single pixel in the SAR image may contain echoes from multiple layovered scattering cells that are closely spaced in the angular dimension. At the edges of the illuminated swath, corresponding to the larger incidence angles, the ground range resolution becomes finer and the echoing areas become small allowing these scattering patches to be modeled as point targets.

These two cases are compared in the figure below. On the left, the range shell at range ρ_1 intersects a rough surface causing multiple facets to reflect. The areas of the reflecting facets are highlighted in red and the pixel corresponding to this range contains the superposition of the scattering from each of these area targets. Near nadir, it is more likely that the number of scattering areas is on the order of, or larger than, the number of cross-track measurements. At a larger range, ρ_2, the scattering patches are reasonably modeled as two well-separated left/right point targets as shown in the off to side case on the right. In the side looking scattering geometry, it is more likely that the number of targets is much less than the number of measurements, making the side looking imager better suited for tomographic imaging methods.

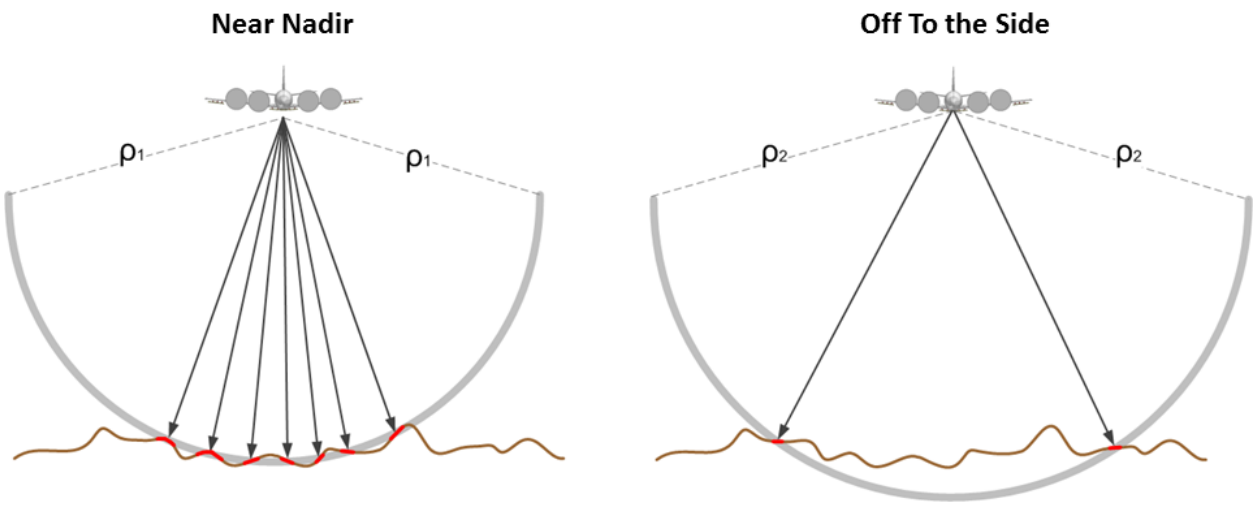

Figure 2-4 Comparison of scattering near nadir and off to the side

In the ice-bed imaging problem, illustrated in Figure 2-5, we assume that clutter from the air-ice interface echoes back at the same time as basal scattering from the ice bottom. We then assume that anywhere from two to four scattering patches dominate the returns arriving after the nadir echo. Two scattering patches are assumed for the sidelooking beams on the same side of nadir to which the beam is steered in transmit: one from air-ice interface and one from the ice-bed interface (i.e. if the beam was steered left in transmit, surface clutter from the left and basal echoes from left are anticipated). The assumption here is that the array provides sufficient left/right isolation that basal echoes from the opposite side may be ignored for echoes arriving from the look direction within the half-power beamwidth of the antenna array. For the sounder beam, four scattering patches are assumed: one from the air-ice interface to left of nadir, one from air-ice interface to right of nadir, one from the ice-bed interface to the left of nadir and one from the ice-bed interface to the right of nadir. This means that our DOA estimation must be capable of resolving up to four distinct directions of arrival.

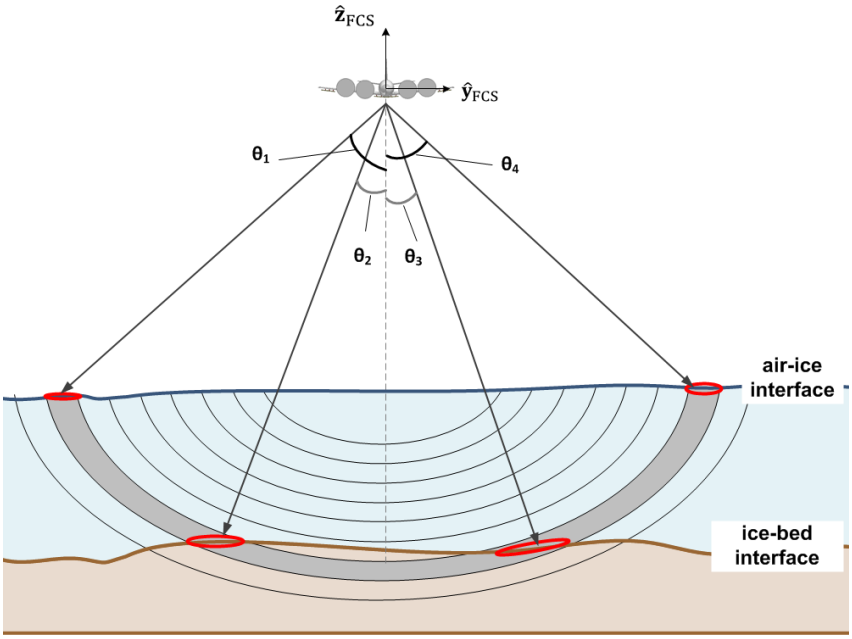

Figure 2-5 Scattering patches in ice-bed imaging problem

2.2.3 Field of View

The wideband direction of arrival estimator that was developed and implemented for this thesis performs a multidimensional search to obtain an estimate of source locations. The algorithm's performance may be improved by restricting the search if we can establish a set of conditions to constrain the solution. One way of doing this is to limit the search based on the range of possible DOAs of the surface and basal backscatter. For this reason, the field of view is considered.

The field of view is taken to be the range of angles that includes all possible source DOAs. Assuming that basal scattering from outside of the half-power beamwidth, ϕ, is negligible, then in multibeam imaging mode the arrival angles of the bed echoes at the array are concentrated over the angular extent $-(\phi_L + \phi_{HP}/2) \leq \theta_{bed} \leq \phi_L + \phi_{HP}/2$. Here ϕ_L is the maximum look angle, taken to be positive. For the 2013 Antarctic mission, the maximum steering angle was 20°. Assuming a 20° half-power beamwidth, then we expect basal scattering to be concentrated between ±30°. The variation of surface clutter angles with platform altitude above ground level are shown in Figure 2-6 for ice with thicknesses of 600 m, 700 m, 1.5 km and 2 km.

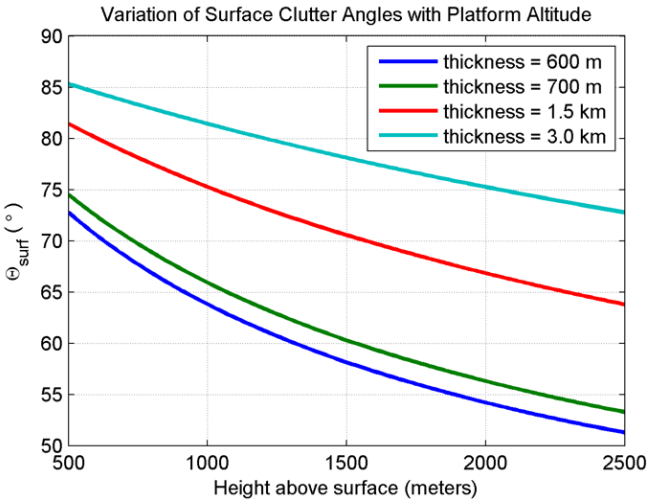

Figure 2-6 Surface clutter arrival angles as a function of platform height

For the 2013 Antarctic high altitude missions, typical values of ice thicknesses over the West Antarctic Ice Sheet were in the range of 600 to 700 meters. In multibeam imaging mode, the radar was operated at high altitude, typically between 1.5 and 2 km above the surface. A range of surface clutter angles that captures these geometries is $48° \leq |\theta_{surf}| \leq 62°$.

2.3 Array Model

This section summarizes the array theory needed to formulate the direction of arrival problem. Both narrowband and wideband array models are presented. Consider an array of M sensors and assume that N_s sources impinge on the array from arrival angles $\theta_1, \ldots, \theta_{N_s}$. The M sensors spatially sample the field arising from the N_s sources at locations $\mathbf{r}_0, \mathbf{r}_1, \ldots, \mathbf{r}_{M-1}$. Let $\tilde{x}_m(t)$ denote the measurement made at passband by the m^{th} sensor whose position is given by the vector $\mathbf{r}_m$. The incident signal due to the i^{th} source is denoted as $\tilde{s}_i(t)$ as measured with respect to an arbitrary reference on the array. The signal received by the m^{th} sensor is the time shifted version of $\tilde{s}_i(t)$ given by $\tilde{s}_i(t - \tau_m(\theta_i))$. Here $\tau_m(\theta_i)$ is the propagation delay between the reference and the m^{th} element due to the n^{th} source given by

$$\tau_m(\theta_i) = -\frac{\mathbf{r}_m^T \mathbf{u}}{c},$$

Where c is the speed of light, $\mathbf{u} = [\sin(\theta_i), \cos(\theta_i)]^T$ is the two element directional cosine vector whose direction cosines with respect to each axis are defined as $u_y = \sin(\theta)$ and $u_z = \cos(\theta)$, and the negative sign arises from the direction of the wave. The wavenumber, $\mathbf{k}$, in terms of $\mathbf{u}$ is $\mathbf{k} = -\frac{2\pi}{\lambda}\mathbf{u}$. The band pass

signal measured by the m^{th} sensor is the following superposition of N signals from source directions $\theta_1, \dots, \theta_{N_s}$

$$\tilde{x}_m(t) = \sum_{i=1}^{N_s} \tilde{s}_i\big(t - \tau_m(\theta_i)\big) + w_m(t), \qquad \text{for } m = 1, \dots, M,$$

Where $w_m(t)$ is white Gaussian noise.

The complex envelope obtained from the m^{th} sensor is then

$$x_m(t) = \sum_{i=1}^{N_s} s_i\big(t - \tau_m(\theta_i)\big)\, e^{-j2\pi f_c \tau_m(\theta_i)} + n_m(t), \qquad \text{for } m = 1, \dots, M. \tag{2-1}$$

Where $n_m(t)$ is a complex Gaussian random variable.

2.3.1 The Narrowband Model

The narrowband DOA estimation methods rely on the fact that a delay in time corresponds to a constant phase shift over a signal's bandwidth in the frequency domain. Let $S_i(f)$ denote the Fourier representation of the signal $s_i(t)$. Suppose this signal is delayed by an arbitrary amount τ. From the time shifting property, $s_i(t - \tau)$ and its Fourier representation are

$$s_i(t - \tau) \overset{\mathcal{F}}{\leftrightarrow} S_i(f) e^{-j2\pi f \tau}. \tag{2-2}$$

In the narrowband model, the bandwidth of the complex envelope is sufficiently small such that the right hand side of (2-1) may be approximated as

$$S_i(f) e^{-j2\pi f \tau} \approx S_i(f) e^{-j2\pi f_c \tau}.$$

Then under the narrowband model, $s_i(t - \tau)$ is modeled as

$$s_i(t - \tau) = \mathcal{F}^{-1}\{S_i(f) e^{-j2\pi f_c \tau}\} = s_i(t) e^{-j2\pi f_c \tau}. \tag{2-3}$$

Substituting equation (2-2) into **Error! Reference source not found.**, the complex envelope obtained from an arbitrary spatial sample is

$$x_m(t) = \sum_{i=1}^{N_s} s_i(t)\, e^{-j2\pi f_c \tau_m(\theta_i)} + n_m(t), \qquad \text{for } m = 1, \dots, M. \tag{2-4}$$

The vector $\mathbf{x}(t)$ is the $M \times 1$ vector containing the array outputs at time t. In the narrowband model, the steering vector

$$\mathbf{a}(\theta_i) = \left[e^{-j2\pi f_c \tau_1(\theta_i)}, \ldots, e^{-j2\pi f_c \tau_M(\theta_i)}\right]^T \quad \textbf{(2-5)}$$

Is used to model propagation of a received signal over the array. The vector $\mathbf{x}(t)$ an be thought of as a snapshot of the array at time, t, and may be written as the following linear combination of steering vectors

$$\mathbf{x}(t) = \mathbf{A}(\boldsymbol{\Theta})\mathbf{s} + \mathbf{n}, \quad \textbf{(2-6)}$$

where

$$\mathbf{A}(\boldsymbol{\Theta}) = \left[\mathbf{a}(\theta_1), \ldots, \mathbf{a}(\theta_{N_s})\right] = \begin{bmatrix} e^{-j2\pi f_c \tau_1(\theta_1)} & \cdots & e^{-j2\pi f_c \tau_1(\theta_{N_s})} \\ \vdots & \ddots & \vdots \\ e^{-j2\pi f_c \tau_M(\theta_1)} & \cdots & e^{-j2\pi f_c \tau_M(\theta_{N_s})} \end{bmatrix},$$

$$\mathbf{s} = \begin{bmatrix} s_1(t) \\ \vdots \\ s_{N_s}(t) \end{bmatrix}, \text{ and } \mathbf{n} = \begin{bmatrix} n_1(t) \\ \vdots \\ n_M(t) \end{bmatrix}.$$

The matrix $\mathbf{A}(\boldsymbol{\Theta})$ is the $M \times N_s$ matrix of steering vectors sometimes referred to as the array manifold, $\mathbf{s}$ is the $N_s \times 1$ vector of whose entries correspond to the values of the N_s signals at time t, and $\mathbf{n}$ is the $M \times 1$ vector of complex white Gaussian noise (CWGN). The noise on the array is taken to be independent and identically distributed with noise power σ_n^2 and $\mathbf{n}$ is then taken to be wide-sense stationary (WSS), multichannel Gaussian random process. In the narrowband model summarized by equations (2-5) and (2-6), the data vector $\mathbf{x}(t)$ may be written as a linear combination of the steering vectors because it is assumed that a steering vector $\mathbf{a}(\theta_i) = \left[e^{-j2\pi f_c \tau_1(\theta_i)}, \ldots, e^{-j2\pi f_c \tau_M(\theta_i)}\right]^T$ evaluated at the carrier frequency is sufficient for modeling the progressive phase shifts across the array over the entire bandwidth.

If we assume the sources and noise to be zero mean and mutually uncorrelated then the covariance matrix is given by the expectation of the outer product of the array outputs

$$\mathbf{R_{xx}} = E[\mathbf{x}(t)\,\mathbf{x}^H(t)] = \mathbf{A}(\boldsymbol{\Theta})\mathbf{R_{ss}}\mathbf{A}^H(\boldsymbol{\Theta}) + \mathbf{R_{nn}} \quad \textbf{(2-7)}$$

$\mathbf{R_{ss}} = E[\mathbf{s}\,\mathbf{s}^H]$ is the source covariance matrix, and $\mathbf{R_{nn}} = E[\mathbf{n}\,\mathbf{n}^H]$ is the noise covariance matrix. Let α_i be the average power associated with source i. When the sources are uncorrelated, then the source covariance matrix is an $N \times N$ diagonal matrix and we define with the average powers to be $\left[\gamma_1, \gamma_2, \ldots, \gamma_{N_s}\right]$ the diagonal. The $M \times M$ noise covariance matrix is given by $\sigma_n^2\,\mathbf{I}$.

The source covariance matrix $\mathbf{R_{ss}}$ is considered a composite covariance matrix that can be decomposed into a sum of the N_s constituent covariance matrices of each source, the i^{th} of which is written as $\mathbf{R_i} = \alpha_i\,\mathbf{a}(\theta_i)\mathbf{a}^H(\theta_i)$. In the narrowband model, the (k,l) element of $\mathbf{R_i}$ is

$$r_{k,l} = E[x_k x_l^*] = \gamma_i\, e^{j2\pi f_c \tau_{k,l}(\theta_i)}, \quad \textbf{(2-8)}$$

where $\tau_{k,l}(\theta_i) = \tau_l(\theta_i) - \tau_k(\theta_i)$. Equation (2-8) suggests that the signal contribution to the correlation between any two elements or cross-track measurements is only a function of target parameters, the source power and source arrival angle.

2.3.2 The Wideband Model

When a received signal is wideband, the steering vectors can no longer be modeled using only f_c. In this case, it is common to use

$$\mathbf{a}(f, \theta_i) = \left[e^{-j2\pi f\tau_1(\theta_i)}, \dots, e^{-j2\pi f\tau_M(\theta_i)}\right]^T \quad \textbf{(2-9)}$$

to emphasize the frequency dependence of a steering vector for an arbitrary arrival angle. The array outputs are then modeled as

$$\mathbf{x}(t) = \int_{f_L}^{f_U} \mathbf{X}(f) e^{-j2\pi(f-f_c)t}\, dt \quad \textbf{(2-10)}$$

there f_L and f_U are the lower and upper frequencies of the bandlimited signal respectively and

$$\mathbf{X}(f) = \mathbf{A}(f, \boldsymbol{\Theta})\mathbf{S}(f) + \mathbf{N}(f).$$

The frequency dependence leads to a frequency dependent model of the covariance matrix

$$\mathbf{R_{xx}}(f) = \mathbf{A}(f, \boldsymbol{\Theta})\mathbf{R_{ss}}(f)\mathbf{A}^H(f, \boldsymbol{\Theta}) + \sigma_n^2(f)\mathbf{I}.$$

The composite covariance matrix for the array output must then be obtained by integrating over the bandwidth

$$\mathbf{R_{xx}} = \int_{f_L}^{f_U} \mathbf{A}(f, \boldsymbol{\Theta})\mathbf{R_{ss}}(f)\mathbf{A}^H(f, \boldsymbol{\Theta}) + \sigma_n^2(f)\mathbf{I}\, df.$$

2.4 Direction of Arrival Estimation in Ice Sheet Tomography

Direction of arrival estimators can be broadly classified as either spectral-based or parametric. The spectral based techniques involve estimation of a spatial power spectrum as a function of the DOA to obtain a function whose peaks correspond to the source locations. The parametric based techniques perform a simultaneous search for the source locations based on some optimization criteria. Both MUltiple SIgnal Classification (MUSIC) and Maximum Likelihood Estimation (MLE) have been used to demonstrate tomographic imaging of the beds of polar ice sheets [10], [11]. An overview of the MUSIC and MLE estimators is presented below as a summary of the documented narrowband methods that have been used

to obtain the DOA in ice bed tomography. MUSIC and MLE assume the narrowband model in equations (2-5) and (2-6). While the two methods vary in formulation, they share a set of common assumptions listed below:

A1: The number of cross-track elements, M, is greater than the number of impinging sources, N_s,

A2: The steering vectors modeling the array response to the source directions are a linearly independent set, which ensures that a unique mapping exists between arrival angle and the associated steering vector (a consequence of the narrowband assumption),

A3: The noise **n** is a complex Gaussian random process that is stationary in the wide sense (WSS) and characterized as having zero mean, and covariance matrix $\sigma_n^2 I$, where I is the M×M identity.

2.4.1 The MUltiple SIgnal Classification (MUSIC) Algorithm

The MUSIC algorithm, first introduced by Schmidt [12], is a subspace method that falls within the spectral based class of DOA estimators. In addition to A1-A3, the MUSIC algorithm requires that

A4$_{music}$: The covariance matrix is non-singular.

The MUSIC algorithm exploits the fact that the M×M covariance matrix in (2-7) admits the following eigen decomposition

$$\mathbf{R_{xx}} = \mathbf{A}(\boldsymbol{\Theta})\mathbf{R_{ss}}\mathbf{A}^{\mathrm{H}}(\boldsymbol{\Theta}) + \mathbf{R_{nn}} = \mathbf{Q_s}\boldsymbol{\Lambda_s}\mathbf{Q_s}^{\mathrm{H}} + \mathbf{Q_n}\boldsymbol{\Lambda_n}\mathbf{Q_n}^{\mathrm{H}}, \tag{2-11}$$

where

$\mathbf{Q_s} \in \mathbb{C}^{M\times N_s}$ is the matrix whose columns are the eigenvectors that form an orthonormal basis for the signal subspace (i.e. $\mathrm{span}\{\mathbf{Q_s}\} = \mathrm{span}\{\mathbf{A}(\boldsymbol{\Theta})\}$),

$\boldsymbol{\Lambda_s} \in \mathbb{C}^{N_s\times N_s}$ is the diagonal matrix of corresponding eigenvalues, and

$\mathbf{Q_n} \in \mathbb{C}^{M\times(M-N_s)}$ is the matrix whose columns are the eigenvectors that form an orthonormal basis for the noise subspace,

$\boldsymbol{\Lambda_n} \in \mathbb{C}^{(M-N_s)\times(M-N_s)}$ is the diagonal matrix of corresponding eigenvalues associated with the noise subspace.

Let $\mathbf{a}(\theta)$ denote the steering vector used to scan over the field of view. Then under the assumption that the signal and noise subspaces are orthogonal,

$$\mathbf{Q}_\mathbf{n}^\mathrm{H}\mathbf{a}(\theta_\mathrm{i}) = 0 \;\forall\; \theta_\mathrm{i}, \qquad \mathrm{i} = 1, \dots, \mathrm{N_s}. \tag{2-12}$$

The estimated MUSIC pseudo spectrum which produces peaks at the corresponding source locations is then given by

$$\mathrm{P_{music}}(\theta) = \frac{\mathbf{a}^\mathrm{H}(\theta)\mathbf{a}(\theta)}{\mathbf{a}^\mathrm{H}(\theta)\widehat{\mathbf{Q}}_\mathrm{n}\widehat{\mathbf{Q}}_\mathrm{n}^\mathrm{H}\mathbf{a}(\theta)}. \tag{2-13}$$

Equation (2-11) is not a power spectrum since it is dimensionless and it cannot be inverted to estimate the power from a particular direction. The MUSIC pseudo spectrum simply provides a measurement of the orthogonality of the manifold and the noise subspace.

When MUSIC is used as the array processing method for tomography, (2-13) is evaluated over a grid of arrival angles obtained from a vector of uniformly spaced $\mathrm{k_y}$ values for every pixel or (u, ρ) pair in the scene. An example of a MUSIC direction of arrival spectrum is shown in Figure 2-7 for an ideal 8 element linear array with half wavelength inter element spacing that spatially samples a field of four sources arriving from angles $\boldsymbol{\Theta} = [-60°, -15°,\ 20°,\ 60°]$. An estimate of the arrival angles, $\widehat{\boldsymbol{\Theta}}$, is obtained through a 1D search of equation (2-11) for $\mathrm{N_s}$ peaks.

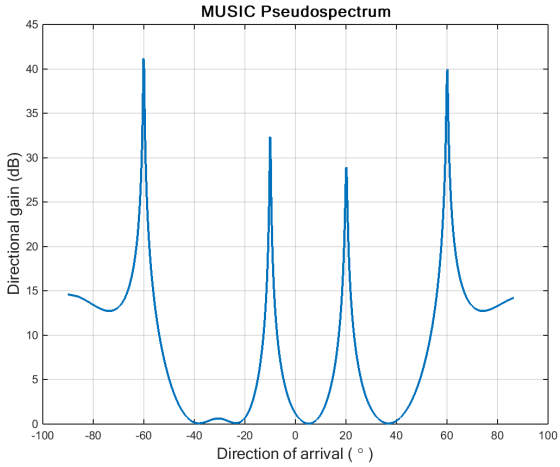

Figure 2-7 Simulated MUSIC pseudospectrum.

2.4.2 The Maximum Likelihood Estimator (MLE)

In addition to assumptions A1-A3, two additional assumptions are made in the formulation of the Maximum Likelihood Estimator of the vector of source directions $\boldsymbol{\Theta} = [\theta_1, \dots, \theta_{\mathrm{N_s}}]^\mathrm{T}$:

A4$_{mle}$: The noise samples from different snapshots are statistically independent, i.e. $E[n_p(t_i)n_m^*(t_k)] = 0$ for $i \neq k$, and

A5$_{mle}$: The sources are regarded as deterministic but unknown [6].

Let $\mathbf{x}(n) = [x_1(n), \dots, x_M(n)]^T$ denote the snapshot of the array at discrete time n. The snapshot model of (2-6) is given by the M×K matrix $\mathbf{X}$ containing K snapshots

$$\mathbf{X} = \mathbf{A}(\boldsymbol{\Theta})\mathbf{S} + \mathbf{N} \tag{2-14}$$

where

$$\mathbf{S} = [\mathbf{s}(n), \mathbf{s}(n+1), \dots, \mathbf{s}(n+K-1)] \text{ and } \mathbf{N} = [\mathbf{n}(n), \mathbf{n}(n+1), \dots, \mathbf{n}(n+K-1)].$$

The multivariate density function of a single snapshot is given by

$$\mathbf{f}(\mathbf{x}) = \frac{1}{\pi^M \det(\mathbf{R_{nn}})} \exp[(\mathbf{x} - \mathbf{A}(\boldsymbol{\Theta})\mathbf{s})^H \mathbf{R_{nn}}^{-1} (\mathbf{x} - \mathbf{A}(\boldsymbol{\Theta})\mathbf{s})].$$

Following from A4$_{mle}$ and A5$_{mle}$, the joint distribution of K successive snapshots is

$$f(\mathbf{X}) = \prod_{i=1}^{K} \frac{1}{\pi^M \det(\mathbf{R_{nn}})} \exp\left[-\frac{1}{\sigma_n^2} |\mathbf{x}(i) - \mathbf{A}(\boldsymbol{\Theta})\mathbf{s}(i)|^2\right]. \tag{2-15}$$

The likelihood function of the three unknown parameters σ_n^2, $\mathbf{S}$, and $\boldsymbol{\Theta}$ conditioned on the observation $\mathbf{X}$ is

$$L(\sigma_n^2, \mathbf{S}, \boldsymbol{\Theta}|\mathbf{X}) = -KM\ln(\pi) - K\ln[\det(\mathbf{R_{nn}})] - \frac{1}{\sigma_n^2} \sum_{i=1}^{K} |\mathbf{x}(i) - \mathbf{A}(\boldsymbol{\Theta})\mathbf{s}(i)|^2. \tag{2-16}$$

In what follows, the first term of (2-15) is omitted without loss of generality. To obtain the maximum likelihood estimate of $\boldsymbol{\Theta}$, the parameters $\boldsymbol{\Theta}$ and $\mathbf{S}$ are held fixed and the likelihood function is maximized with respect to σ_n to obtain

$$\hat{\sigma}_n^2 = \frac{1}{MK} \sum_{i=1}^{K} |\mathbf{x}(i) - \mathbf{A}(\boldsymbol{\Theta})\mathbf{s}(i)|^2. \tag{2-17}$$

Substituting (2-16) into (2-15) and again omitting constant terms, the maximum likelihood estimate of the unknown parameters $\boldsymbol{\Theta}$, and $\mathbf{S}$ are given by the following maximization

$$\max_{\boldsymbol{\Theta}, \boldsymbol{S}} \left\{ -KM \ln \left(\sum_{i=1}^{K} |\mathbf{x}(i) - \mathbf{A}(\boldsymbol{\Theta})\mathbf{s}(i)|^2 \right) \right\}$$

Or equivalently

$$\min_{\boldsymbol{\Theta},\boldsymbol{S}} \left(\sum_{\mathrm{i}=1}^{\mathrm{K}} |\mathbf{x}(\mathrm{i}) - \mathbf{A}(\boldsymbol{\Theta})\mathbf{s}(\mathrm{i})|^2 \right). \tag{2-18}$$

Holding $\boldsymbol{\Theta}$ fixed, then the solution to the minimization in (2-18) is given by the Least Squares solution to (2-14)

$$\hat{\mathbf{s}}(\mathrm{i}) = \left(\mathbf{A}^{\mathrm{H}}(\boldsymbol{\Theta})\mathbf{A}(\boldsymbol{\Theta}) \right)^{-1} \mathbf{A}^{\mathrm{H}}(\boldsymbol{\Theta})\mathbf{x}(\mathrm{i}). \tag{2-19}$$

The following projection matrix notation is introduced

$$\mathbf{P}_{\mathbf{A}(\boldsymbol{\Theta})} = \mathbf{A}(\boldsymbol{\Theta}) \left(\mathbf{A}^{\mathrm{H}}(\boldsymbol{\Theta})\mathbf{A}(\boldsymbol{\Theta}) \right)^{-1} \mathbf{A}^{\mathrm{H}}(\boldsymbol{\Theta}). \tag{2-20}$$

Recall that the matrix $\mathbf{A}(\boldsymbol{\Theta})$ is the model of the array manifold for a given vector of arrival angles.

Following the substitution of (2-18) into (2-17) and expressing the likelihood function in terms of $\mathbf{P}_{\mathbf{A}(\boldsymbol{\Theta})}$ and $\mathbf{R}_{\mathbf{xx}}$ leads to the final form

$$\mathrm{L}(\boldsymbol{\Theta}) = \mathrm{trace}\left(\mathbf{P}_{\mathbf{A}(\boldsymbol{\Theta})} \mathbf{R}_{\mathbf{xx}} \right). \tag{2-21}$$

An example of the likelihood function is provided below for a simulation involving an ideal linear array of 8 elements. The surface in Figure 2-8 is an example of the MLE cost function for a 2 dimensional signal subspace estimated from 100 snapshots. Two sources were simulated, each with 20 dB SNR and whose arrival angles are given by the vector $\boldsymbol{\Theta} = [-20°, 20°]$. (2-21) is evaluated over a grid of 128 possible steering vectors showing that the global maximum of the cost function coincides with true arrival angle solution.

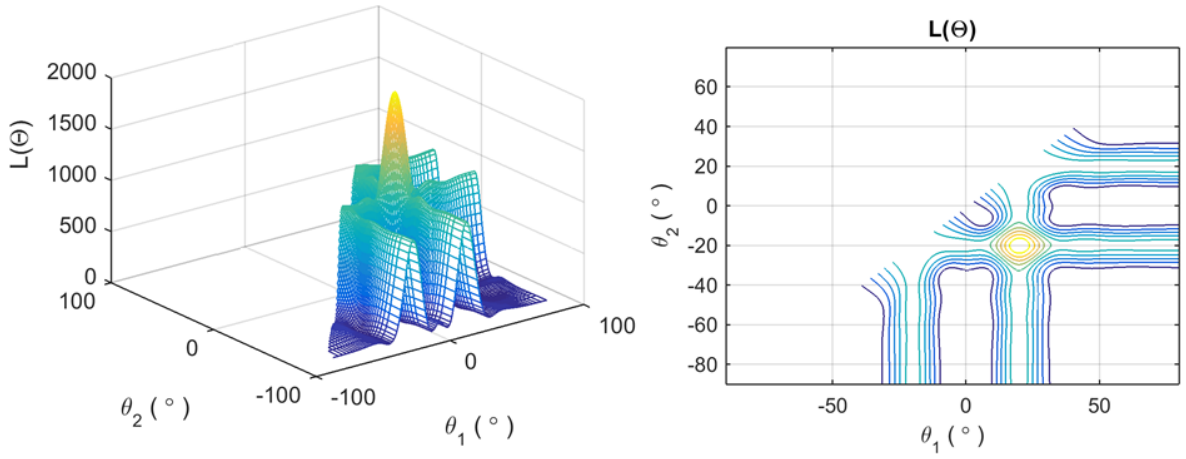

Figure 2-8 Simulated likelihood function represented as a surface (left) and contours (right).

The Maximum Likelihood Estimate of the vector of source directions is then given by the following maximization problem

$$\widehat{\boldsymbol{\Theta}} = \max_{\boldsymbol{\Theta}}\{\mathrm{L}(\boldsymbol{\Theta})\} = \max_{\boldsymbol{\Theta}}\left\{\mathrm{trace}\left(\mathbf{P}_{\mathbf{A}(\boldsymbol{\Theta})}\mathbf{R}_{\mathbf{xx}}\right)\right\}. \quad \textbf{(2-22)}$$

Equation (2-22) is a multidimensional nonlinear maximization of the real-valued cost function $\mathrm{L}(\boldsymbol{\Theta})$ and does not admit an analytical solution. Instead, it must be solved numerically with the use of a gradient based search algorithm like the steepest descent or Gauss-Newton method. When the dimensionality of the signal subspace is small[3], $\widehat{\boldsymbol{\Theta}}$ can be computed by evaluating (2-21) over a coarse grid to obtain an initial estimate of the peak and then refining this estimate with a gradient search technique. Higher dimensionality problems require more efficient methods like the Alternating Projection (MLE-AP) approach to maximizing $\mathrm{L}(\boldsymbol{\Theta})$ that is presented by Ziskind and Wax in [6]. MLE-AP is an iterative search algorithm that decomposes the multidimensional maximization into $\mathrm{N_s}$ single dimensional searches to refine some initial estimate of the peak. In the context of ice bed tomography, MLE requires an exhaustive search of the $\mathrm{N_s}$ dimensional cost function must be carried out for every pixel in the scene.

2.4.3 Differences between MUSIC and MLE

MLE is optimal in the maximum likelihood sense when the noise is a complex Gaussian random process. Thus the underlying assumption is that the distribution of the noise is known. MUSIC assumes orthogonality between the signal and noise subspaces to ensure satisfaction of (2-12). Another way of stating this is that MUSIC requires that the noise eigenvectors be orthogonal to all of the steering vectors meaning that MUSIC is sensitive to array calibration errors. Both algorithms assume the narrowband data model in (2-6) and, as will be shown, their performance degrades to an intolerable degree when this model fails to represent the received signals. Additionally both algorithms assume knowledge of the dimensionality of the signal subspace. MLE has been shown to outperform MUSIC in both low SNR and limited snapshot scenarios [6] making it more appropriate for accurately estimating the DOA from the edges of the swath where the returns are weak. Although MLE is optimal, it is computationally expensive.

2.5 Classification of Imaging Geometries as Wideband

The definition of the wideband problem in literature is often times vague but here an attempt is made to establish criteria for characterizing imaging geometries as narrowband or wideband. The time-bandwidth product

[3] In [24], Van Trees considers the signal subspace dimension to be small when $\mathrm{N_s} \leq 3$.

$$\tau_{max}(\theta)BW \tag{2-23}$$

of the cross-track array seems to be the most appropriate measure for establishing the criterion to classify an imaging geometry as wideband. Here BW refers to the bandwidth of the received chirp, and the time term is the maximum propagation delay across the aperture (taken to be the propagation delay between the outermost elements) within the field of view. The maximum propagation delay in terms of the largest dimension of the cross-track aperture (equivalent to the length of the array in the y-dimension for the Basler configuration) denoted as L_y, is

$$\tau_{max}(\theta) = \frac{L_y}{c}\sin(\theta).$$

The system bandwidth and cross-track aperture length are fixed so establishing whether or not the Basler system is wideband will depend on the arrival angle.

A simple imaging example is used to illustrate differences in narrowband and wideband imaging geometry by relating the physical propagation of an echo from a point target to pixels in the SAR image. Consider 3-channel SAR that images a scene containing only an ideal point target which is perfectly focused to the n^{th} fast time bin and the k^{th} along-track sample of the reference channel, taken to be the center element. The range to the target at zero Doppler is ρ_0 and its corresponding two-way propagation is T_0. The imaging geometry of this example is shown in Figure 2-9 below.

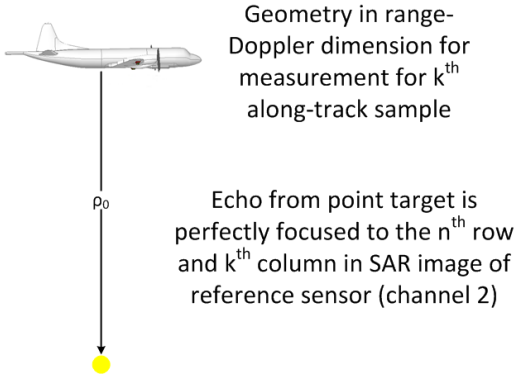

Figure 2-9 Example used to characterize narrowband and wideband imaging geometries

2.5.1 Narrowband Imaging System

In [13] Van Trees states that the narrowband assumption is valid for $\tau_{max}(\theta)BW \ll 1$. When this holds, a signal remains correlated over the array and the cross-correlation of sensors k and l may be modeled as

$$r_{k,l} = \sum_{i=1}^{N_s} \gamma_i e^{j2\pi f_c \tau_{k,l}(\theta_i)}. \quad \textbf{(2-24)}$$

The underlying assumption of (2-24) is that the sources are uncorrelated. In the narrowband model the angular dependence of the complex correlation between sensors is characterized by the phase of (2-24).

An example of a narrowband imaging geometry is shown below to illustrate how the physical model relates to the pixel values in the SAR images and to distinguish between narrowband and wideband imaging geometries. On the top half of Figure 2-10 the SAR focused echo, s(T), from a point target is shown in yellow as it washes over an ideal array of three elements (indicated with crosses). The target's two-way propagation delay as measured with respect to the center channel is given by T_0.

The example shows a snapshot of the array when the range impulse response is centered on channel 2. The resolution elements ΔT, measured in seconds, and $\Delta\rho$, measured in meters, refer to temporal (measured as a two-way travel time) and range resolution elements and are defined by the 3 dB roll off of the range impulse response. On the bottom half of the figure, the SAR images of each channel are illustrated. The middle element is defined as the reference of the imaging geometry in the y-z plane. The target appears in the n^{th} fast time bin of the complex SAR image obtained from the reference channel with an intensity value that maps to a yellow pixel.

In the narrowband imaging geometry, the maximum propagation delay between the outermost elements is less than the temporal resolution element, ΔT, for all possible arrival angles within the field of view. Because this is satisfied, then the following statement is taken to be valid

$$s(T_0 + \tau_1) = s(T_0) = s(T_0 + \tau_3) \quad \textbf{(2-25)}$$

And the corresponding pixel values indicated in yellow have the same magnitude across all of the channels. The target is registered in range meaning that it appears in the same fast time bin in each image. The correlation between any two channels may then be modeled in this case using Equation (2-24) as $r_{k,l} = \gamma \cdot e^{j2\pi f_c \tau_{k,l}(\theta)}$. In the narrowband model, the magnitude of the complex covariance between any two arbitrary channels is equal to the target SNR, γ (or sum of SNRs for multiple targets).

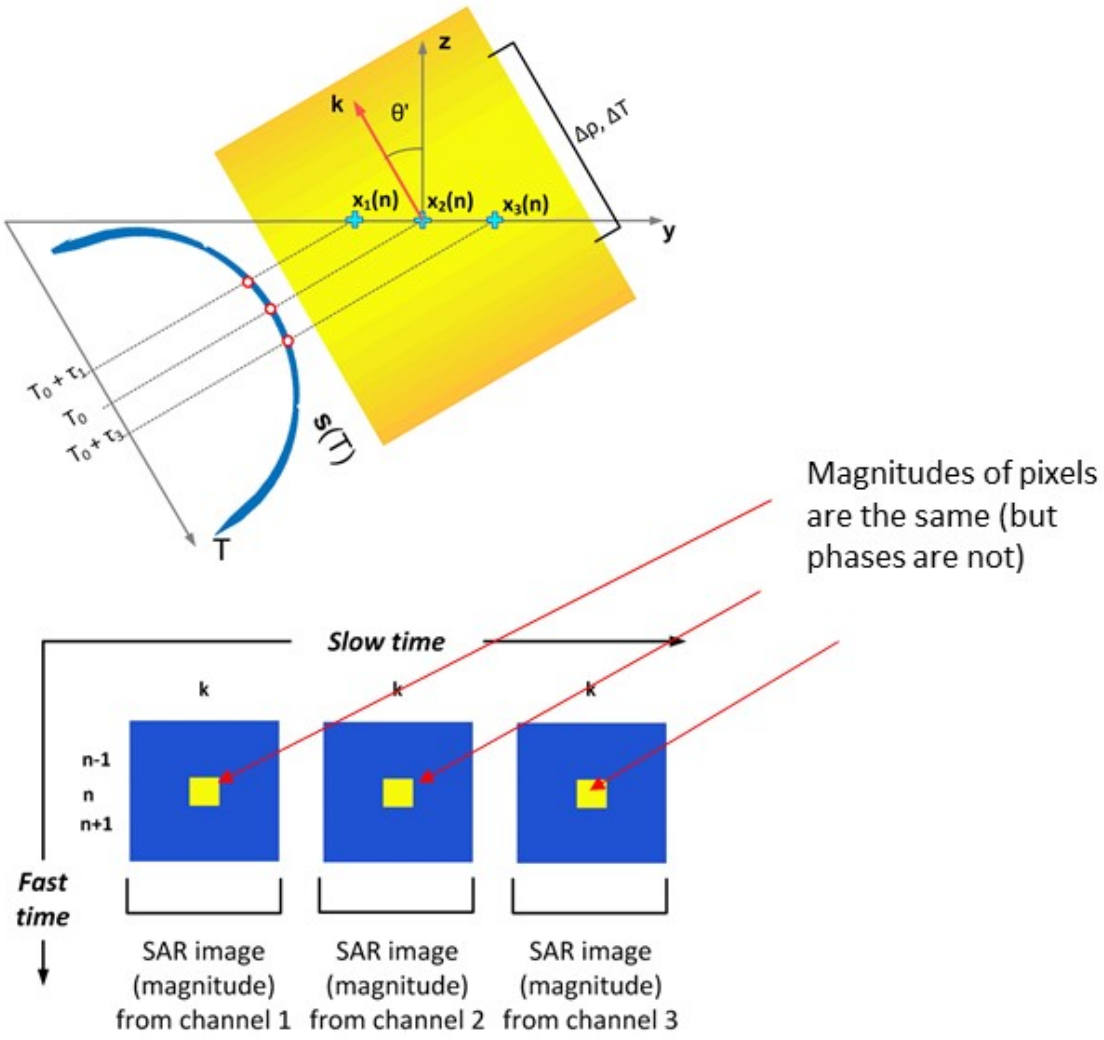

Figure 2-10 Narrowband imaging geometry and SAR images

2.5.2 Wideband Imaging System

In the description of wideband imaging systems, two cases are considered: 1) those where targets are registered in range across the receivers and 2) those that exhibit registration errors. Registration errors occur when the time-bandwidth product exceeds 1. Thus the first scenario corresponds to geometries that may be modeled as $\tau_{\max}(\theta)\mathrm{BW} < 1$ but that are not well described by the narrowband model while the second describes the situation where $\tau_{\max}(\theta)\mathrm{BW} > 1$.

Scenario 1: Wideband Geometry with Registered Target

The example in Figure 2-9 is still assumed only now we consider a wideband system, meaning that the range resolution elements will be finer than those associated with the narrowband system. An illustration of a snapshot of the array as the echo from the target is maximally aligned with channel 2 is shown Figure

2-11. Here the time-bandwidth product is still less than 1 but inter element propagation delays are approaching the order of the temporal resolution of the SAR. The imaging geometry shown violates the narrowband assumption because Equation (2-25) is no longer valid. Though the target is registered in range across the three SAR images, a roll-off over the channels is observable in the magnitudes of the target pixels. In this case, the complex covariance between the sensors k and l is more adequately modeled by a DOA dependent magnitude term that models the roll-off as

$$r_{k,l} = \gamma \cdot g\left(\tau_{k,l}(\theta)\right) \cdot e^{j2\pi f_c \tau_{k,l}(\theta)}. \quad \textbf{(2-26)}$$

If the power spectrum of echo from the target is known to be flat, then $g\left(\tau_{k,l}(\theta)\right)$ may be modeled as $g\left(\tau_{k,l}(\theta)\right) = \mathrm{sinc}\left(\pi BW \tau_{k,l}(\theta)\right)$.

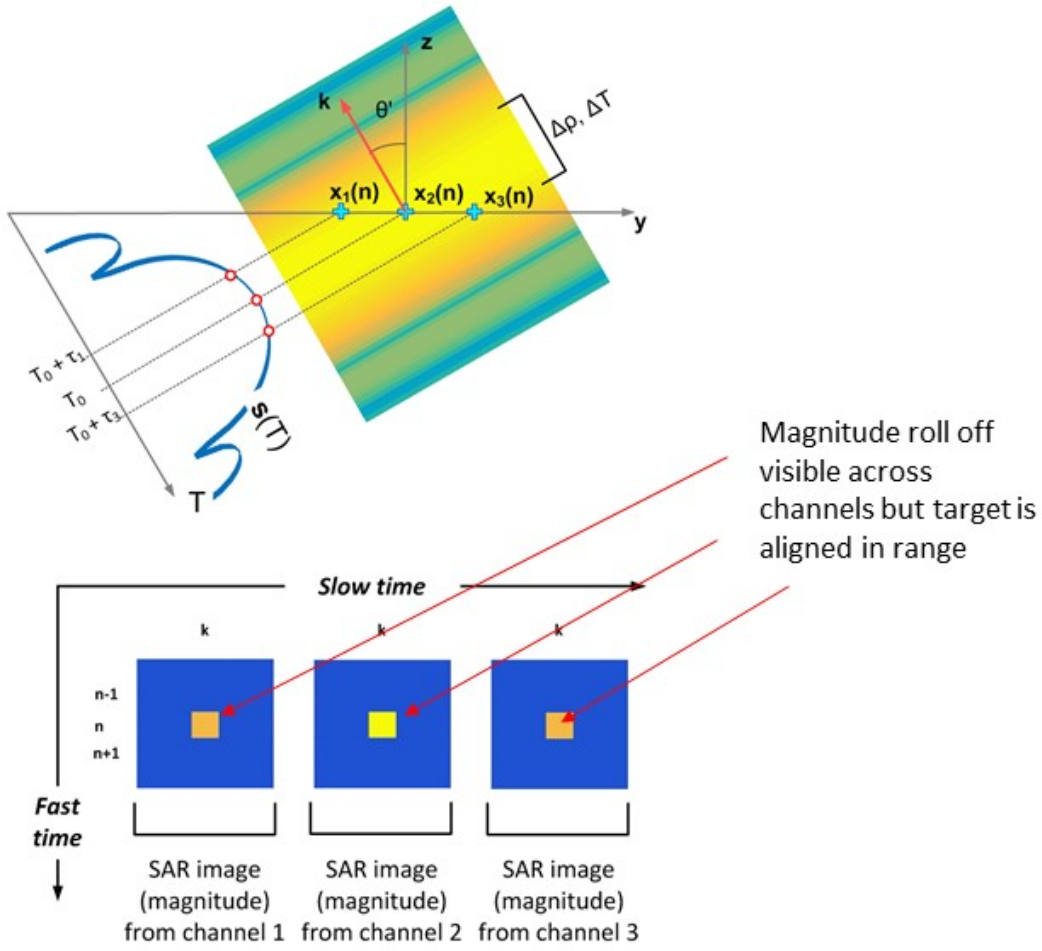

Figure 2-11 Wideband imaging geometry and SAR images with registered target

Scenario 2: Wideband Geometry with Registration Error

When $\tau_{max}(\theta)BW = 1$ there is complete decorrelation in fast-time between signals arriving at opposite ends of the array, the corresponding geometry may clearly be described as wideband. For the Basler system, where the length of the cross-track aperture is 3.36 meters and the bandwidth is 250 MHz, this angle is computed as

$$\theta = \sin^{-1}\left(\frac{c}{L_y BW}\right) = 20°.$$

Recall that in multibeam mode, the look angles for the 2013 Antarctic mission were $\pm 20°$. We can then expect registration errors well within the footprint to be observed in the UWB data set. An example of an imaging geometry with time-bandwidth product exceeding 1 is shown in Figure 2-12 below. In this case, we see the point target migrate in range across the channels and may or may not show the roll off of the point target response depending on the geometry. In this case, to fully characterize the complex covariance between sensors, we need to capture the correlation at different lags, i.e.

$$r_{k,l}(m) = E\{x_k(i)x^*(j)\}, m = i - j.$$

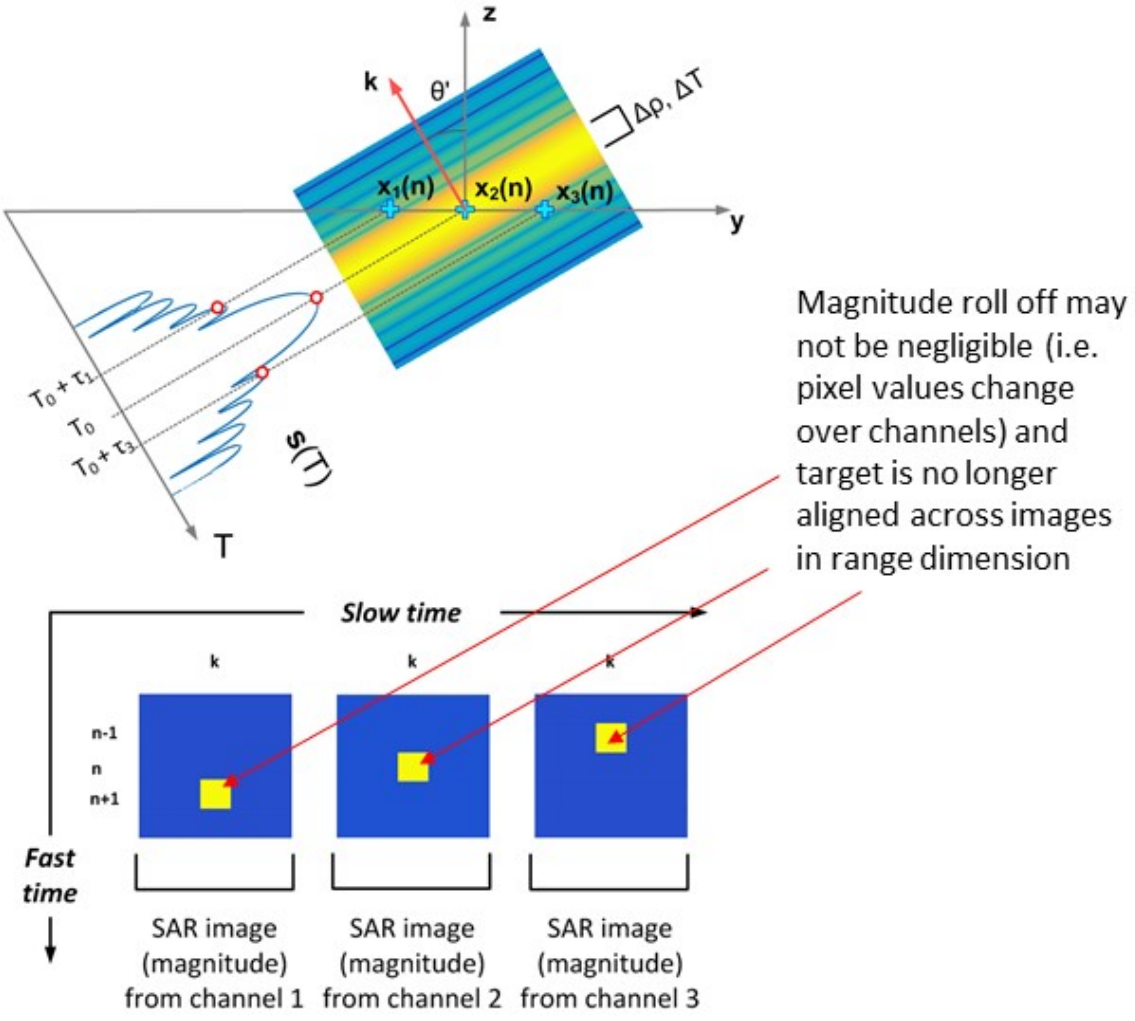

Figure 2-12 Wideband imaging geometry and SAR images with registration error

2.6 Previous Work on Wideband Direction of Arrival

2.6.1 Incoherent and Coherent Methods

Two broad categories of wideband DOA estimators exist in the literature, both of which pose certain limitations for the ice sheet tomography problem. These categories classify wideband DOA estimators as either coherent or incoherent. The incoherent methods use subbanding to estimate the DOA at each frequency bin with narrowband methods and average the results over the total bandwidth [14]. This in effect degrades the range resolution in order to obtain an estimate of the DOA. The approach is not optimal for two reasons. First, by degrading the range resolution, we allow more targets to be illuminated and the dimensionality of the signal subspace must increase to resolve them meaning this modified imaging problem transcends our existing left/right separation framework. Second, the incoherent methods perform poorly in low SNR and low snapshot scenarios.

While the incoherent methods treat each frequency bin independently, the coherent methods attempt to align the signal subspaces over the bandwidth but require initial DOA estimates to do so. The coherent techniques make use of a preprocessing step where the covariance matrices estimated in each subband are focused to the center frequency using a transformation matrix called a focusing matrix. This requires some initial estimate of the DOA. The Coherent Signal Subspace Method (CSSM) introduce by Wang [15], [16]. In addition to this requirement which may not be attainable in practice, they also perform poorly in low SNR scenarios making them undesirable for imaging at the edges of the swath.

2.6.2 Parametric Modeling of the Spatial Covariance Matrix

In a review of the literature, a paper was identified that described a method that obtained an estimate of the direction of arrival of a wideband signal by fitting their data to a model of the spatial covariance matrix [17]. The phase components of their complex covariance matrix model are based on the interelement phase shifts used in the familiar narrowband steering vectors but they introduce a sinc term to model the decorrelation between elements. Under the assumption that the sources are uncorrelated, the composite covariance matrix due to N_s sources can be modeled into a summation of signal covariance matrices and a noise covariance matrix

$$\mathbf{R_{xx}} = \sum_{\mathbf{n=1}}^{\mathbf{N_s}} \mathbf{R_{ss}}(\theta_n) + \sigma_n^2 \mathbf{I}. \tag{2-27}$$

Assuming the received signal to have a flat power spectrum, the authors model the contribution of the n^{th} source to the (k, l) entry of $\mathbf{R_{xx}}$ as

$$[\mathbf{R_{ss}}(\theta_n)]_{k,l} = r_{k,l}(\theta_n) = \gamma_n \text{sinc}\left(BW\tau_{k,l}(\theta_n)\right) e^{j2\pi f_c \tau_{k,l}(\theta_n)} \quad \textbf{(2-28)}$$

Where

γ_n is the average power of the source at θ_n,

BW is the bandwidth of the received signal,

f_c is the carrier frequency of the passband signal, and

$\tau_{k,l}(\theta_n)$ is the interelement propagation delay due to the n^{th} source given by $\tau_{k,l}(\theta_n) = \tau_l(\theta_n) - \tau_k(\theta_n)$. Based on an assumption that the sources are uncorrelated, the (k, l) value of the composite covariance matrix is of the form

$$[\mathbf{R_{ss}}]_{k,l} = \sum_{n=1}^{N_s} r_{k,l}(\theta_n).$$

The $(M-1)\times 1$ vector $\mathbf{r_i}$ is introduced to describe the i^{th} column of $\mathbf{R_{ss}}$ with the (i, i) entry removed[4]. Then from (2-28) it follows that $\mathbf{r_i}$ is of the form

$$\mathbf{r_i} = \widetilde{\mathbf{A}}\boldsymbol{\gamma},$$

Here $\widetilde{\mathbf{A}}_i = \left[\tilde{\mathbf{a}}(\theta_1), \ldots, \tilde{\mathbf{a}}\left(\theta_{N_s}\right)\right]$ is the matrix of truncated steering vectors, with $\tilde{\mathbf{a}}(\theta)$ being the $M-1\times 1$ steering vector of (2-5) scaled by the sinc decorrelation as in (2-28) with the i^{th} entry removed and gamma is the vector of average powers associated with the sources $\boldsymbol{\gamma} = \left[\gamma_1, \ldots, \gamma_{N_s}\right]^T$.

As an example, suppose we had an array of 3 elements and a priori knowledge of two sources. We would model $\mathbf{r_1}$ as

$$\mathbf{r_1} = \begin{bmatrix} \text{sinc}\left(BW\tau_{2,1}(\theta_1)\right) e^{j2\pi f_c \tau_{2,1}(\theta_1)} & \text{sinc}\left(BW\tau_{2,1}(\theta_2)\right) e^{j2\pi f_c \tau_{2,1}(\theta_2)} \\ \text{sinc}\left(BW\tau_{3,1}(\theta_1)\right) e^{j2\pi f_c \tau_{3,1}(\theta_1)} & \text{sinc}\left(BW\tau_{3,1}(\theta_2)\right) e^{j2\pi f_c \tau_{3,1}(\theta_2)} \end{bmatrix} \begin{bmatrix} \gamma_1 \\ \gamma_2 \end{bmatrix}.$$

The i^{th} column of the estimated covariance matrix (with i^{th} entry removed) is taken to be a linear combination of the vectors in $\widetilde{\mathbf{A}}_i$, $\mathbf{r_i} \in \text{span}\{\widetilde{\mathbf{A}}_i\}$ and this fact is used to formulate the following cost function

[4] It is unclear why the authors chose to ignore the diagonal terms of $\mathbf{R_{xx}}$ in their formulation of a cost function. In simulating their spatial only parametric technique, including these terms improved the DOA estimates, albeit only slightly.

$$J(\boldsymbol{\Theta}) = \sum_{i=1}^{M} \hat{\mathbf{r}}_i^H \mathbf{P}_{\mathbf{A}_i(\boldsymbol{\Theta})}^{\perp} \hat{\mathbf{r}}_i \,, \tag{2-29}$$

Which when minimized provides an estimate of the vector of source locations $\widehat{\boldsymbol{\Theta}}$. Their technique was applied in simulations of wideband signal environments based on the Basler system parameters but the performance did not offer significant improvement over the narrowband methods and degraded more rapidly than MUSIC and MLE when the DOA increased further off nadir.

2.7 Parametric Modeling of Space-Time Covariance in Wideband Imaging

The parametric modeling of the spatial covariance matrix in [17] does not fully model the correlation between cross-track measurements obtained from the imaging geometry of the UWB depth sounder configured for the Basler aircraft. This is because the imaging geometry on this platform leads to registration errors in the SAR images. Registration errors refer to a misalignment in the images when a target does not show up in the same pixel for every cross-track image but instead appears to migrate in the images. Image registration allows the targets to be realigned but can only be used to align to a single DOA meaning only one target can be resolved for every (u, ρ) pair in the scene. This makes image registration impractical for cases where we wish to resolve multiple scattering directions as is needed to separate bed echoes from the left and right or where basal scattering and surface scattering need to be resolved.

2.8 Chapter Summary

This chapter described the mutlibeam imaging concept for obtain swath images of ice sheet basal morphology over wide swaths in a single pass. The tomographic formulation was described to give context to the 3D imaging problem and to establish the arrival angle as the missing coordinate for resolving targets across the track. Array processing theory was reviewed and difference between the narrowband and wideband models were discussed. The chapter concluded by laying a foundation for the space-time direction of arrival method developed in this thesis.

Chapter 3

Methodology

3.1 Parametric, Space-Time Direction of Arrival Estimation

3.1.1 Proposed Space-Time Formulation

A space-time formulation is proposed to more accurately model signals received by a wideband imaging geometry. To do this, a widening factor, W, is introduced that describes the maximum propagation delay in samples of a received signal across the cross-track aperture, corresponding to the case of a DOA equal to $\pm 90°$, calculated as:

$$W = \lceil \tau_{max} \cdot f_s \rceil,$$

Where $\lceil \ \rceil$ is the ceiling operator, τ_{max} is the maximum propagation delay across the cross-track aperture in seconds, and f_s is the sampling frequency of the SAR processed outputs. During SAR processing, the data are decimated to the bandwidth of the received chirp, BW. The maximum propagation delay in seconds in terms of the length of the aperture across the track, L_y, and the speed of light, c, is calculated as

$$\tau_{max} = \frac{L_y}{c}.$$

The variable W then represents the time-bandwidth product of the cross-track aperture. For the Basler imaging configuration, W = 4, meaning that in the extreme case a signal from $\pm 90°$ at one end of the array will appear on the opposite end 4 samples later. Since the field of view is generally more restricted than this because of transmit beamforming we chose to use W = 3.

3.1.2 The Space-Time Covariance Matrix

Let $x_m(n)$ correspond to a measurement made by the m^{th} sensor at discrete time n. Then the $M\times 1$ vector $\mathbf{x}(n) = [x_1(n), x_2(n), \dots, x_m(n)]^T$ is the vector containing the spatial samples of a field at discrete time n. We use a temporal ordering of spatial samples to construct a space-time covariance matrix. Let $\tilde{\mathbf{x}}$ denote the vector obtained from a temporal ordering of spatial samples. We wish to construct this vector so that the direction of any target within the field of view can be unambiguously identified so it must contain W time samples. For the case of W = 3, the space-time vector $\tilde{\mathbf{x}} \in \mathbb{C}^{M\cdot W\times 1}$ is thus constructed as

$$\tilde{\mathbf{x}} = [\mathbf{x}(n-1) \mid \mathbf{x}(n) \mid \mathbf{x}(n+1)]^T. \tag{3-1}$$

From the space-time vector $\tilde{\mathbf{x}}$, a space-time data covariance matrix (DCM) is constructed as

$$\mathbf{R}_{\tilde{\mathbf{x}}\tilde{\mathbf{x}}} = E\{\tilde{\mathbf{x}}\tilde{\mathbf{x}}^H\}. \tag{3-2}$$

Equation (3-1) is substituted into (3-2) to provide insight into the structure of the space-time DCM below

$$\mathbf{R}_{\tilde{\mathbf{x}}\tilde{\mathbf{x}}} = \begin{bmatrix} E\{\mathbf{x}(n-1)\mathbf{x}^H(n-1)\} & E\{\mathbf{x}(n-1)\mathbf{x}^H(n)\} & E\{\mathbf{x}(n-1)\mathbf{x}^H(n+1)\} \\ E\{\mathbf{x}(n)\mathbf{x}^H(n-1)\} & E\{\mathbf{x}(n)\mathbf{x}^H(n)\} & E\{\mathbf{x}(n)\mathbf{x}^H(n+1)\} \\ E\{\mathbf{x}(n+1)\mathbf{x}^H(n-1)\} & E\{\mathbf{x}(n+1)\mathbf{x}^H(n)\} & E\{\mathbf{x}(n+1)\mathbf{x}^H(n+1)\} \end{bmatrix},$$

which may be expressed as the following block matrix

$$\mathbf{R}_{\tilde{\mathbf{x}}\tilde{\mathbf{x}}} = \begin{bmatrix} \mathbf{R}_{\mathbf{xx}}(1,1) & \mathbf{R}_{\mathbf{xx}}(1,0) & \mathbf{R}_{\mathbf{xx}}(1,-1) \\ \mathbf{R}_{\mathbf{xx}}(0,1) & \mathbf{R}_{\mathbf{xx}}(0,0) & \mathbf{R}_{\mathbf{xx}}(0,-1) \\ \mathbf{R}_{\mathbf{xx}}(-1,1) & \mathbf{R}_{\mathbf{xx}}(-1,0) & \mathbf{R}_{\mathbf{xx}}(-1,-1) \end{bmatrix}, \tag{3-3}$$

where the $\mathbf{R}_{\mathbf{xx}}(i,j)$ is defined as $\mathbf{R}_{\mathbf{xx}}(i,j) = E\{\mathbf{x}(i)\mathbf{x}^H(j)\}$ and corresponds to the covariance of the spatial samples at discrete times i and j. If we assume that the space-time process is stationary over our observation interval, then (3-3) may be expressed in terms of lags as

$$\mathbf{R}_{\tilde{\mathbf{x}}\tilde{\mathbf{x}}} = \begin{bmatrix} \mathbf{R}_{\mathbf{xx}}(0) & \mathbf{R}_{\mathbf{xx}}^H(-1) & \mathbf{R}_{\mathbf{xx}}^H(-2) \\ \mathbf{R}_{\mathbf{xx}}(1) & \mathbf{R}_{\mathbf{xx}}(0) & \mathbf{R}_{\mathbf{xx}}^H(-1) \\ \mathbf{R}_{\mathbf{xx}}(2) & \mathbf{R}_{\mathbf{xx}}(1) & \mathbf{R}_{\mathbf{xx}}^H(0) \end{bmatrix}. \tag{3-4}$$

The forms of $\mathbf{R}_{\tilde{\mathbf{x}}\tilde{\mathbf{x}}}$ summarized in (3-3) and (3-4) offer insight into the structure of the space-time DCM. $\mathbf{R}_{\tilde{\mathbf{x}}\tilde{\mathbf{x}}} \in \mathbb{C}^{M\cdot W\times M\cdot W}$ is a complex-valued square matrix with dimensionality given by the product of the number of sensors, M, and the widening factor, W. Recall that W=3 for the Basler system, so the DCM in this case is a 24 by 24 complex valued square matrix. $\mathbf{R}_{\tilde{\mathbf{x}}\tilde{\mathbf{x}}}$ is composed of W^2 $M\times M$ submatrices that

describe the spatial covariance at different temporal lags. The submatrices along the main diagonal are the spatial-only covariance structures describing how the sensors are correlated in space. The off-diagonal submatrices describe space-time correlation of a field.

In practice, the quantity in (3-3) or (3-4) is estimated by averaging over a neighborhood of pixels, assuming the stationarity of $\tilde{\mathbf{x}}$ over that neighborhood. The variable $\widetilde{\mathrm{K}}$ is introduced to denote the number of space-time snapshots available for averaging. Let $\widetilde{\mathbf{X}} \in \mathbb{C}^{\mathrm{M}\cdot\mathrm{W}\times\widetilde{\mathrm{K}}}$ denote the matrix containing the $\widetilde{\mathrm{K}}$ space-time snapshots. Then an estimate of $\mathbf{R}_{\tilde{\mathbf{x}}\tilde{\mathbf{x}}}$ is obtained as

$$\widehat{\mathbf{R}}_{\tilde{\mathbf{x}}\tilde{\mathbf{x}}} = \frac{1}{\widetilde{\mathrm{K}}}\widetilde{\mathbf{X}}\widetilde{\mathbf{X}}^{\mathrm{H}}.$$

3.1.3 Model of the Space-Time Covariance Matrix

The wideband direction of arrival algorithm (WDOA) uses a model of the space-time DCM described in (3-3) that is parameterized by the variable $\boldsymbol{\Theta}$. Let $\mathbf{R}_{\mathrm{ss}}(\boldsymbol{\Theta})$ denote the signal contribution to the model of the space-time DCM as a function of the vector of source arrival angles, $\boldsymbol{\Theta}$. The (k,l) entry of $\mathbf{R}_{\mathrm{ss}}(\boldsymbol{\Theta})$ is a function of the lag variable m as well as $\boldsymbol{\Theta}$, modeled as

$$\mathrm{r}_{\mathrm{k,l}}(\boldsymbol{\Theta}) = \sum_{\mathrm{i}}^{\mathrm{N_s}} \gamma_{\mathrm{i}} \cdot \mathrm{g}\big(\tau_{\mathrm{k,l}}(\theta_{\mathrm{i}}) - \mathrm{mT_s}\big)\mathrm{e}^{-\mathrm{j}2\pi \mathrm{f_c}\tau_{\mathrm{k,l}}(\theta_{\mathrm{i}})}. \qquad \textbf{(3-5)}$$

With γ_{i} denoting the SNR of the i^{th} source. The lag depends on which submatrix the (k,l) falls into based on (3-4). The function $\mathrm{g}(\mathrm{t})$ is imposed to model the correlation between sensors in space and time. As was described in Chapter 2, suppose we knew that the power spectrum of the received signal to be flat. Then $\mathrm{g}(\mathrm{t})$ could be modeled as a sinc function. The model of $\mathrm{g}(\mathrm{t})$ must be modeled to account for the use frequency domain windowing applied to each individual channel during pulse compression. Let $\mathrm{H}(\mathrm{f})$ denote the frequency domain windowing function. Then g(t) is taken to be

$$\mathrm{g}(\mathrm{t}) = \mathcal{F}^{-1}\{\mathrm{H}(\mathrm{f})\}. \qquad \textbf{(3-6)}$$

$\mathrm{H}(\mathrm{f})$ is chosen to match the windowing applied during SAR processing. This typically corresponded to a Hanning window.

3.1.4 Cost Function Based on Covariance Matrix Fitting

The WDOA algorithm follows the formulation presented in [17] but applies the method to space-time measurements based on the reasoning offered in a discussion of a covariance matrix matching technique for estimating arrival angle in [18] where the authors point to the possibility of exploiting temporal correlation by fully utilizing information from additional covariance matrix lags.

The underlying assumption of the WDOA algorithm is that sources are uncorrelated. Then the observed space-time DCM is taken to be a linear combination of the contributions from each source to the measured covariance matrix plus the noise covariance matrix of the space-time process. Let $\mathbf{r}_j(\theta) \in \mathbb{C}^{M\cdot W\times 1}$ be the j^{th} column of the modeled DCM given a source at angle θ and let $\hat{\mathbf{r}}_j \in \mathbb{C}^{M\cdot W\times 1}$ denote the j^{th} column of our measured DCM. We assume that our observation may be written as the following linear combination of vectors from our model and a bulk noise vector, $\boldsymbol{\varepsilon}_j$

$$\hat{\mathbf{r}}_j = \sum_{i}^{N_s} \gamma_i \mathbf{r}_j(\theta_i) + \boldsymbol{\varepsilon}_j, \tag{3-7}$$

Let $\mathbf{A}_j(\boldsymbol{\Theta})$ be the $M \cdot W \times N_{sig}$ complex-valued matrix whose columns correspond to the model of the j^{th} column of the space-time DCM given the sources with arrival angles $\boldsymbol{\Theta} = \left[\theta_1, \dots, \theta_{N_{sig}}\right]^T$. Then a least squares cost function is formulated from the following system of equations:

$$\boldsymbol{\varepsilon}_j = \hat{\mathbf{r}}_j - \mathbf{A}_j(\boldsymbol{\Theta})\boldsymbol{\gamma}, \tag{3-8}$$

The projection matrix $\mathbf{P}_{\mathbf{A}_j(\boldsymbol{\Theta})} = \mathbf{A}_j(\Theta)\left(\mathbf{A}_j^H(\boldsymbol{\Theta})\mathbf{A}_j(\boldsymbol{\Theta})\right)^{-1}\mathbf{A}_j^H(\boldsymbol{\Theta})$ takes a complex valued vector of length $M \cdot W$ and projects it onto the subspace spanned by the columns of $\mathbf{A}_j(\boldsymbol{\Theta})$, our model of the j^{th} column of the signal portion of the space-time DCM. The least squares estimate of the vector of DOAs, $\widehat{\boldsymbol{\Theta}}$, is obtained by minimizing the squared error between the observation of the j^{th} column of the DCM and the model,

$$J(\boldsymbol{\Theta}) = \hat{\mathbf{r}}_j^H \mathbf{P}^{\perp}_{\mathbf{A}_j(\boldsymbol{\Theta})} \hat{\mathbf{r}}_j. \tag{3-9}$$

To utilize all of the information about the correlation of the space-time process, (3-9) is modified to assign a cost for each column of the DCM:

$$J(\boldsymbol{\Theta}) = \sum_{j=1}^{M\cdot W} \hat{\mathbf{r}}_j^H P^{\perp}_{A_j(\boldsymbol{\Theta})} \hat{\mathbf{r}}_j, \tag{3-10}$$

where

$\boldsymbol{\Theta} = \left[\theta_1, \dots, \theta_{N_s}\right]$ is the $N_s \times 1$ vector of source directions,

$\hat{\mathbf{r}}_j \in \mathbb{C}^{M\cdot W\times 1}$ is the j^{th} column of the estimated space-time covariance matrix,

M is the number of sensors,

W is a widening factor,

$\mathbf{A}_j(\boldsymbol{\Theta})$ is the matrix whose columns correspond to the model of the jth column of the space-time covariance matrix in the directions specified by $\boldsymbol{\Theta}$ and

$\mathbf{P}^{\perp}_{\mathbf{A}_j(\boldsymbol{\Theta})} = \mathbf{I}_{M\cdot W} - \mathbf{A}_j(\Theta)\left(\mathbf{A}_j^H(\boldsymbol{\Theta})\mathbf{A}_j(\boldsymbol{\Theta})\right)^{-1}\mathbf{A}_j^H(\boldsymbol{\Theta})$ is the projection matrix onto the subspace that is orthogonal to the subspace spanned by the columns of $\mathbf{A}_j(\boldsymbol{\Theta})$.

An example of the WDOA cost function in the case of $N_s = 2$ is shown in the figure below. Here $-J(\boldsymbol{\Theta})$ is shown on a dB scale for convenience and was evaluated over a 128×128 grid of arrival angles obtained by uniformly sampling the wavenumber in the y-dimension, k_y. This cost function was obtained from a simulation assuming two 20 dB wideband sources with arrival angles given by the vector $\boldsymbol{\Theta} = [15°, 45°]$. The array geometry of the UWB depth sounder in the Basler configuration for the 2013 Antarctic mission was assumed. The source bandwidths were set to 250 MHz with the purpose of matching the parameters of that season.

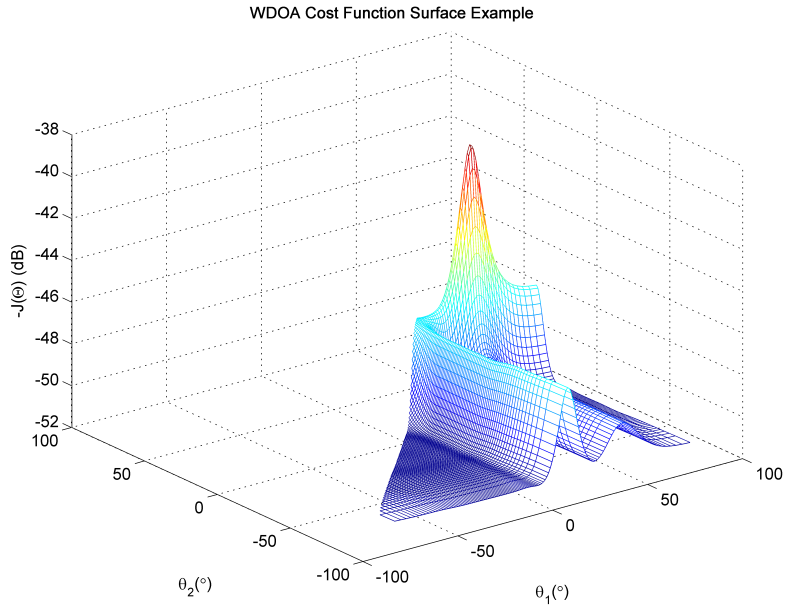

Figure 3-1 Cost function example for WDOA algorithm

From (3-10), an estimate of $\boldsymbol{\Theta}$ by solving the following optimization problem

$$\widehat{\boldsymbol{\Theta}} = \min_{\boldsymbol{\Theta}}\left\{\sum_{j=1}^{M\cdot W}\hat{\mathbf{r}}_j^H P^{\perp}_{\mathbf{A}_j(\boldsymbol{\Theta})}\hat{\mathbf{r}}_j\right\}. \qquad \textbf{(3-11)}$$

3.1.5 Computational Complexity

Obtaining a solution to Equation (3-11) requires a direct search of N_s dimensions to determine the global minimum of the cost function in (3-10). In theory the brute for solution would be obtained by evaluating $J(\boldsymbol{\Theta})$ for every possible solution $\boldsymbol{\Theta} = [\theta_1, \dots, \theta_{N_s}]$ in the search space to determine a global minimum. It is worth considering the computation complexity required for a single evaluation of $J(\boldsymbol{\Theta})$. To do this, we write Equation (3-10) in terms of the matrix $\mathbf{A}_j(\boldsymbol{\Theta})$

$$J(\boldsymbol{\Theta}) = \sum_{j=1}^{M \cdot W} \hat{\mathbf{r}}_j^H \hat{\mathbf{r}}_j - \hat{\mathbf{r}}_j^H \mathbf{A}_j(\boldsymbol{\Theta}) \left(\mathbf{A}_j^H(\boldsymbol{\Theta}) \mathbf{A}_j(\boldsymbol{\Theta}) \right)^{-1} \mathbf{A}_j^H(\boldsymbol{\Theta}) \hat{\mathbf{r}}_j. \tag{3-12}$$

To evaluate the complexity of Equation (3-12), the number of basic operations required to evaluate one term in the summation was analyzed and then multiplied by $M \cdot W$. Basic operations are real multiplications or additions. The number of real additions and multiplications required to perform three simple complex operations are summarized in the table below.

Table 1 Real additions and multiplications required for three simple complex operations

Operation	Input	Output	Real Operations	
			Multiplies	*Adds*
Complex multiplication	$x = a + j\,b,$ $y = c + j\,d,$	$z = x \cdot y$	4	2
Complex division	$x = a + j\,b,$ $y = c + j\,d,$	$z = x/y$	8	4
Complex addition	$x = a + j\,b,$ $y = c + j\,d,$	$z = x + y$	0	2

Equation **Error! Reference source not found.** requires for each term of the summation three different types of vector or matrix operations: a vector inner product, matrix multiplication and a matrix inversion. All of the quantities involved are complex and involve some combination of the simple complex operations in the table below. The real additions and multiplications required for these operations are stated below.

Table 2 Summary of types of complex vector and matrix operations need to evaluate cost function

Operation	Input	Output	Real Operations	
			Multiplies	*Adds*
Complex inner product	$\mathbf{x}, \mathbf{y} \in \mathbb{C}^{n\times 1}$	$z = \mathbf{x}^H \cdot \mathbf{y}$	$4n$	$2n$
Complex matrix multiplication	$\mathbf{C} \in \mathbb{C}^{m\times n}$ $\mathbf{D} \in \mathbb{C}^{n\times p}$	$\mathbf{Z} = \mathbf{C}\,\mathbf{D}$	$4mpn$	$2\,mp(n-1)$
Matrix inversion	$\mathbf{C} \in \mathbb{C}^{n\times n}$	$\mathbf{Z} = \mathbf{C}^{-1}$	$\frac{4}{3}n^3 + 6n^2 + \frac{2}{3}n$	$\frac{4}{3}n^3 + 4n^2 - 2n$

The total number of basic operations, S, (taken to be real multiplications or additions) required for one evaluation of the cost function was determined assuming the Gauss-Jordan method for matrix inversion (which would be a worst case or most complex implementation). It is written here in terms of the dimensional variables of interest

$$S = 2(3N_s^2 + 5)(M \cdot W)^2 + \left(\frac{8}{3}N_s^3 + 10\,N_s^2 - \frac{10}{3}N_s - 2\right)(M \cdot W). \quad \textbf{(3-13)}$$

Recall that M refers to the number of sensors, W is the widening factor and N_s is the number of sources. For the Basler configuration in 2013, M = 8 and W = 3. N_s is most commonly taken to be 2 but seldom exceeds 4. Often times the matrix inverse operation is attributed as the dominant factor determining an algorithm's computational complexity. It was found however that the inversion of the $N_s \times N_s$ complex matrix $\mathbf{B} = \mathbf{A}_j^H(\boldsymbol{\Theta})\mathbf{A}_j(\boldsymbol{\Theta})$ did not set the order of complexity. To illustrate this, Equation (3-13) is expressed as the sum of two terms, S_1 and S_2. S_1 totals all of the basic operations required to do the matrix inversion of $\mathbf{B}$ and S_2 is used to describe the basic operations required to do everything else. These are

$$S_1 = \left(\frac{8}{3}N_s^3 + 10\,N_s^2 - \frac{4}{3}N_s\right)(M \cdot W), \quad \textbf{(3-14a)}$$

$$S_2 = 2MW(MW-1)N_s^2 + 2MW(MW-1)N_s + 2MW(5MW-1). \quad \textbf{(3-14b)}$$

Evaluation of S_1 and S_2 for $1 \le N_s \le 4$ for fixed values of M and W showed that the complexity was not dominated by the matrix inversion.

An example is provided in Figure 3-2 to show the order of complexity, $O(\log L)$, with L being the number of basic operations either S, S_1, or S_2 as N_s varies from 1 to 20 for $M = 8$ and $W = 3$. In practice,

N_s would not take values larger than M but was allowed to here for the purpose of determining at what point the matrix inversion would dominate the complexity associated with one evaluation of the cost function. As this result shows, over the envelope of possible values of N_s the complexity is dominated by the real additions and multiplications associated with the inner product and the matrix multiplication operations. The matrix inverse operation would be the driving factor in the complexity if N_s were allowed to take values larger than 15. This provides some insight into the algorithm improvements that would speed up evaluation of the cost function (thereby speeding up convergence to a solution). The result suggests that focusing on doing efficient matrix multiplies will likely have a greater impact on the improvement of overall execution times.

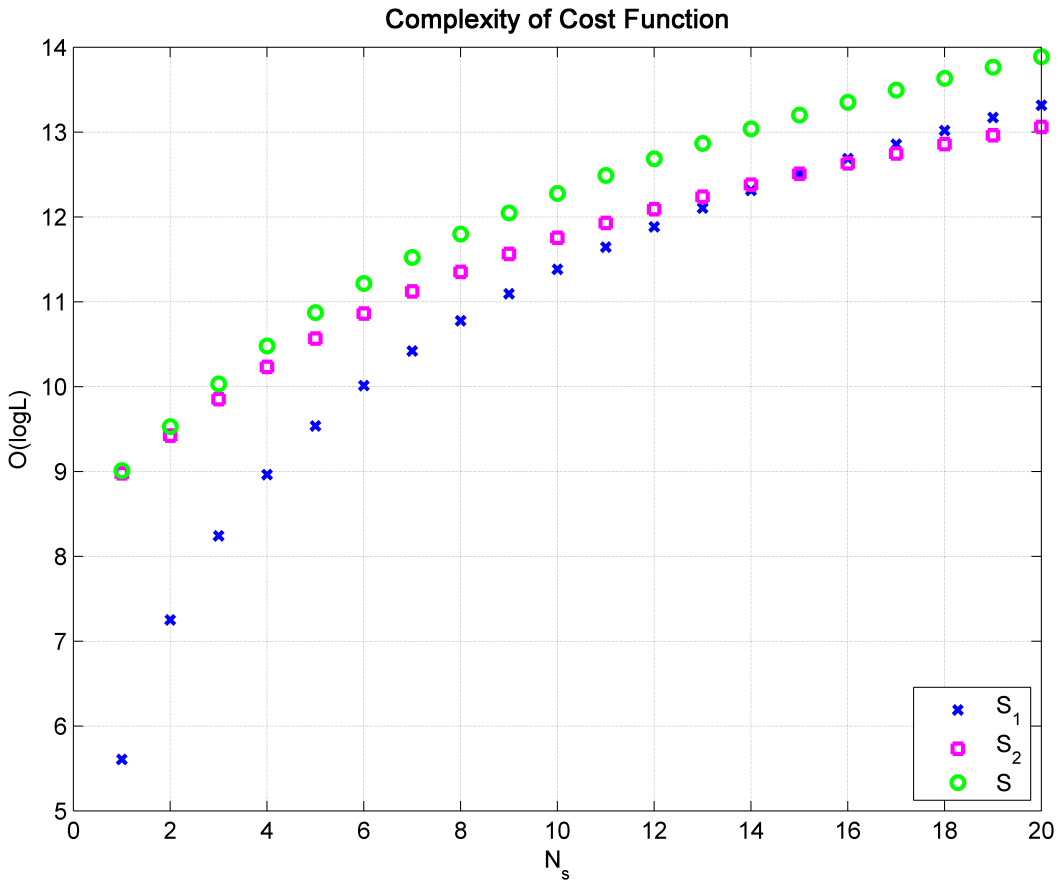

Figure 3-2 Cost function complexity with increasing N_s

3.1.6 Algorithm

The feasibility of applying the WDOA algorithm to real data hinges on our ability to effectively search N_s dimensions for the solution. This section describes the implementation of the WDOA algorithm that has been integrated into the CReSIS software. The block diagram in Figure 3-3 offers a general description of the WDOA algorithm that is performed at the pixel level. For every (u, ρ) pair in the scene, the WDOA algorithm starts by building a matrix of space-time snapshots that is used to estimate the space-time DCM. The DCM is then used to obtain an initial estimate of (3-11) which in turn initializes some numerical solver used to find the minimum of $J(\boldsymbol{\Theta})$. *Both initialization and minimization assume N_s to be known a priori.*

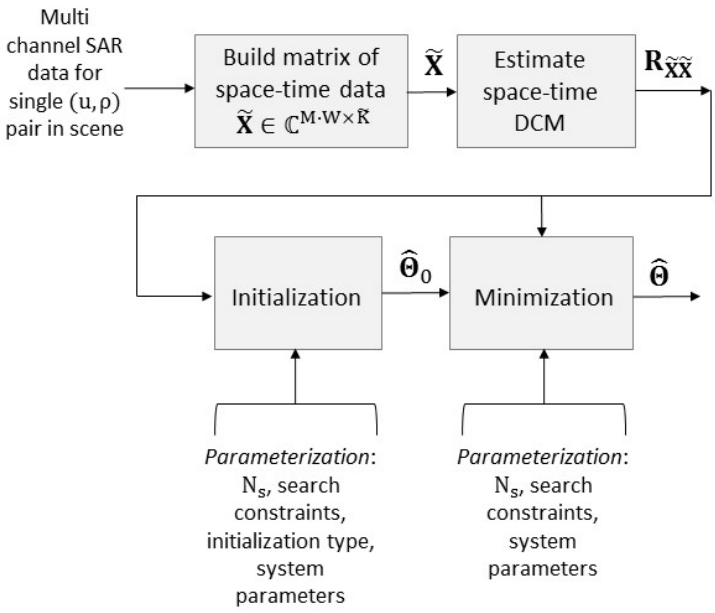

Figure 3-3 Block diagram for WDOA algorithm

Initialization

Initialization is a critical part of minimizing the cost function for two reasons. It directly influences accuracy of the final solution as well as computation speed. Since an exhaustive search of N_s dimensions for every pixel in the scene is not realizable in practice, we must rely on a smart search algorithm to find the minimum of the cost function. This is done by obtaining some initial estimate of the global minimum that is refined with a local minimization. Initialization informs the minimization algorithm of where to start its search. If the initial value is poor, the algorithm may converge a nearby minimum that does not correspond to the true solution (at the global minimum) leading to an erroneous estimate. Also a good initial value means that the subsequent search can converge to the solution in fewer iterations (i.e. fewer evaluations of the cost function).

Two possible approaches have been considered for the initialization stage: coarse grid evaluation and an Alternating Projection (AP) method. The former involves evaluation of the cost function over a coarse grid DOAs (chosen such that the sampling of the k_y dimension satisfies Nyquist) and then determining the initial estimate to be the global minimum of that coarse evaluation. Let N_{grid} be the number points on the grid in a single dimension. Then in the coarse grid method, the cost function is evaluated at $(N_{grid})^{N_s}$ points in the solution space. Figure 3-1 is an example of a grid evaluation of $J(\boldsymbol{\Theta})$ where $N_{grid} = 128$ was used leading to a 128×128 mesh of evaluation points. During initialization though, we just want to get in the neighborhood of the solution which can be achieved with a much smaller value of N_{grid}. During processing N_{grid} was set to 24 or 48.

The AP style initialization draws from the methods presented in [6]. This approach breaks the minimization down into N_s successive one-dimensional evaluations of the cost function. An example is described here for $N_s = 2$ using Figure 3-4. The notation $\hat{\theta}_i^{(0)}$ is used to denote the initialization value of the i^{th} source.

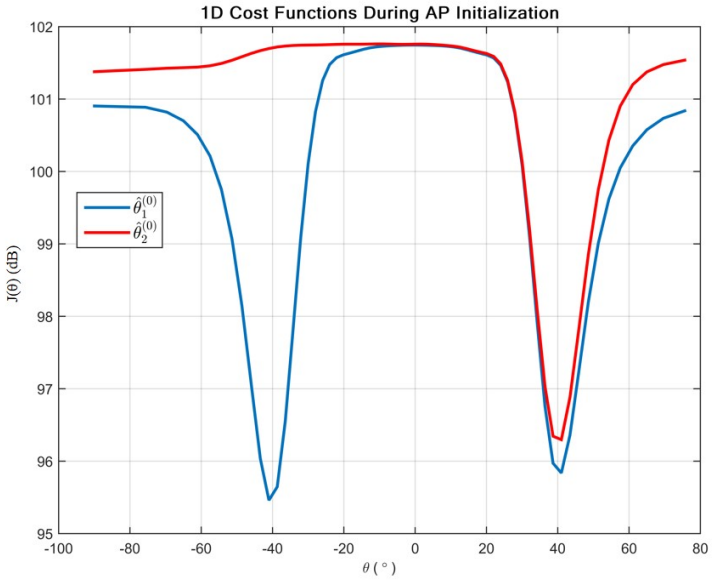

Figure 3-4 Alternating projection style initialization

On the first iteration, the problem is solved for a single source, meaning the $\mathbf{A}_j(\boldsymbol{\Theta})$ matrix is taken to be $\mathbf{A}_j(\theta_1)$, a single $M \cdot W$ column vector representing our model of the j^{th} column of the DCM as a function of the variable θ_1. In this case we obtain the following problem:

$$\hat{\theta}_1^{(0)} = \min_{\theta_1} \left\{ \sum_{j=1}^{M \cdot W} \hat{\mathbf{r}}_j^H P_{\mathbf{A}_j(\theta_1)}^{\perp} \hat{\mathbf{r}}_j \right\},$$

Leading to an initial value $\hat{\theta}_1^{(0)} \approx -40°$. The argument of the minimization above appears in Figure 3-4 as the blue curve. On the initialization of the first source, the deepest null is chosen. On the second iteration, we fix $\hat{\theta}_1^{(0)}$ and allow θ_2 to be variable. The matrix $\mathbf{A}_j(\boldsymbol{\Theta})$ is evaluated as $\mathbf{A}_j\left(\theta_2, \hat{\theta}_1^{(0)}\right)$ and the problem becomes

$$\hat{\theta}_2^{(0)} = \min_{\theta_2} \left\{ \sum_{j=1}^{M \cdot W} \hat{\mathbf{r}}_j^H P_{\mathbf{A}_j\left(\theta_2, \hat{\theta}_1^{(0)}\right)}^{\perp} \hat{\mathbf{r}}_j \right\}.$$

The result of holding $\hat{\theta}_1^{(0)}$ fixed and allowing θ_2 to be variable, is that the cost function $J\left(\theta_2, \hat{\theta}_1^{(0)}\right)$ shown in red is projected orthogonally to the first value. This is visible in the figure where we can see that the null associated with the first source has been suppressed and the minimum is $\hat{\theta}_2^{(0)} = 40°$.

The AP style initialization appears capable of performing the initialization stage with fewer evaluations of $J(\boldsymbol{\Theta})$. In the coarse grid initialization, $\left(N_{grid}\right)^{N_s}$ evaluations are required while the AP initialization only requires $N_s \cdot N_{grid}$ evaluations. It should be noted that during simulation, it was observed that the success of the AP method for initializing the i^{th} source hinged on the ability to project orthogonally to all of the $\hat{\theta}_k^{(0)}, k \neq i$. The projection was poor when any of the other initialized sources were just a few degrees off of the true DOAs. Poor projection performance appeared like leakage from the previously estimated sources. This commonly occurred when MATLAB's *min* function was used to find the nulls of $J(\theta)$. To handle this, MATLAB's *min* function was used to get near a null and then adjacent points were used to fit a second order polynomial to the null to refine the coarse estimate. When the AP method was implemented in this fashion, N_{grid} could be made as low as 24.

3.1.7 Cost Function Minimization

During the initial testing of the WDOA algorithm, the Alternating Projection algorithm presented by Ziskind and Wax [6] was used for minimizing the cost function. The AP algorithm is a direct search method that starts at the initialization point and moves iteratively through the search space along the contours of the cost function along directions that are parallel to the axes. An example showing the successive iterations was recreated from an identical figure in [6] and is show here in to illustrate the convergence to a solution for a 2-dimensional cost function. Like the initialization technique, each iteration involves a 1D grid search.

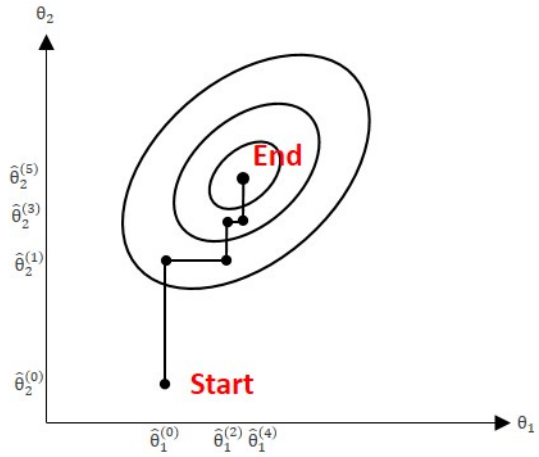

Figure 3-5 Illustration of AP search of 2D cost function, recreated from an identical figure in [6]

Early tests found the MATLAB implementation to be too slow even in a simulated environment. In [6] the authors present a projection matrix update equation that reduces some of the expensive computations and facilitates easier vectorization of variables in MATLAB (thereby eliminating the requirement of one of the for loops). This notion was adapted to our problem but the computation was still too expensive. This was largely due to the overhead of calling MATLAB functions during the search. The AP method was eventually abandoned during testing but is mentioned here for completeness.

MATLAB's fmincon

MATLAB's Optimization Toolbox provides functionality for numerically solving optimization problems by finding the parameters that maximize or minimize an objective subject to some constraints. These libraries are already designed to be fast and efficient making them more attractive for applying to the WDOA algorithm. MATLAB has made available comprehensive documentation on this toolbox [19] which helps users select the appropriate solver for an optimization problem and offers examples on parameterization.

MATLAB's *fmincon* function was chosen to execute the minimization. The *fmincon* function finds the minimum of a constrained nonlinear multivariable function. Given the cost function $J(\theta)$ and a set of constraints, *fmincon* formulates the following constrained minimization problem

$$\min_{x} J(x) \text{ such that } \begin{cases} \text{i).} & c(x) \leq 0, \\ \text{ii).} & c_{eq}(x) = 0, \\ \text{iii).} & A \cdot x \leq b, \\ \text{iv).} & A_{eq} \cdot x = b_{eq}, \\ \text{v).} & lb \leq x \leq ub. \end{cases}$$

In the WDOA algorithm, constraints i) and v) are specified while constraints ii) through iv) are left unspecified. Constraint i) is a non-linear constraint that was used to impose a guard band to avoid repeated solutions in the vector of DOAs that would lead to linear dependence of the columns of $\mathbf{A}(\boldsymbol{\Theta})$. This would arise when the value of N_s was not properly set and caused the minimizer to fail. The non-linear constraint file forces the solver to find N_s unique solutions that must each be separated by a minimum of θ_{guard}.

This requirement was found to be most important in processing the nadir beam. Typically N_s was set to 2 for imaging near nadir with the intent of separating echoes from the left and right sides. At nadir before the annulus opens at the ice-bed interface, there is generally one dominant source (i.e. $N_s \neq 2$). The non-linear constraint forces the solver to find 2 unique solutions, however one of them will be not be useful. This presents a challenge in later stages of imaging when the scattering pixels are picked from the point cloud of DOAs. Handling this situation near nadir needs improvement. One possibility would be to identify a quality measure that would allow us to identify these bad pixels after array processing. An alternative, and perhaps better, approach would be to estimate N_s before the DOA estimation but this would increase complexity and was left for future work.

Constraint iv) serves to bound a solution within an interval. This speeds up convergence and in some cases may improve performance when the true DOA solution appears at a local minimum does not correspond to the global minimum of the cost function. This was used to impose a search window on the j^{th} source by searching for the solution over an interval $\left[\theta_{\text{lb}} \leq \theta_j \leq \theta_{\text{ub}}\right]$. The limits θ_{lb} and θ_{ub} were determined for each range bin from a window about the incidence angle, $\theta_{\text{mid}}(\rho)$, along the surface of interest (the air-ice interface or ice-bed interface for example) based on the two-way propagation time of the pixel being processed assuming a flat surface. The range-dependent lower and upper bounds were determined as

$$\theta^j_{\text{lb}}(\rho) = \theta^j_{\text{mid}}(\rho) + \theta^j_1,$$

And

$$\theta^j_{\text{ub}}(\rho) = \theta^j_{\text{mid}}(\rho) + \theta^j_2,$$

Where θ^j_1 and θ^j_2 are user defined angular bounds about the incidence angle $\theta^j_{\text{mid}}(\rho)$.

Figure 3-6 is used to illustrate the DOA constraints. This figure shows a tomographic slice obtained from one range line of high-altitude, multibeam data collected over Whillians ice stream. This result corresponds to returns from the right beam. Two sources were assumed: one from air-ice interface to the right side and one from the ice-bed interface to the right side. DOA estimation was restricted to a set of

range bins that starts slightly before the bed echo and extends far enough to capture the basal scattering. Range bin restriction is discussed in the following section. $\hat{\theta}_{surf}$ and $\hat{\theta}_{bed}$ are the estimated arrival angles of the surface and basal echoes obtained from searches within their respective bounds. The bed begins echoing at approximately the 1135^{th} range bin. As range increases, the trend of $\hat{\theta}_{bed}$ extends further off nadir and becomes noisier approaching the edge of the half-power beamwidth at $-30\,°$

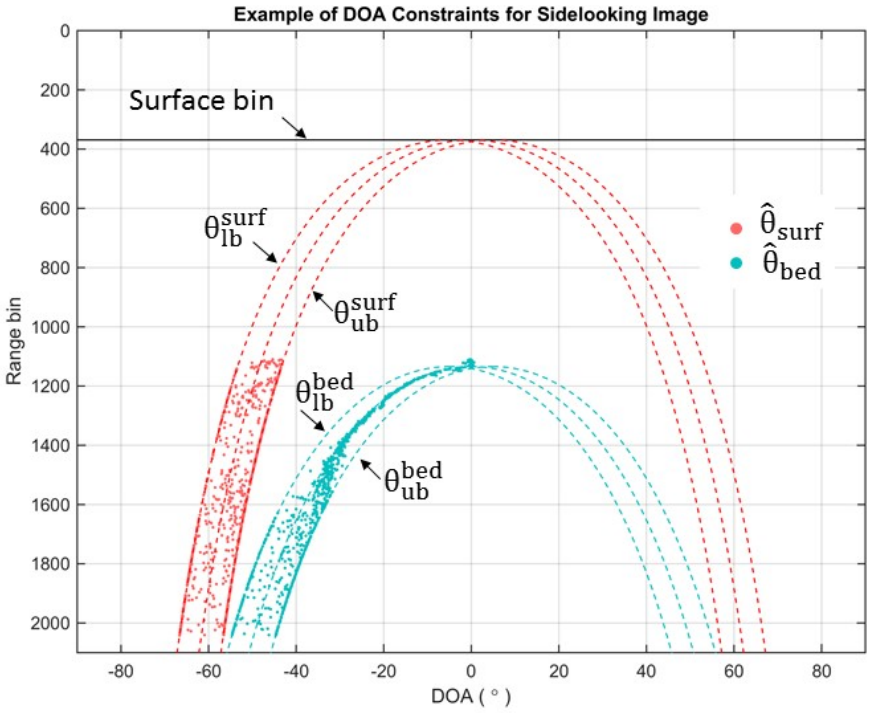

Figure 3-6 Example of DOA constraints for one range line in sidelooking image

3.1.8 Bin Restriction

The WDOA algorithm is computationally expensive because the cost function must be evaluated many times to converge to a solution for each pixel in the scene. In our application, the multichannel data is organized into segments that are then broken into frames which typically cover 30 to 50 km sections of a scene. Frames are further broken into 5 km chunks. Our existing processing works on frames so for an implementation of (3-11) in the framework of our processing to be feasible, it must be able to process a frame in a reasonable time period (i.e. less than a day). For the 2013 Basler mission, the SAR focused outputs of one chunk have dimensions 9812×2010 or 19,722,120 pixels. This means that to assign a direction of arrival to every pixel in our scene using the WDOA algorithm using a direct search would require exhaustively searching N_s dimensions 197,722,120 times for a frame containing 10 chunks.

But we are really only interested in assigning a DOA to those pixels containing basal scattering. In an effort to reduce computation time, functionality was added to the array processing stage of the CReSIS toolbox that was used to restrict the bins that were processed during imaging. Processing was restricted between two layers that were created in the picker interface. Picks were made on echograms obtained by multilooking across the array. Incoherently combining the channels is equivalent to forming a product that is unfocused across the track and provides a quick way to get an idea regarding the fast-time extent of the basal scattering.

An example of the multilooked outputs are presented that correspond to the focused sounder profile from Kamb that was combined using MUSIC beamforming shown in Figure 3-7. This is in an area where the bed is very rough. The roughness is revealed in the multilook images for the left and right beams shown in Figure 3-8 and Figure 3-9 respectively. The unique features of each side are observable. These images show the bins used to restrict the tomography during array processing.

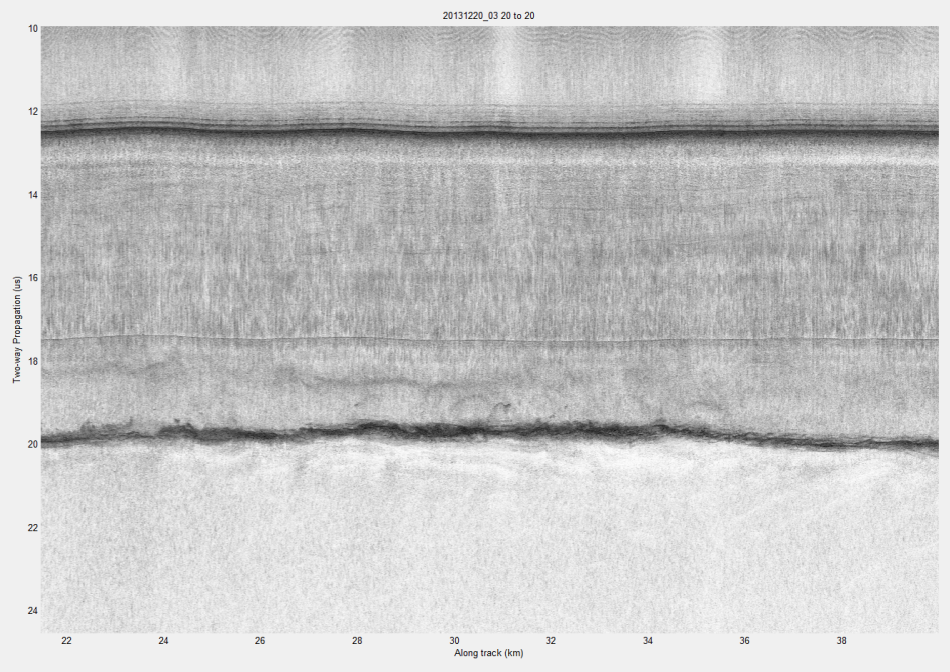

Figure 3-7 MUSIC sounder profile from Kamb

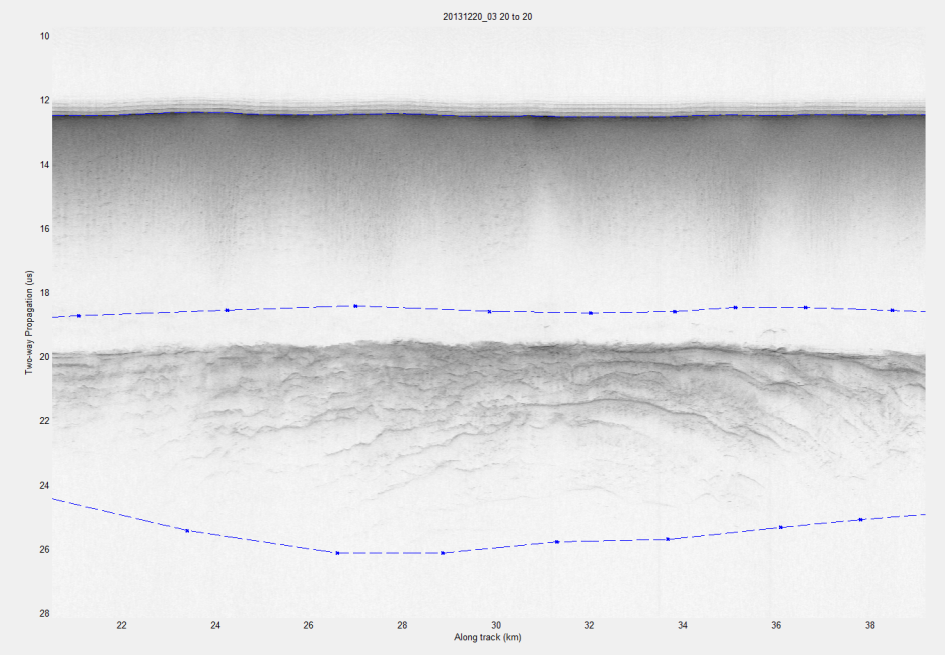

Figure 3-8 Multilook image from left

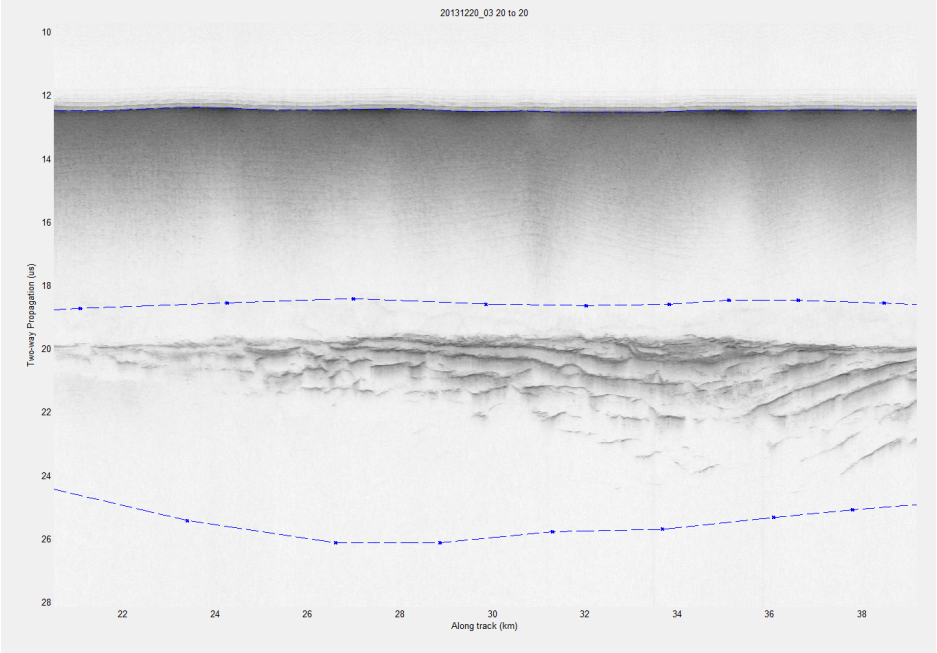

Figure 3-9 Multilook image from right

3.2 Estimation of SNR of Wideband Sources

Over the course of the project, it became apparent that having some measurement of source SNR was important for improving the surface extraction stage of the imaging process. From a point cloud of noisy DOAs, SNR can be used a measure of quality in order to pick out scattering pixels from noise. The additional functionality of estimating source SNR is also an important step towards future efforts to estimate basal conditions at the ice-bed interface. A relative SNR measurement of each source is obtained using the DOA estimates. The method outlined here is a first order approach that could be refined in the future.

To estimate the SNR for the j^{th} source, the array was first registered to the j^{th} target. This was achieved by first using a sinc interpolation kernel (generally 20 taps long) to co-register the signal on each channel. Let $x_m(n)$ be the discretized range line from the m^{th} channel and let $\tau_m(\hat{\theta}_j)$ represent the propagation delay between the origin and sensor m in the direction $\hat{\theta}_j$. The reconstructed signal $x_m^r(t)$ is obtained as

$$x_m^r(t) = \sum_{n-(N_{taps}-1)/2}^{n+(N_{taps}-1)/2} x_m(n)\mathrm{sinc}\left(\frac{t-nT_s}{T_s}\right).$$

The vector measurements, $\mathbf{x_{reg}}(n)$, registered to a source at $\hat{\theta}_j$

$$\mathbf{x_{reg}}(n) = \begin{bmatrix} x_1\left(\tau_1(\hat{\theta}_j)\right) \\ \vdots \\ x_8\left(\tau_8(\hat{\theta}_j)\right) \end{bmatrix}$$

$$= \begin{bmatrix} \sum_{n-(N_{taps}-1)/2}^{n+(N_{taps}-1)/2} x_1(n)\mathrm{sinc}\left(\frac{\tau_1(\hat{\theta}_j)-nT_s}{T_s}\right) \\ \vdots \\ \sum_{n-(N_{taps}-1)/2}^{n+(N_{taps}-1)/2} x_8(n)\mathrm{sinc}\left(\frac{\tau_8(\hat{\theta}_j)-nT_s}{T_s}\right) \end{bmatrix}.$$

The received signal from $\hat{\theta}_j$ is denoted as $s_j(t)$. Samples of the estimated signal are denoted as $\hat{s}_j(n)$. This quantity is estimated from the registered measurement vector using the MLE beamformer in Equation (2-19), obtained when a weight vector

$$\mathbf{w} = \left(\mathbf{V}^H(\boldsymbol{\Theta})\mathbf{V}(\boldsymbol{\Theta})\right)^{-1}\mathbf{V}^H(\boldsymbol{\Theta}), \quad \textbf{(3-15)}$$

is used to estimate the vector of sources as

$$\hat{\mathbf{s}}(\mathrm{n}) = \left(\mathbf{V}^{\mathrm{H}}(\boldsymbol{\Theta})\mathbf{V}(\boldsymbol{\Theta})\right)^{-\mathbf{1}} \mathbf{V}^{\mathrm{H}}(\boldsymbol{\Theta})\mathbf{x}(\mathrm{n}). \tag{3-16}$$

Here $\hat{\mathbf{s}}(\mathrm{n})$ is the $\mathrm{N_s}\times 1$ vector containing samples of the received signals at discrete time n

$$\hat{\mathbf{s}}(\mathrm{n}) = [\hat{\mathrm{s}}_1(\mathrm{n}) \quad \ldots \quad \hat{\mathrm{s}}_{\mathrm{N_s}}(\mathrm{n})]^{\mathrm{T}}$$

and $\mathbf{V}(\boldsymbol{\Theta})$ is the $\mathrm{M}\times\mathrm{N_s}$ matrix of *narrowband* steering vectors, i.e.

$$\mathbf{V}(\boldsymbol{\Theta}) = \left(\frac{1}{\sqrt{\mathrm{M}}}\right)\begin{bmatrix} e^{j2\pi f_c \tau_1(\theta_1)} & \cdots & e^{j2\pi f_c \tau_1(\theta_{N_s})} \\ \vdots & \cdots & \vdots \\ e^{j2\pi f_c \tau_M(\theta_1)} & \cdots & e^{j2\pi f_c \tau_M(\theta_{N_s})} \end{bmatrix}.$$

Equation (3-16) is modified so that a vector of measurements that are registered to the j^{th} source $\mathbf{x_{reg-j}}(\mathrm{n})$ may be used to estimate $\mathrm{s_j}(\mathrm{n})$. A vector $\mathbf{g}$ is defined as the $\mathrm{N_s}\times 1$ vector whose only non-zero entry is in the j^{th} place that serves to preserve only the signal to which the array is registered. Then $\hat{\mathrm{s}}_\mathrm{j}(\mathrm{n})$ is computed as

$$\hat{\mathrm{s}}_\mathrm{j}(\mathrm{n}) = \mathbf{g}^{\mathrm{T}}\left(\mathbf{V}^{\mathrm{H}}(\boldsymbol{\Theta})\mathbf{V}(\boldsymbol{\Theta})\right)^{-\mathbf{1}} \mathbf{V}^{\mathrm{H}}(\boldsymbol{\Theta})\mathbf{x_{reg-j}}(\mathrm{n}),$$

And the estimated SNR of the j^{th} source, $\widehat{\mathrm{SNR}}_\mathrm{j}$, is taken to be the expectation of the inner product of $\hat{\mathrm{s}}_\mathrm{j}(\mathrm{n})$ obtained by estimating the following quantity

$$\mathrm{SNR_j} = \mathrm{E}\{\hat{\mathrm{s}}_\mathrm{j}^*(\mathrm{n})\hat{\mathrm{s}}_\mathrm{j}(\mathrm{n})\}.$$

3.3 Chapter Summary

A space-time formulation was presented for the wideband imaging problem. In this formulation, a space-time vector was constructed with multiple consecutive temporal samples of the array measurements and used to estimate a space-time data covariance structure. It was shown that the space-time DCM contains samples of the cross-correlation function between sensors at zero lag and also at non-zero lags. A wideband DOA estimation method was presented that obtains an estimate of the wideband source arrival angles by fitting the observation of the space-time DCM to a model through the minimization of a least-squares type cost function. The computational complexity of the cost function was analyzed and an algorithm for solving the WDOA minimization problem was presented that uses MATLAB's optimization solver following a coarse grid initialization. Techniques for speeding up convergence to a solution were offered. Finally a first order approach for estimating the average SNR of a wideband source was presented that used registration followed by the pseudoinverse.

Chapter 4

Simulations

A MATLAB based simulator was developed for the purpose of studying direction of arrival estimation in wideband signal environments. The simulation setup is overly simplified in the sense that wideband sources are modeled as reflections from point targets and sensors are assumed to be isotropic radiators. The outcomes of several Monte Carlo experiments are used to compare the WDOA to the three other DOA estimators: narrowband MUSIC, narrowband MLE and the wideband version of MLE. The results offer insight into the best-case DOA estimation performance. This chapter describes how multichannel array data were simulated. An overview of the wideband MLE (WBMLE) method is also offered. The Monte Carlo experiments are described and results are presented. The chapter concludes with summarizing remarks about the four compared methods drawn from observations.

4.1 Simulating Multichannel Array Data

Multichannel array data are simulated by first generating a set of N_s signals, $\{s_1(t), \dots, s_{N_s}(t)\}$, whose arrival angles are $\theta_1, \dots, \theta_{N_s}$. The reference signals are taken to be the complex envelopes of those signals that would be observed at some origin of the array, generally taken to be the center, or defined such that it coincides with the location of the array's transmit phase center. We assume that each signal is wide-sense stationary (WSS) over some observation interval. The i^{th} signal is then modeled as a zero-mean, complex Gaussian random process whose real and imaginary components are jointly WSS, each with variance σ_i^2 given by $\sigma_i^2 = \frac{\gamma_i}{2}$, where γ_i refers to the average SNR of source i.

The method used to simulate the spectrum of $x_m(t)$, (the complex envelope of the m^{th} sensor) is summarized in Figure 4-1 below. The signal, $x_m(t)$, is modeled as the superposition of the set of signals measured at the m^{th} element, $\{s_1(t - \tau_m(\theta_1)), \dots, s_{N_s}(t - \tau_m(\theta_{N_s}))\}$, and complex Gaussian noise,

convolved with the system response of the radar. In simulation, the i^{th} source is time shifted by imposing true time delays in the Fourier domain at passband. Let $S_i(f)$ denote the Fourier transform of $s_i(t)$. Then the time shifted signal $s_i(t - \tau_m(\theta_i))$ is evaluated as $s_i(t - \tau_m(\theta_i)) = \mathcal{F}^{-1}\{S_i(f)e^{-j2\pi f\tau_m(\theta_i)}\}$, $f_0 \leq f \leq f_1$. Realization of true time delays in this fashion allows for simulation of wideband signal environments.

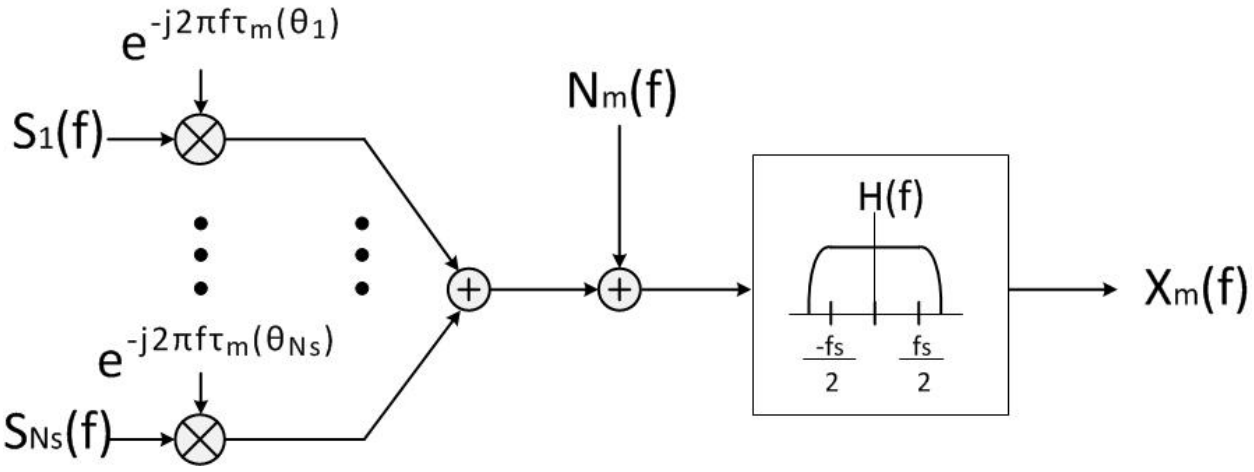

Figure 4-1 Block diagram describing simulation of the spectrum of a single channel's complex envelope

The simulator that was implemented for this thesis uses H(f) to model frequency domain windowing applied in pulse compression. Non-rectangular windowing broadens a pulse slightly that is reflected from a target, which then may influence the widening factor. A rectangular window was used to characterize performance and a Hanning window was used to validate that the same performance was achieved with windowing.

What has been described above is the method for simulating the complex envelope of the m^{th} receiver, $x_m(t)$ and since the bandwidth of H(f) is equal to the sampling frequency f_s, then the simulator is more specifically providing the samples of the envelope $x_m(nT_s)$. Then the multichannel array data are the set of the m envelopes sampled at $t = nTs$, or the snapshot of the array $t = nTs$. The vector $\mathbf{x}(n)$ is used to describe the $M \times 1$ vector containing samples of the envelopes at discrete time n

$$\mathbf{x}(n) = [x_1(nTs), \dots, x_m(nTs)]^T.$$

The matrix $\mathbf{X}(n) \in \mathbb{C}^{M \times K}$ is then used to describe the matrix containing K temporal snapshots of the array, i.e.

$$\mathbf{X}(n) = \left[\mathbf{x}(n), \mathbf{x}(n-1), \dots \mathbf{x}\left(n - (K-1)\right)\right].$$

Figure 4-2 summarizes the arguments of the MATLAB function used to simulate the matrix of array data, $\mathbf{X}(n)$. The function is passed two sets of parameters. The observation parameters, indicated with a

blue bracket, include sampling frequency, bandwidth, window function, and the position vectors of each sensor in the cross-track dimension. The target parameters required to generate the array data are indicated with a red bracket and include source DOAs, source SNRs and the number of snapshots, K.

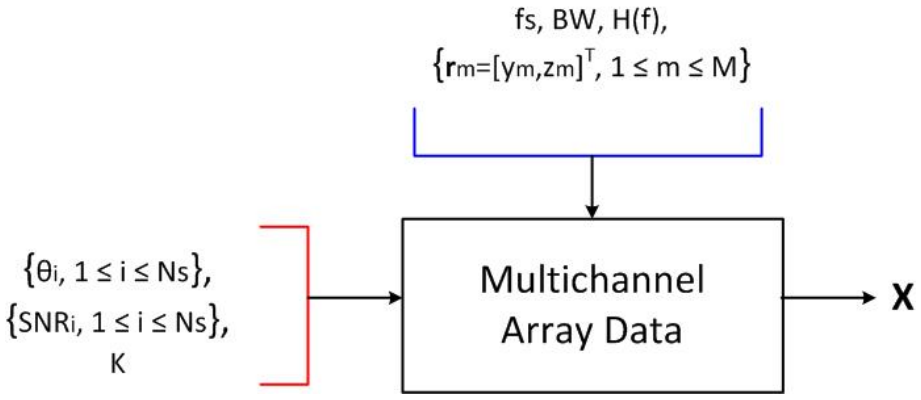

Figure 4-2 Array data simulator block diagram

4.2 Direction of Arrival Simulations

The array data simulator was used to conduct a set of experiments meant to characterize the performance of the wideband (WB) direction of arrival estimator. It was compared to the two narrowband DOA estimators that have been used in ice-bed tomographic imaging: MUSIC and MLE. Additionally, a wideband version of MLE (WBMLE) was implemented so that the technique could be compared to an optimal wideband estimator. MUSIC and MLE were discussed in Chapter 2. A brief description of the WBMLE algorithm is presented later in this section for completeness.

4.2.1 Monte Carlo Experiments

The performance of the WDOA technique is characterized by comparing its performance with MUSIC, MLE and WBMLE in several simulation based experiments. In all experiments, sources are assumed to be uncorrelated. The array is taken to be composed of isotropic elements. The system parameters of the UWB during the 2013 Antarctic mission are used to set the geometry of the array, bandwidth, sampling frequency and windowing applied in pulse compression.

Each experiment is designed to test the performance of the DOA estimators as a function of some varying parameter of a wideband source (such as arrival angle θ, source SNR, or snapshots). For every hypothesis parameter, a random number generator is reseeded and a set of multichannel data is generated using the function described earlier. These data are to estimate the DOA with each of the tested methods. Each value of a parameter is tested over N_{runs} trials or runs. With every run a new set of random

multichannel data is generated. Between each tested value, the random number generator is reseed. In other words, for each value of a parameter under test, the multichannel data are obtained from the same set of random numbers. This ensures that the error can be attributed to the variations of the test parameter and not the random number generator.

The metric used to assess performance is the root-mean-squared error for each direction of arrival. Let $\hat{\theta}_i(n)$ denote the estimate of a particular method of the i^{th} source measured on the n^{th} run. The RMSE of this source is computed as

$$\mathrm{RMSE}_i = \sqrt{\frac{1}{N_{runs}} \sum_{n=1}^{N_{runs}} \left|\hat{\theta}_i(n) - \theta_i\right|^2},$$

And the units are either in degrees or radians depending on the units of the DOA estimates.

4.2.2 Notations

Because the WMLE method works on the array data in the Fourier domain, some confusion may arise with notation. Up to this point, the matrix $\mathbf{X} \in \mathbb{C}^{M \times K}$ has been used to denote the $M \times K$ matrix of complex values containing measurements made by the array over K snapshots

$$\mathbf{X} = \begin{bmatrix} x_1(n) & x_1(n-1) & \cdots & x_M\big(n-(K-1)\big) \\ \vdots & \vdots & \vdots & \vdots \\ x_M(n) & x_M(n-1) & \cdots & x_M\big(n-(K-1)\big) \end{bmatrix}.$$

To avoid confusion of $\mathbf{X}$ with the frequency domain variables needed to describe WBMLE, the variable $\mathbf{X}_{td}$ is introduced to denote the matrix of temporal snapshots.

4.2.3 Wideband MLE

In the WBMLE method, the time series of array data are conditioned into N_b frequency domain snapshots so that at each discrete frequency, a linear model of the array holds. This is realized by observing the multichannel data over a time interval $T_{obs} = K \cdot T_s$. The variable K is the number of temporal snapshots of the array observed over T_{obs} and T_s is the sampling interval. The total observation interval is broken down into P subintervals of duration T_{sub} such that $P \cdot T_{sub} = T_{obs}$.

Within every subinterval, the DFT is computed for each channel and the data are reorganized into frequency domain snapshots. The number of frequency domain snapshots is determined by the number of time samples within the duration of T_{sub}, i.e.

$$N_b = T_{sub} \cdot f_s.$$

The resolution bandwidth of the frequency domain snapshots or the subband is determined by the duration of the subinterval as

$$\Delta f = \frac{1}{T_{sub}} = \frac{f_s}{N_b}. \tag{4-1}$$

The range of frequencies within the j^{th} subband are then given by $f_j - \frac{\Delta f}{2} \leq f \leq f_j + \frac{\Delta f}{2}$. The number of bands is chosen such that each subband is approximately narrowband.

The p^{th} frequency domain snapshot containing the spatial samples at the discrete frequency f_j is represented as the $M \times 1$ vector of complex values given by

$$\mathbf{X}_{(p)}(f_j) = \left[X_1^{(p)}(f_j), \dots, X_M^{(p)}(f_j)\right].$$

Here, $X_m^{(p)}(f_j)$ is the value of the DFT of channel m at the discrete frequency f_j from the p^{th} subinterval. The frequency domain snapshot model due to N_s wideband sources received from arrival angles $\boldsymbol{\Theta} = \left[\theta_1, \dots, \theta_{N_s}\right]^T$ may then be written as the following linear system of equations

$$\mathbf{X}_{(p)}(f_j) = \mathbf{A}(\boldsymbol{\Theta}, f_j)\mathbf{S}_{(p)}(f_j) + \mathbf{N}_{(p)}(f_j), \qquad \text{for } j = 1, \dots, N_b \text{ and } p = 1, \dots, P. \tag{4-2}$$

where,

$$\mathbf{S}_{(p)}(f_j) = \left[S_1^{(p)}(f_j), \dots, S_{N_s}^{(p)}(f_j)\right]^T,$$

and

$$\mathbf{N}_{(p)}(f_j) = \left[N_1^{(p)}(f_j), \dots, N_M^{(p)}(f_j)\right]^T$$

Are the vectors containing the DFT coefficients of the sources and noise respectively at the j^{th} subband obtained from the p^{th} subinterval and $\mathbf{A}(\boldsymbol{\Theta}, f_j) \in \mathbb{C}^{M \times N_s}$ is the matrix containing the frequency dependent steering vectors for the subband centered at the discrete frequency f_j.

At each subband, the sample covariance matrix $\mathbf{R}_{\mathbf{XX}}(f_j)$ is estimated as

$$\widehat{\mathbf{R}}_{\mathbf{XX}}(f_j) = \frac{1}{P}\sum_{p=1}^{P} \mathbf{X}_{(p)}(f_j)\mathbf{X}_{(p)}^H(f_j), \tag{4-3}$$

The implication of Equation (4-3) is that the multichannel random process in Equation (2-1) remains stationary over all subintervals.

The standard assumptions described in Chapter 2, **A1-A3,** are made. Additionally the following assumptions are required for the maximum likelihood estimator of wideband sources [20]:

A4$_{\text{wbmle}}$: The sources are regarded as deterministic but unknown,

A5$_{\text{wbmle}}$: The noise is spectrally white at each subband and the level of the noise spectral density at the j$^{\text{th}}$ subband, $\sigma_n^2(f_j)$ is unknown.

Then under the aforementioned assumptions, the ML estimate of the unknown arrival angles of the wideband sources is one that maximizes the following likelihood function

$$L(\boldsymbol{\Theta}) = \sum_{j=1}^{N_b} \text{trace}\left(\mathbf{P}_{\mathbf{A}(\boldsymbol{\Theta},f_j)}\widehat{\mathbf{R}}_{\mathbf{XX}}(f_j)\right). \tag{4-4}$$

Based on (4-4), the collection of narrowband sample covariance matrices, $\{\widehat{\mathbf{R}}_{\mathbf{XX}}(f_j),\ \text{for } j = 1, \dots, N_b\}$, may be regarded as sufficient statistic for the estimation problem at hand and the ML estimate of $\boldsymbol{\Theta}$ is obtained by solving the following optimization problem

$$\widehat{\boldsymbol{\Theta}} = \max_{\boldsymbol{\Theta}} \left\{ \sum_{j=1}^{N_b} \text{trace}\left(\mathbf{P}_{\mathbf{A}(\boldsymbol{\Theta},f_j)}\widehat{\mathbf{R}}_{\mathbf{XX}}(f_j)\right) \right\}.$$

Impracticalities of the WBMLE

The wideband version of MLE is computationally expensive and, depending on the system parameters, may be undesirable for imaging applications. This is due to the fact that range resolution must be sacrificed to improve the DOA estimation performance. The subbands must be made small enough to ensure that they are approximately narrowband, meaning that more range samples are needed to decrease the frequency bin size. For the 250 MHz UWB radar depth sounder, the length of the cross-track aperture is 3.36 meters which corresponds to a maximum propagation time across the array of approximately 11 ns. Suppose that the WBMLE was used for DOA estimation and bins were chosen such that the time-bandwidth product of the array was 10% for each subband. Then the number of time samples needed within each *subinterval*, N_b, must be at least 31. This corresponds to a degradation in range resolution by a factor of 31 suggesting that WBMLE may be an impractical solution to the wideband imaging problem. An investigation of the number of subintervals required to achieve good performance should be investigated in the future.

4.2.4 Peak Search

MLE, WBMLE and the WDOA algorithm obtain estimates of the vector of DOAs through minimization or maximization of some cost function. This allows these algorithms to capture refined estimates of the

peaks or valleys of their respective objective functions. The MUSIC estimate was previously [10] obtained by evaluating the pseudospectrum over a grid and finding the maximum value. This limits a MUSIC estimate to points on the grid and introduces a bias in the RMSE. MATLAB's optimization solvers, such as *fmincon* for example, are designed to search a function's domain for a local minimum. This behavior was leveraged to allow MUSIC to sample off the grid by using the MUSIC pseudospectrum as a cost function argument for the constrained optimization solver. The MUSIC pseudospectrum was evaluated over a grid to get an initial estimate of source locations and *fmincon* was used to refine the estimates.

4.2.5 Validation of Narrowband Techniques

Ziskind and Wax demonstrated the performance of MLE solved with the Alternating Projection algorithm in [6] where the authors compared the technique to the MUSIC algorithm. Because the ML solution of the DOA is obtained with MATLAB's constrained optimization function *fmincon* the results of Ziskind and Wax were first verified. This provided some reliable confidence that the experiments described below could reliably describe the performance of the narrowband techniques in wideband signal environments. Three results from [6] have been recreated and are presented below.

In the validation of the results of Ziskind and Wax, the WDOA and WBMLE techniques were applied in addition. The purpose of doing this was two-fold. First this offered some insight into the performance of the WDOA technique in narrowband imaging configurations and also provided a check for verifying that narrowband MLE and WBMLE were equivalent in narrowband signal environments. For the narrowband signal environment, both the widening factor of the WDOA method and the number of subbands for WBMLE are taken to be 1.

Narrowband Experiment 1

In the first experiment, three isotropic elements at half-wavelength spacing are assumed. The sensors spatially sample a field arising from two narrowband, equal power uncorrelated sources arriving from 0° and 20° respectively. The number of available snapshots is assumed to be 10. The RMS errors in degrees for each source that results from sweeping the SNR from 10 dB to 25 dB are shown in Figure 4-3 and Figure 4-4. In both cases, MLE (indicated with red markers that are completely overlapped by WBMLE in the narrowband case) outperforms both MUSIC and the WDOA algorithm over all the values of SNR tested. In the high SNR limit, MUSIC appears to converge to MLE but exhibits a slight performance degradation in RMS error of about 0.035°. The WDOA outperforms MUSIC for lower SNRs but between 17 and 19 dB, the RMS error of MUSIC falls below that of the WDOA so that in the high SNR limit, the WDOA exhibits a bias that is slightly higher than MUSIC. The bias of from the MLE's RMS error is about 0.16° in the high SNR limit.

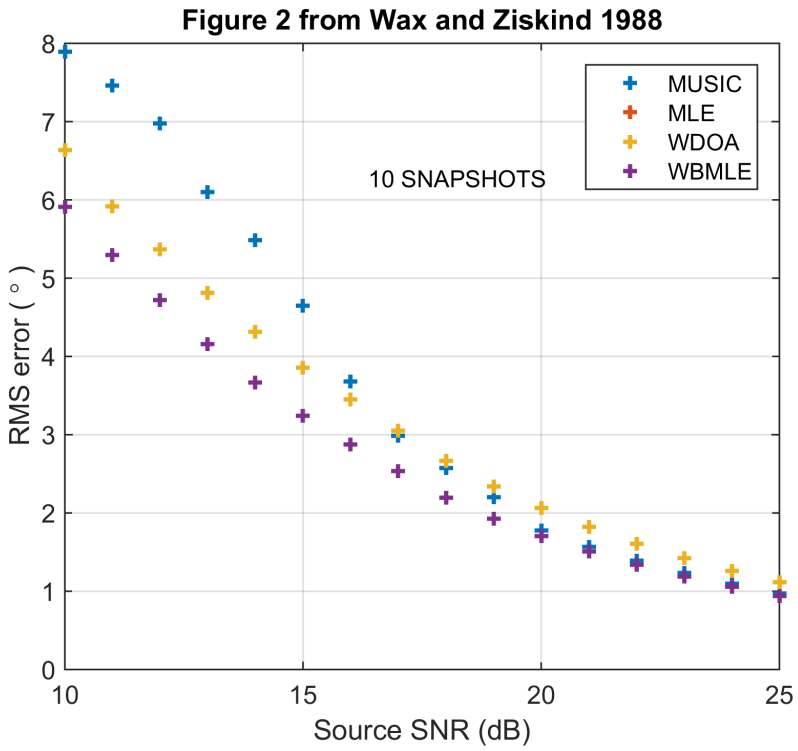

Figure 4-3 Narrowband Experiment 1: RMS error of 0° degree source

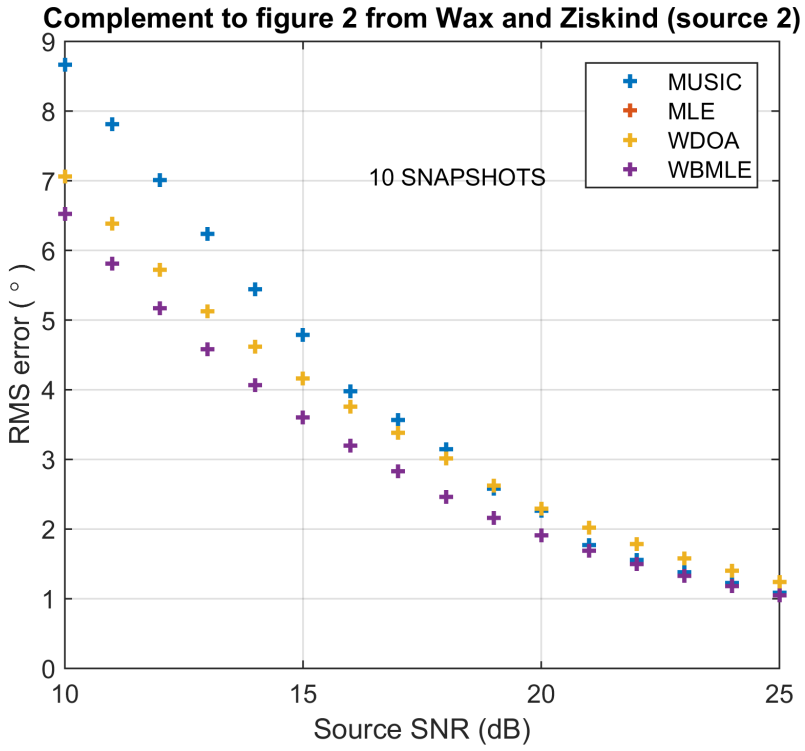

Figure 4-4 Narrowband Experiment 1: RMS error of 20° source

Narrowband Experiment 2

The setup of the second experiment is identical to the first except that the SNR is set to 20 dB and the number of available snapshots is swept from 10 to 1,000. The RMS error was estimated for both sources and were found to be quite similar. Only the RMS error of the 0° source is presented in Figure 4-5 below. Though the MLE (overlapped by the WBMLE) exhibits the smallest RMS error over each tested number of snapshots, the results are comparable and difference between the methods get smaller as the sample support grows.

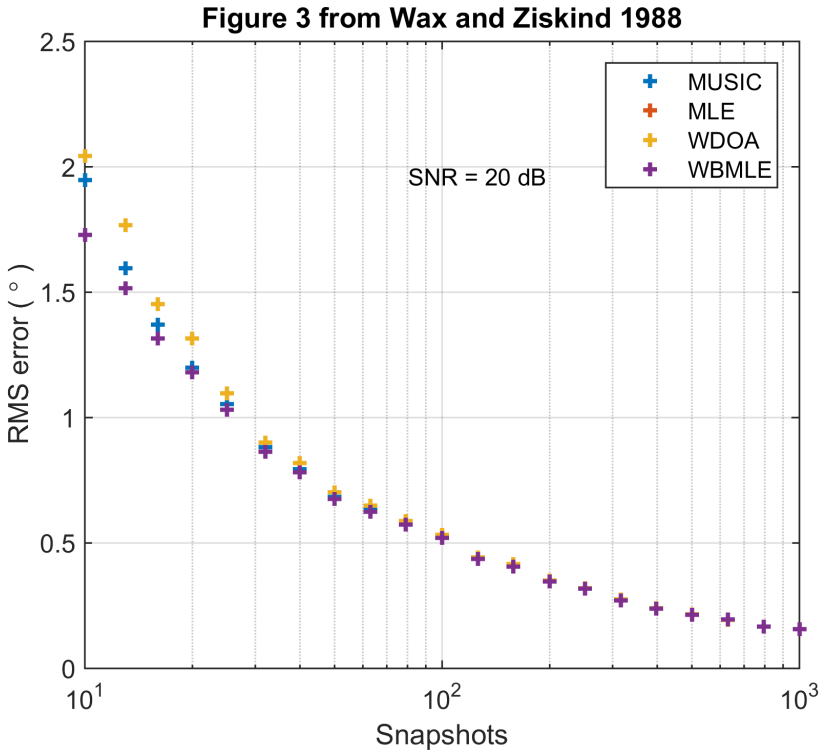

Figure 4-5 Narrowband Experiment 2: RMS error of 0° source

Narrowband Experiment 3

The third experiment tests the performance of the DOA estimators when two equal power (20 dB) narrowband sources impinge on the array from 0° and 5°. The number of snapshots is swept from 50 to 500. Since the beamwidth of the ideal array is 57°, resolution of two sources separated by 5° is much more challenging. The RMS error of the source at 0° is shown in Figure 4-6. The results for the 5° source are nearly identical and therefore are not included. Again the MLE results and WBMLE results are identical and both identically outperform MUSIC and the WDOA. When the number of snapshots is less than about

300, MUSIC shows lower RMS error than the WDOA but in the high snapshot limit, the WDOA outperforms MUSIC and more closely approximates MLE.

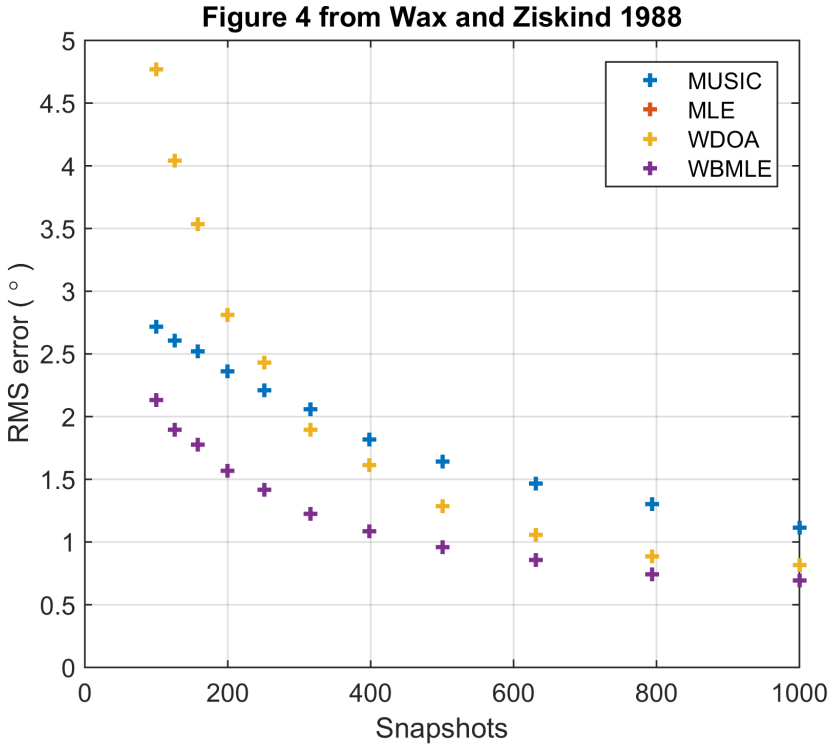

Figure 4-6 Narrowband Experiment 3: RMS error of 0° source

4.2.6 Simulation of Wideband Sources

The simulations described herein are all overly simplified imaging scenarios meant to study the left/right separation of basal echoes with sufficient signal-to-clutter ratio (SCR) as well as the DOA problem for targets off to the side. In what follows, results are presented from several Monte Carlo experiments used to study the performance of the DOA estimators for imaging with the 250 MHz version of the UWB radar depth sounder that operated from the Basler in 2013. The results presented arise from three distinct setups:

- *Wideband experiments 1A through 1C:* Simulations which compare the narrowband methods to the WDOA for estimating the arrival angle of a single wideband source,
- *Wideband experiments 2A through 2C:* Simulations which compare the performance of the WDOA to an optimal wideband estimator, the WBMLE, using a setup that models the sidelooking imaging case,
- *Wideband experiments 3A:* Simplified simulation that considers the use of MLE or MUSIC in left/right separation at nadir.

Wideband Experiment 1A

The first experiment demonstrates the problem that arises when the narrowband methods are used to estimate source arrival angles in wideband signal environments. Here a single high SNR, wideband source is assumed and the number of snapshots is set to 100. The direction of arrival is swept from 0° out to 45°. Since MATLAB's fmincon function uses a set of bounds to limit the search during minimization, the DOA solution was restricted to the interval $\left[-\frac{\pi}{2}, \frac{\pi}{2}\right]$. For $N_s = 1$, this implementation provides the global minimum of the single dimensional cost functions. Note that in the special case of $N_s = 1$, the likelihood function is equivalent to the spatial matched filter. The RMS errors of the MUSIC, MLE and WDOA estimates are presented in Figure 4-7. For source arrival angles exceeding 45°, the RMS errors of the MUSIC and MLE estimates become increasingly large (exceeding 80°) while the WDOA estimate remains small.

For small DOAs, MUSIC and MLE offer reasonable performance with errors less than a degree even when the DOA is 20°. This suggests that the narrowband techniques may be tolerable for small off-nadir incidence angles provided that the SCR is sufficiently large enough. If the surface clutter is on the order of the ice-bed SNR, then clutter from the surface (characterized by errors in excess of 60° depending on the geometry) are ineffectively modeled and may corrupt the bed echo signal. Once the source DOA exceeds 20°, the errors in the MUSIC and MLE estimates increase more rapidly. This is the time-bandwidth product exceeds one for 250 MHz sources. At 25°, a source spreads over two pixels meaning that a signal that impinges on channel 1 illuminates channel 8 one sample later. For a source from 50° off nadir, the registration error between channel 1 and channel 8 is two samples.

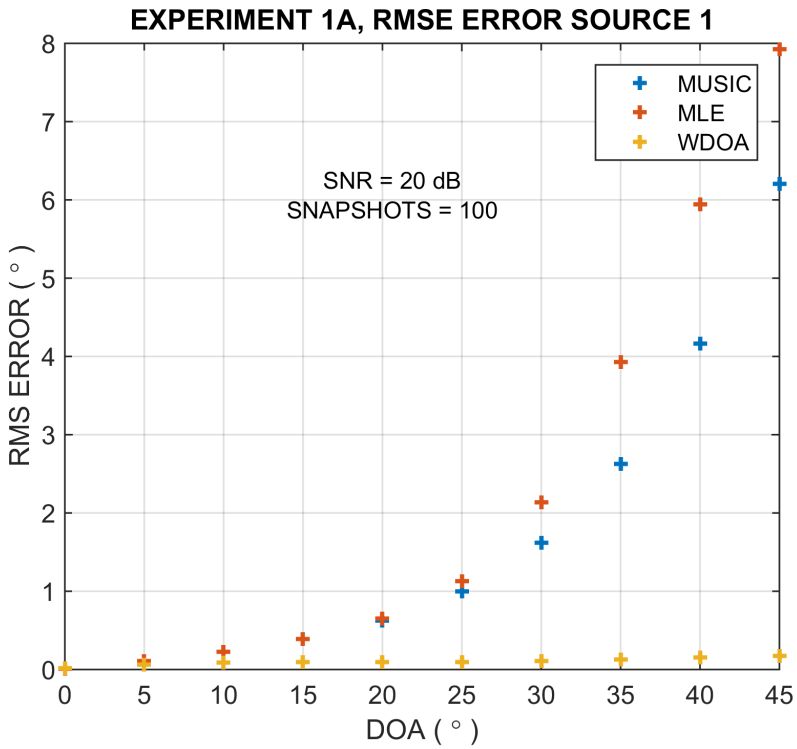

Figure 4-7 Wideband experiment 1A: RMSE of single wideband source with variable DOA

Wideband Experiment 1B

In experiment 1B, a single wideband source is assumed to be fixed at 25°. The source is characterized by a low per channel SNR of -5 dB (so that the combined SNR of the 8 element array is 3 dB). The number of snapshots is swept from 10 to 1,000. The RMS errors for the single wideband source DOA are presented in Figure 4-8. As might be expected, all three estimators are characterized by large errors when the number of snapshots available for estimating the necessary statistics is 10 with MUSIC showing the largest error in the low snapshot/low SNR scenario, followed by MLE and then the WDOA algorithm.

This experiment shows that increasing the number of snapshots improves the performance of all three methods. MUSIC and MLE become increasingly close to one another in the high snapshot limit but are still outperformed by the WDOA. Also of note is that in the region where the number of snapshots exceeds about 30, large numbers of snapshots appear to influence the performance of the narrowband methods as compared to the space-time WDOA. By approximately 25 snapshots, the WDOA error has already fallen below 1° and decays slowly to its final error value of 0.2°. MUSIC does not fall below the 1° error mark until it has about 300 snapshots and MLE the requirement is closer to 400.

Although the narrowband techniques eventually approach a tolerable error in the high snapshot limit, they are impractical since there are rarely so many snapshots available for averaging. In imaging we use

neighborhoods of pixels to obtain snapshots. For this project, the typical number of averages used to estimate the DCM was 33 but could be as low as 11. Features off to the side are often narrow in range and in these cases using fast time samples may not offer any benefit. This means that for targets off to the side, we are often more reliant on the Doppler dimension for obtaining snapshots. There is an inherent assumption of stationarity of targets along the track and we must assume the scene to be slowly evolving in this dimension. The DOA estimation could be improved in the future with the use a smarter algorithm that allowed statistical multilooks to be adaptive.

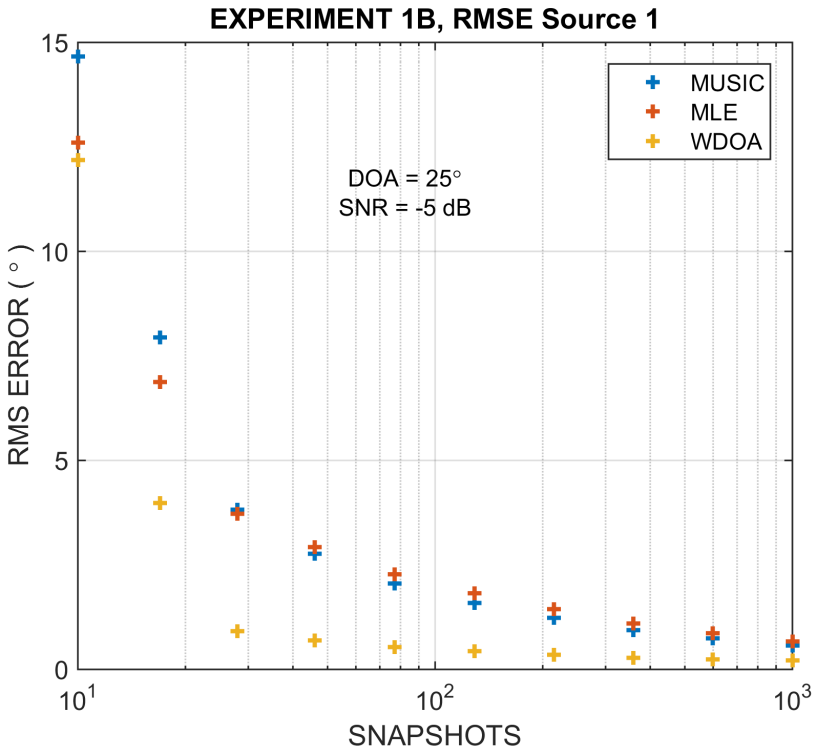

Figure 4-8 Wideband experiment 1B: RMSE of 25° source

Wideband Experiment 1C

The RMS error's dependence on the number of snapshots is also evaluated in the case of a high SNR wideband source at 25°. The number snapshots is again swept from 10 to 1,000 for the setup described above only now the source is assumed to be characterized by an SNR of 20 dB. The results of this experiment are presented in Figure 4-9. All methods show improved performance in the high SNR case and all similarly exhibit the same trend of the highest error being associated with the smallest number of snapshots and a monotonic decrease as the number of snapshots available increases. The error of the WDOA estimate starts at 0.3° and falls to a final value of 0.03° when 1,000 snapshots are used. The RMS error of

the MUSIC estimate starts at 2.8°, crosses the 1° error mark around 100 snapshots and falls to a final value of 0.32°. MLE is slightly higher than MUSIC, starting at 3° and falling to a final value of 0.37°.

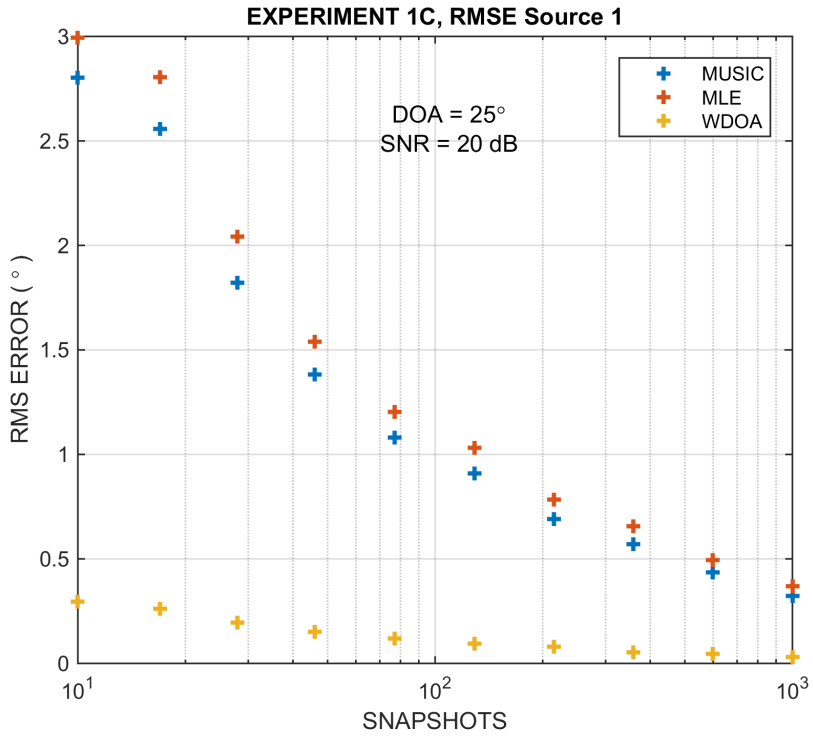

Figure 4-9 Wideband experiment 1C: RMS error of 25° source

Wideband Experiment 2A

Two uncorrelated sources are assumed within a possible field of view for the sidelooking imaging case. For this experiment, it is assumed that the transmit pattern provides sufficient isolation from echoes returning from the side of nadir opposite to the look direction. This scenario is illustrated in Figure 4-10. The arrival angles are 25° and 60° and number of snapshots is 30. Note that both DOAs lead to registration errors since the time-bandwidth products exceed 1. This simulation compares the WDOA and WBMLE estimates when WBMLE is limited to $N_b = 3$ so that it accesses the same number of fast-time samples as the WDOA (for a widening factor of 3). In this case, both algorithms degrade the range resolution by a factor of 3 and their computational complexities are considered to be similar. The SNR of the 25° source is swept from -5 dB to 35 dB while the SNR of the source at 60° is fixed to 10 dB.

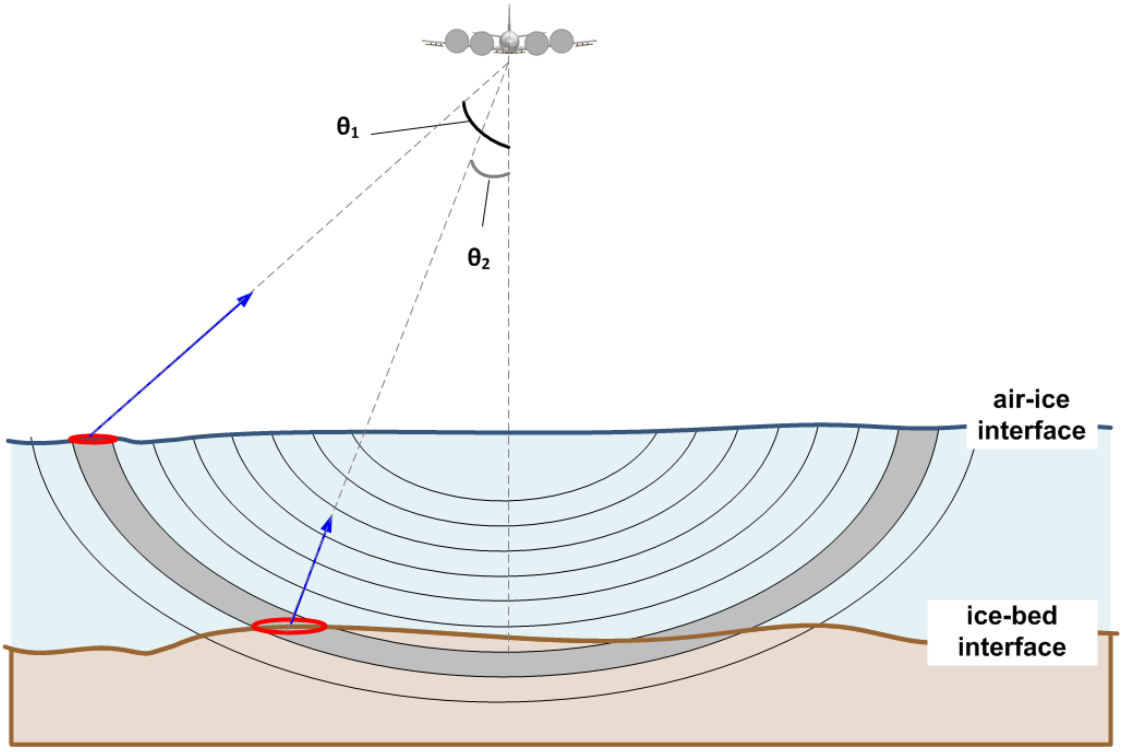

Figure 4-10 Imaging geometry assumed for experiments 2A through 2D

The RMS errors are estimated for each source and are presented in Figure 4-11 for the 25° source and in Figure 4-12 for the 60° source. In the case of the 25° source with variable SNR, the RMS errors for both techniques are highest at the lowest SNRs and both error curves decrease as the SNR increases. The change in performance evolves more slowly once the SNR exceeds about 10 dB and improvements in the accuracy of the 25° DOA estimates observed in the high SNR limit are small. When the error of the 60° source is taken into account, we see a degradation in performance of both algorithms once the SNR of source 1 exceeds the SNR of source 2. When the SNR of the first source exceeds 15 dB, the error of the WDOA estimate rises above 1° until it approaches a steady state value of 4° when the SNR exceeds 35 dB. The error of the WBMLE estimate for source 2 is lowest when source 1 is at -5 dB SNR, corresponding to an error of 1.3° and increases to a steady state error of 5° in the high SNR limit.

This experiment suggests that for this sidelooking configuration, the WDOA algorithm offers better performance than the WBMLE when both algorithms are only allowed to degrade or coarsen the range resolution by a factor of 3. This example also shows the complexity of the multisource DOA estimation problem and in particular the challenge that arises when one source is much larger than another. Suppose we could only tolerate errors less than 1°. Then accurate estimates of both sources could only be obtained with the WDOA when the SNR of the 25° took a value between approximately 3 and 15 dB.

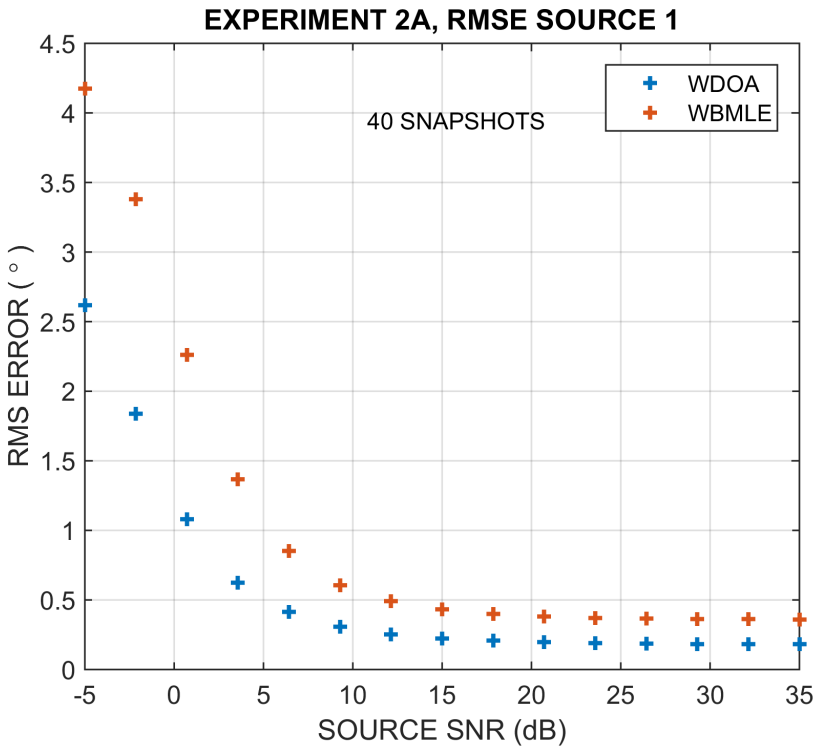

Figure 4-11 Wideband experiment 2A: RMS error of 25° source

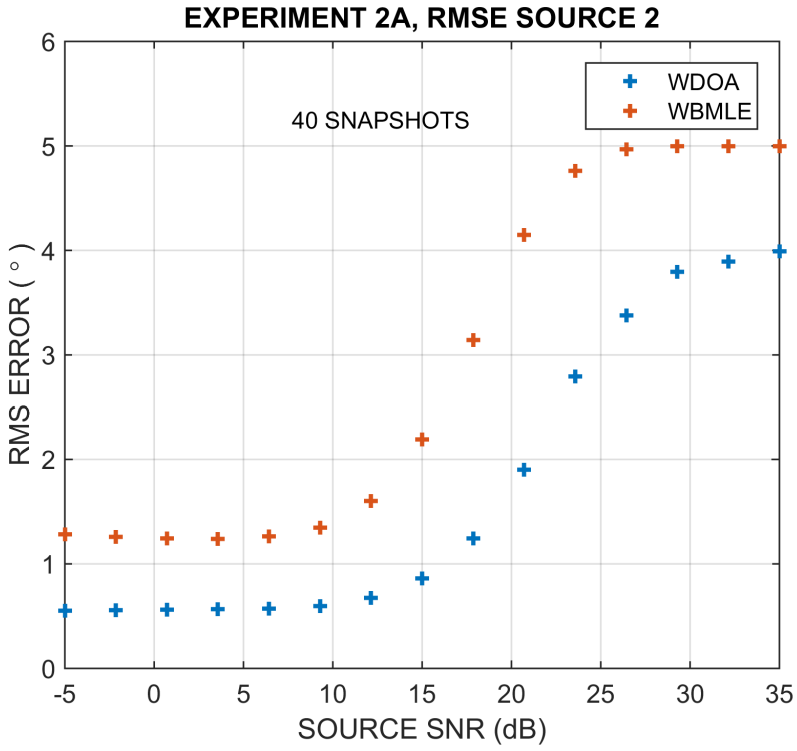

Figure 4-12 Wideband experiment 2A: RMS error for 60° source

Wideband Experiment 2B

The previous experiment showed that for the hypothetical sidelooking geometry in Figure 4-10, the WDOA outperforms WBMLE when the two algorithms operate with comparable computational complexity. In the experiments that follow, WBMLE is used as a benchmark for measuring the performance of the WDOA algorithm as a wideband DOA estimator. For these simulations, the number of subbands used to obtain the WBMLE results is $N_b = 31$ so that each frequency bin spans 3% of the 250 MHz system bandwidth and the time-bandwidth product of the array is less than 10%.

The WDOA is compared to the optimal WBMLE based on the RMS errors of the DOA estimates presented in Figure 4-13 and Figure 4-14. 40 temporal snapshots are assumed (as in the previous example). The error curves for the WDOA estimates are the same as in the previous example but the WBMLE result acts as a lower bound.

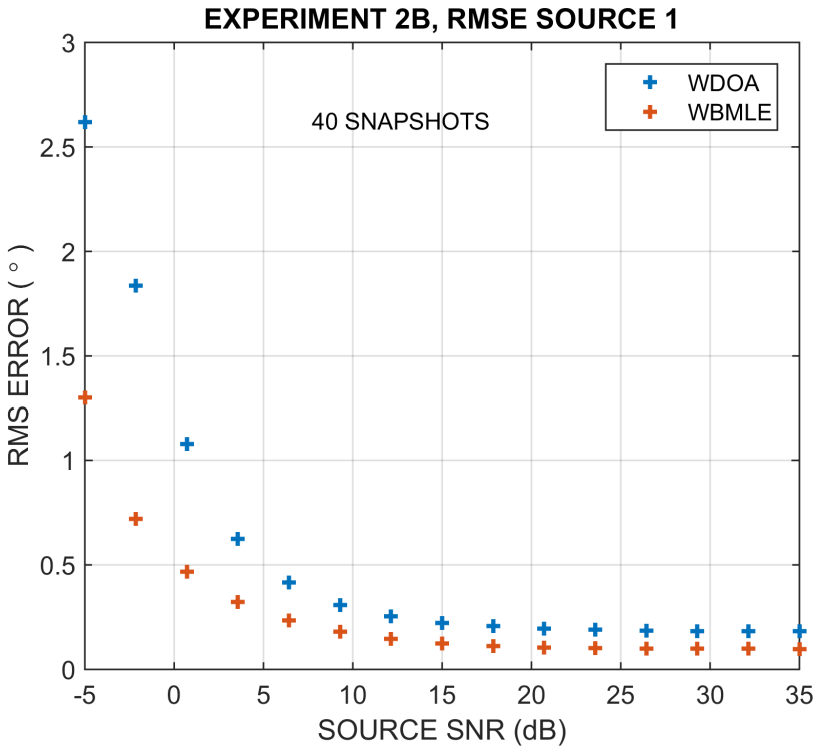

Figure 4-13 Wideband experiment 2B: RMSE of 25° source

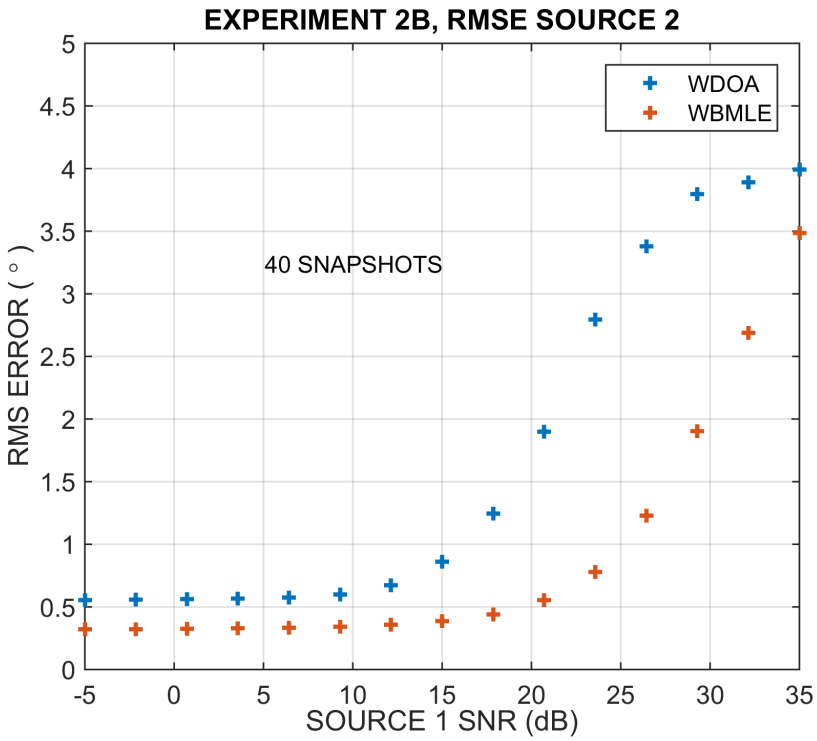

Figure 4-14 Wideband experiment 2B: RMSE of 60° source

Wideband Experiment 2C

This experiment considers the influence of number of available snapshots on the WDOA performance in a low SCR scenario. The SNR of the 60° source is fixed at 10 dB and the SNR of the 25° source is set to 5 dB. Taking the 25° source to be the target, the SCR is -5 dB. The number of snapshots is swept from 40 to 1,000. The outcomes from this experiment are shown in Figure 4-15 and Figure 4-16. The performance of both the WDOA and WBMLE improves as the snapshot support increases. At 40 snapshots, the WDOA exhibits less than 1° error for both the target and the clutter. Despite the presence of a competing source, the WDOA appears to perform well in this example in terms of recovering the arrival angle of the target.

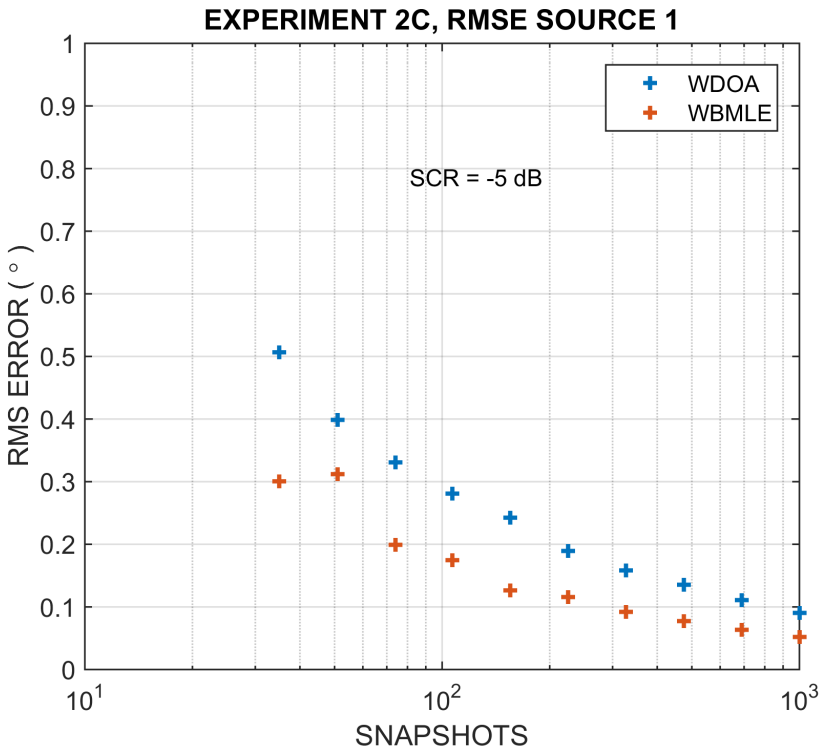

Figure 4-15 Wideband experiment 2C: RMSE of target at 25°

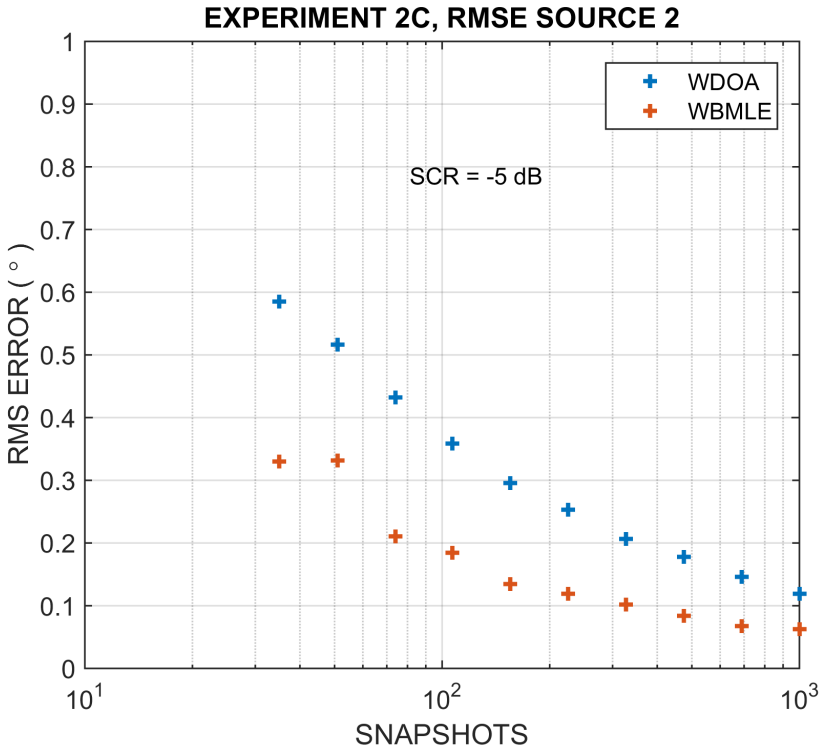

Figure 4-16 Wideband experiment 2C: RMSE of surface clutter at 60°

Wideband Experiment 2D

Now a case of high SCR is considered. The SNR of the 60° source is fixed at 10 dB and the SNR of the 25° source is set to 20 dB. Taking the 25° source to be the target, the SCR is -5 dB. The number of snapshots is swept from 40 to 1,000. The outcomes from this experiment are shown in Figure 4-17 and Figure 4-18. The performance of both the WDOA and WBMLE improves as the snapshot support increases. At 40 snapshots, the WDOA exhibits less than 1° error for both the target and the clutter. The WDOA estimates the target within 0.2° over the envelope of tested snapshot values and performs better for the 25° than in the -5 dB SCR case. Larger errors are observed for the 60° clutter source with both WDOA and WBMLE. The largest error for the WDOA is 1.67° and is associated with the lowest number of snapshots. This error is tolerable because it doesn't push the solution into the field of view associated with the target. After array processing, targets outside the field of view are thrown away in surface extraction. Thus as long as the errors do not push the surface clutter into the range of DOAs associated with backscatter from the ice-bed, they can be considered tolerable.

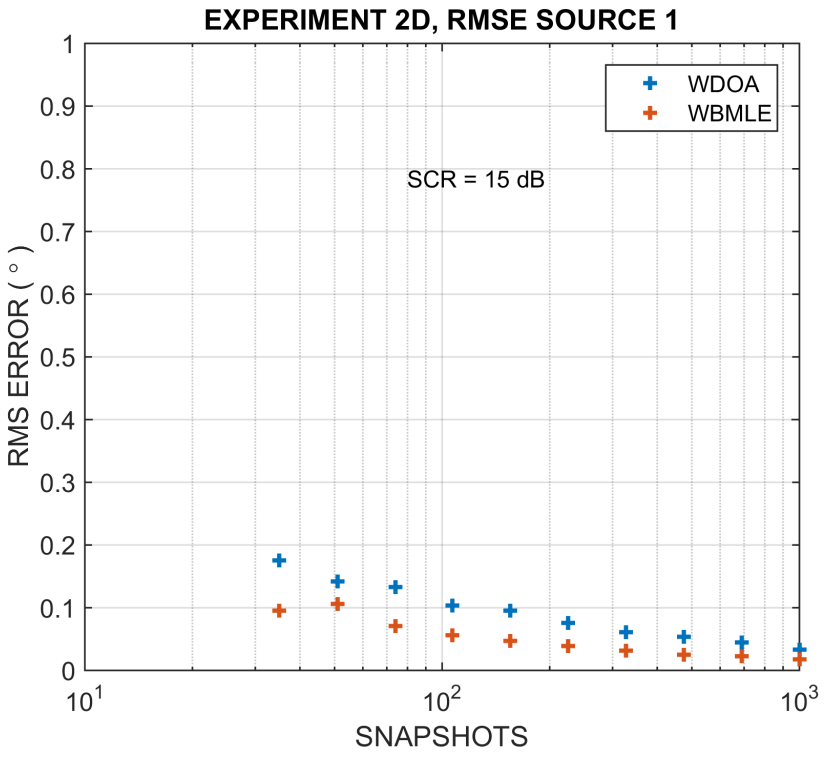

Figure 4-17 Wideband experiment 2D: RMSE of 25° target

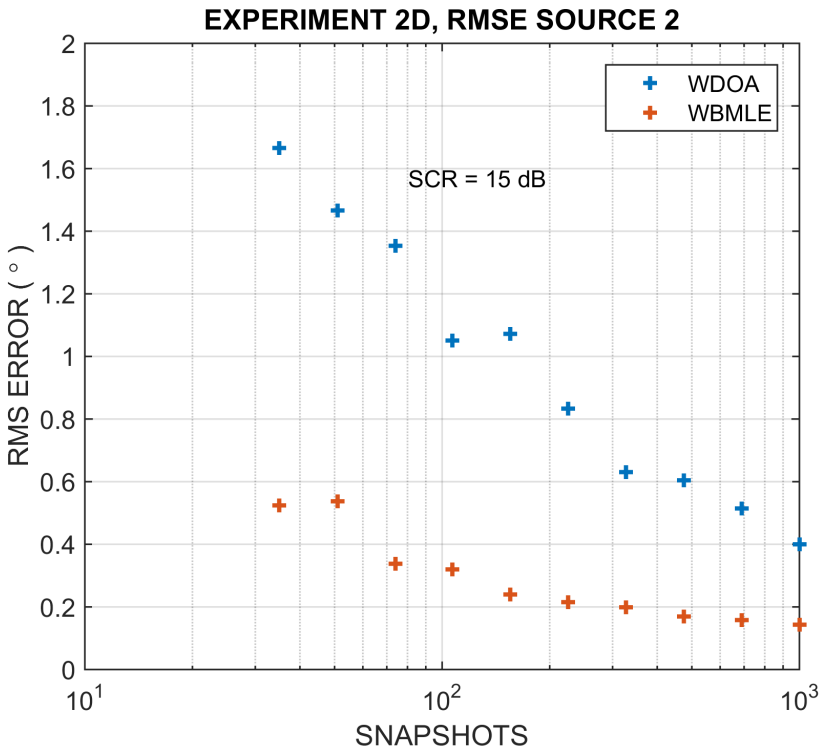

Figure 4-18 Wideband experiment 2D: RMSE of clutter at 60°

Wideband Experiment 3A

The last experiment considers sources that are uncorrelated, have equal power and whose DOAs are ±8°. The setup is meant to serve as an overly simplified model of the left/right separation problem for echoes near the edges of the swath when the beam is steered towards nadir on transmit, as illustrated in transmit and before the registration error problem arises when the arrival angles exceed 20°. The clutter from the air-ice interface is neglected since the near nadir basal returns generally dominate in the Basler datasets. The narrowband techniques along with the WDOA are used to estimate the DOAs as the SNRs are swept from -5 dB to 35 dB.

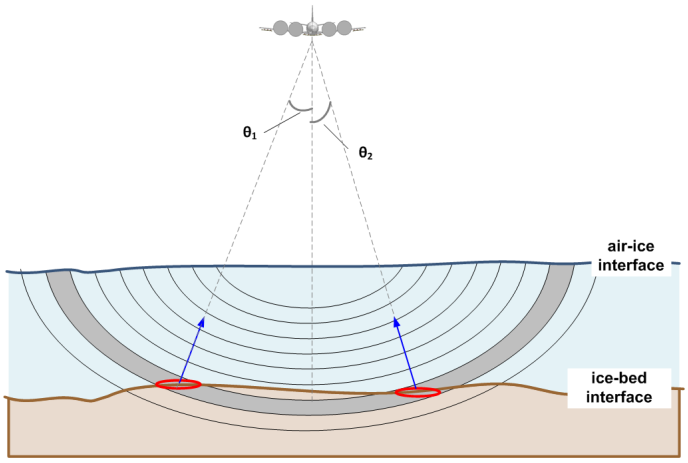

Figure 4-19 Setup for wideband experiment 3A

The number of snapshots is set to 30. The RMS errors of the two sources are similar so only results from the first source are shown. The WDOA outperforms the narrowband techniques over the range of tested SNRs. MLE exhibits slightly better performance over the MUSIC algorithm. The result suggests that in this simple example of two equal power left/right sources, the narrowband methods may be sufficient for DOA estimation provided that the clutter from the surface is negligible. If the clutter is not negligible, it has the potential of corrupting the ice-bed return which would ultimately translate into errors in the ice-bed elevation measurements obtained after array processing.

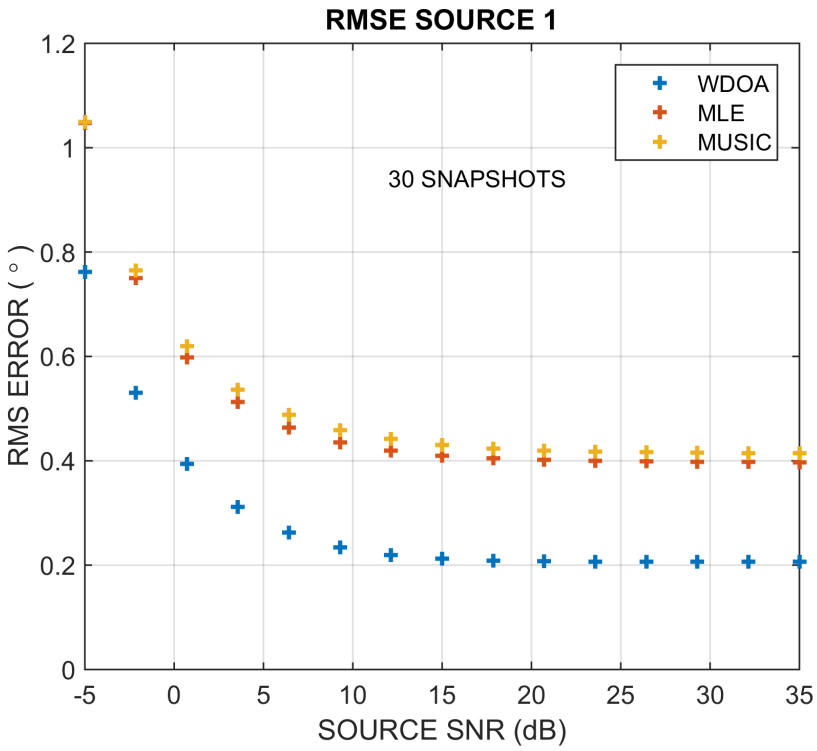

Figure 4-20 Wideband experiment 3A: RMSE of -8° source

4.3 Chapter Summary

This chapter summarized the development of a MATLAB based simulator used to carry out Monte Carlo experiments for studying DOA estimation in wideband signal environments assuming simplified scattering scenarios. The RMS error of a DOA estimate was used as the metric for evaluating an estimator's performance. The implementation of the narrowband methods used in these experiments was validated against results presented by Ziskind and Wax's Maximum Likelihood Estimator in [6] and in doing so the WDOA was adapted for the narrowband case. These results showed MLE to be optimal in narrowband signal environments, outperforming MUSIC and WDOA. The poor performance of the narrowband methods was demonstrated by sweeping the DOA from 0 to 45° to illustrate the changes in performance demonstrated by MUSIC and MLE when the time-bandwidth product of the imaging geometry exceeds 1. It was shown that the performance of the narrowband methods in estimating a wideband source could be improved when the number of data tends to infinity. An optimal wideband DOA estimator (WBMLE) was described and used as a benchmark for evaluating the performance of the WDOA method in a sidelooking setup. Finally a simplified geometry was postulated to consider the possibility of using the narrowband methods for imaging with the nadir beam.

Chapter 5

Results

The merit of the WDOA algorithm as an arrival angle estimator in ice sheet 3D tomography has been studied experimentally using wide swath, multibeam data collected by the UWB radar depth sounder from a Basler BT-67 aircraft during the 2013 Antarctic field season. Maps of the basal topography of Kamb Ice Stream are used to examine errors at crossing points. The results presented in this chapter demonstrate both the WDOA algorithm as well as the use of multiple beams to image large swaths.

5.1 Kamb Grounding Line

During the 2013 Antarctic mission, a dense grid was flown over the grounding line of the Kamb Ice Stream (or Ice Stream C) at high altitude and the UWB radar depth sounder/imager was run in the multibeam transmit scheme described in Chapter 2. Kamb Ice Stream is an area of interest to scientist because it was once responsible for discharging ice into the drainage basin of the Ross Sea but deactivated approximately 150 years ago. The termination of Kamb has been attributed to a thick layer of accretionary ice formed by the freeze on of subglacial water over thousands of years [21]. The stoppage of Kamb has served to counteract sea level rise by supporting local thickening of the ice in this part of West Antarctica. There is speculation about the possible reactivation of Kamb and understanding the basal processes that decelerated it will help model and predict the flow of adjacent ice streams that also drain into the Ross Sea.

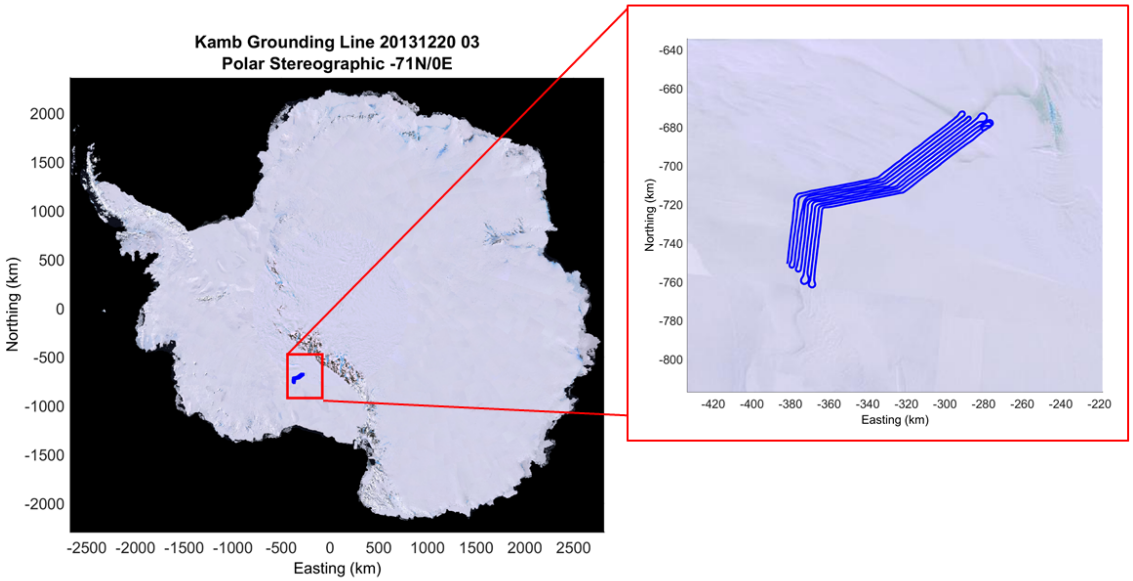

Figure 5-1 Kamb Grounding Line grid from 2013 mission in Antarctica

The flight lines for the Kamb grid are shown in Figure 5-1 Kamb Grounding Line grid from 2013 mission in Antarctica below. The data set contains 37 frames of data that break down into three sets of nine parallel tracks spaced approximately 1.5 km apart. This is slightly less than the multibeam footprint so little to no overlap is expected at the edges of any two swaths from adjacent tracks. The nominal ice thickness in this data set was observed to be in the neighborhood of approximately 570 meters.

5.2 Multibeam Processing

The Maximum Likelihood Estimator was chosen as the direction of arrival estimator for imaging with echoes from the nadir beam. The primary motivation for using MLE near nadir was to speed up processing of the multibeam data since MLE is computationally less burdensome than the WDOA. The rationale behind this choice was that in cases where the basal scattering dominated the pixels containing bed echoes, and near nadir where targets are primarily registered across the channels, MLE was considered adequate for separating left and right sides. For MLE processing, the number of sources is set to 2, MATLAB's fmincon is restricted to a search of the arrival angles within ±15° of nadir and the SNR is estimated using the pseudoinverse.

For the sidelooking beams, the WDOA was used to estimate the DOA. Again the number of sources was taken to be 2 and scattering was anticipated from the surface and ice bottom on the same side of nadir

as the look angle. The search was restricted to a range of DOA's as described in Chapter 3. The estimated DOAs associated with the surface are removed with an arrival angle threshold and discarded. From the remaining DOAs, those falling within the half power beamwidth are preserved for inversion. The SNR is estimated by registering to each DOA and applying the pseudo inverse to suppress clutter from the surface.

5.3 Tomographic Basal Maps

The ice-bed interface has been imaged for four parallel frames from the grounding line of the Kamb Ice Stream. The four frames were chosen because they each intersected with low-altitude crossing lines, meaning that depth sounder profiles were available for cross-over analysis. Both gridded ice-bed elevation maps along with backscatter images are presented here for each individual beam. A merged result for each frame is presented showing topography and backscatter results for all three beams simultaneously. These results are just laid on top of each other so there is not interpolation at the edges of the swaths where the beams come together. Holes that appear in the middle of the swaths are areas where the sidelooking beams do not overlap with the nadir beam.

5.3.1 Frame 008

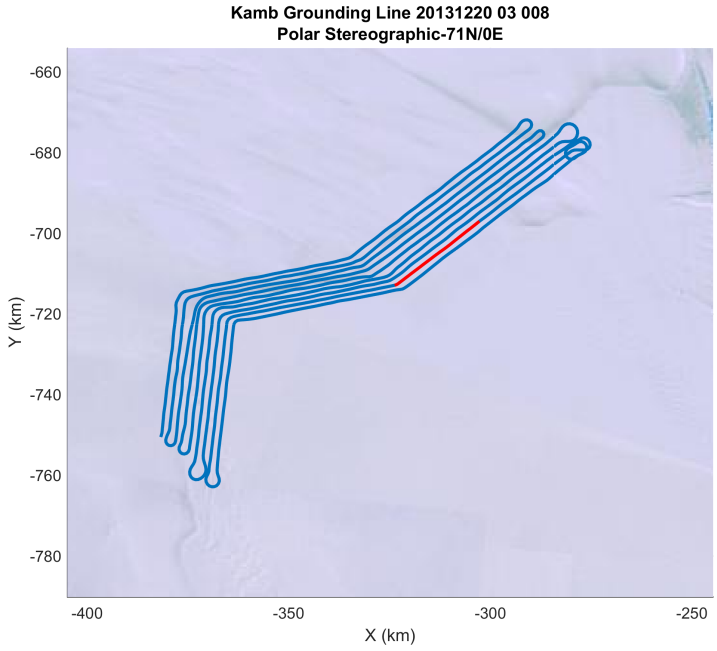

Figure 5-2 Geolocated frame 20131220_03_008

Left Beam

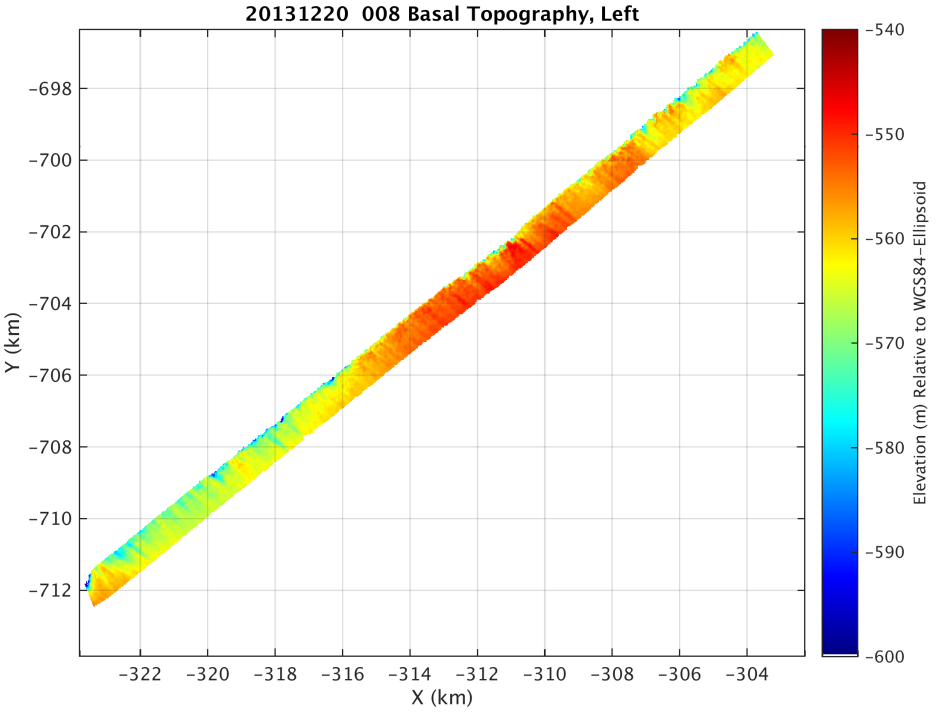
20131220 008 Basal Topography, Left
Y (km)
X (km)
Elevation (m) Relative to WGS84–Ellipsoid
-698
-700
-702
-704
-706
-708
-710
-712
-322
-320
-318
-316
-314
-312
-310
-308
-306
-304
-540
-550
-560
-570
-580
-590
-600

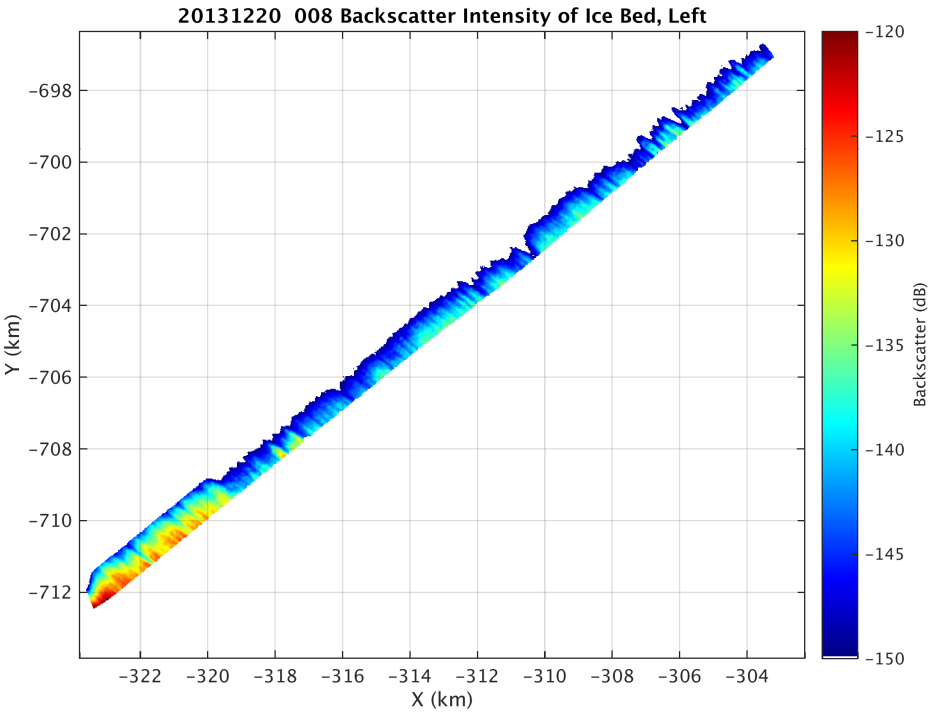
20131220 008 Backscatter Intensity of Ice Bed, Left
Y (km)
X (km)
Backscatter (dB)
-698
-700
-702
-704
-706
-708
-710
-712
-322
-320
-318
-316
-314
-312
-310
-308
-306
-304
-120
-125
-130
-135
-140
-145
-150

Nadir Beam

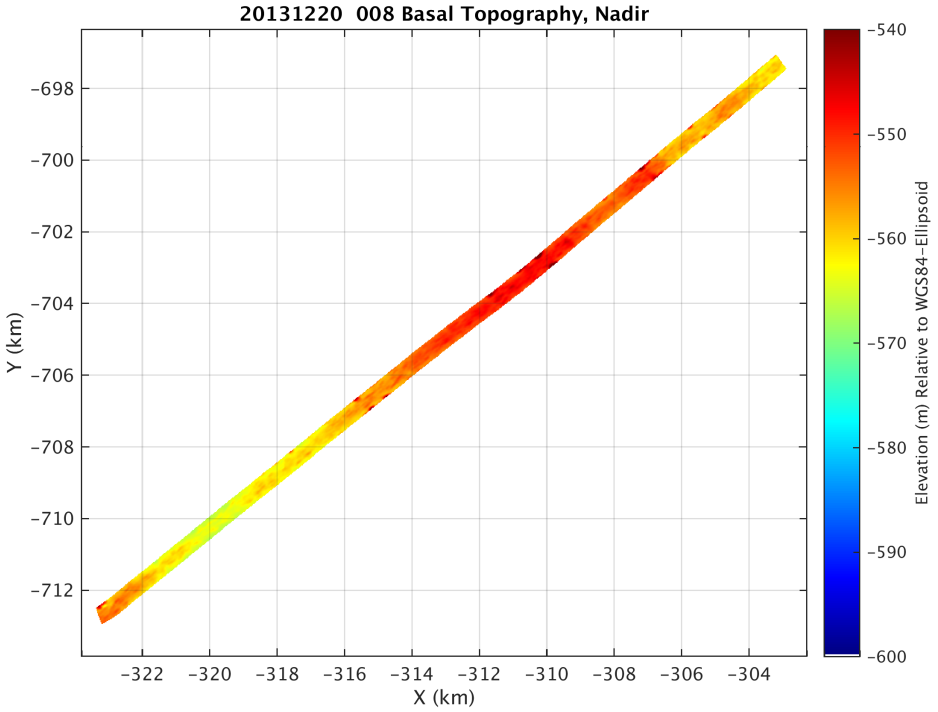
20131220 008 Basal Topography, Nadir
Y (km)
X (km)
Elevation (m) Relative to WGS84-Ellipsoid
-698
-700
-702
-704
-706
-708
-710
-712
-322
-320
-318
-316
-314
-312
-310
-308
-306
-304
-540
-550
-560
-570
-580
-590
-600

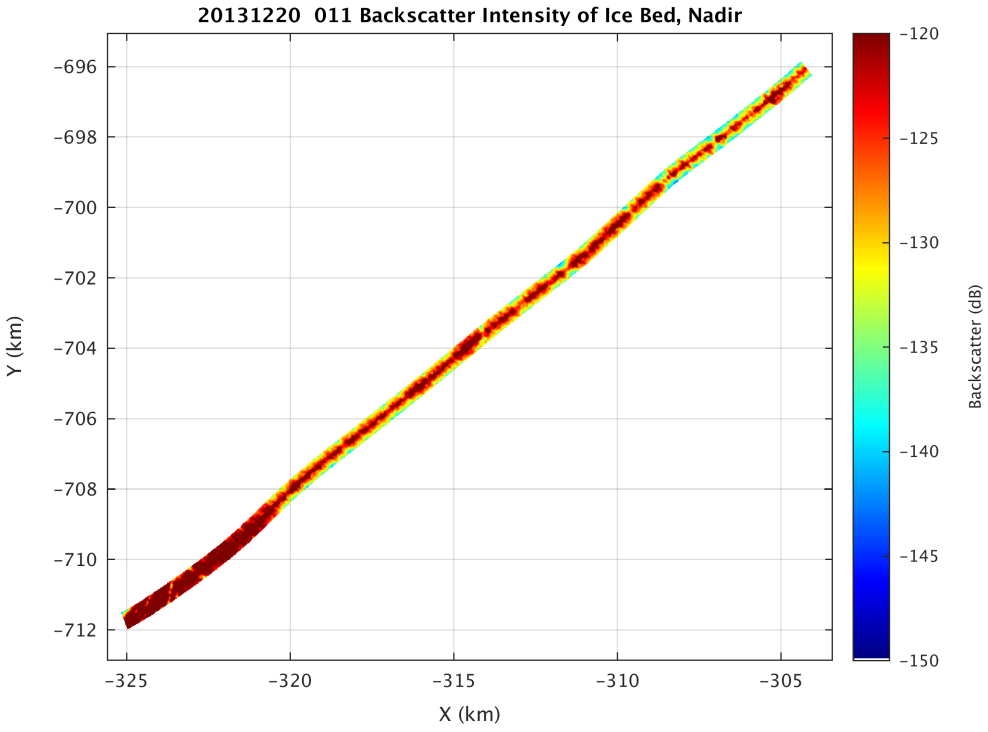
20131220 011 Backscatter Intensity of Ice Bed, Nadir
Y (km)
X (km)
Backscatter (dB)
-696
-698
-700
-702
-704
-706
-708
-710
-712
-325
-320
-315
-310
-305
-120
-125
-130
-135
-140
-145
-150

Right Beam

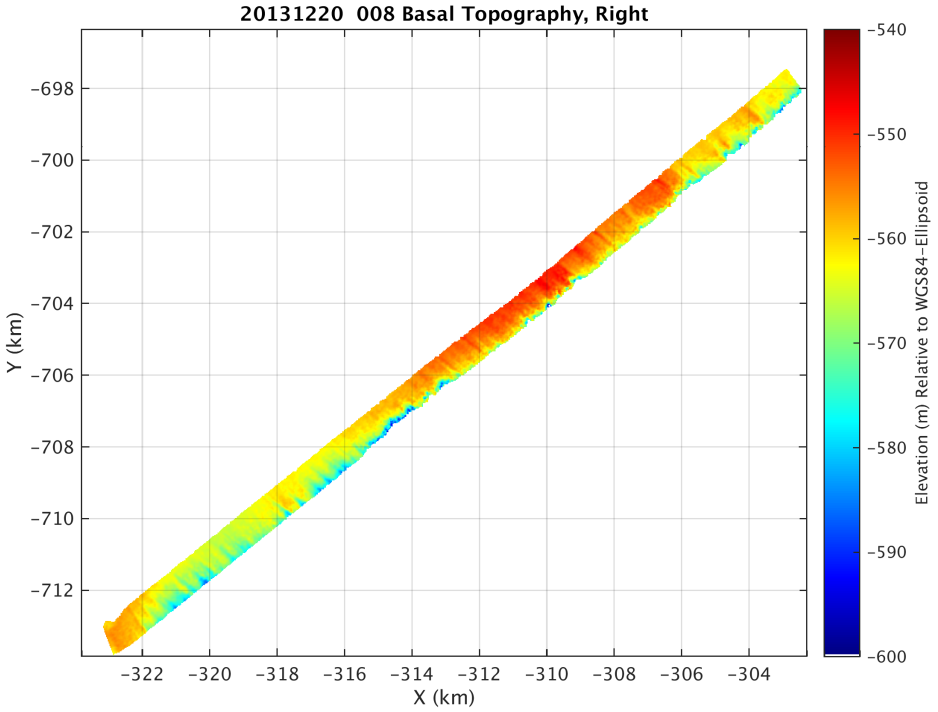
20131220 008 Basal Topography, Right
Y (km)
X (km)
Elevation (m) Relative to WGS84–Ellipsoid
-698
-700
-702
-704
-706
-708
-710
-712
-322
-320
-318
-316
-314
-312
-310
-308
-306
-304
-540
-550
-560
-570
-580
-590
-600

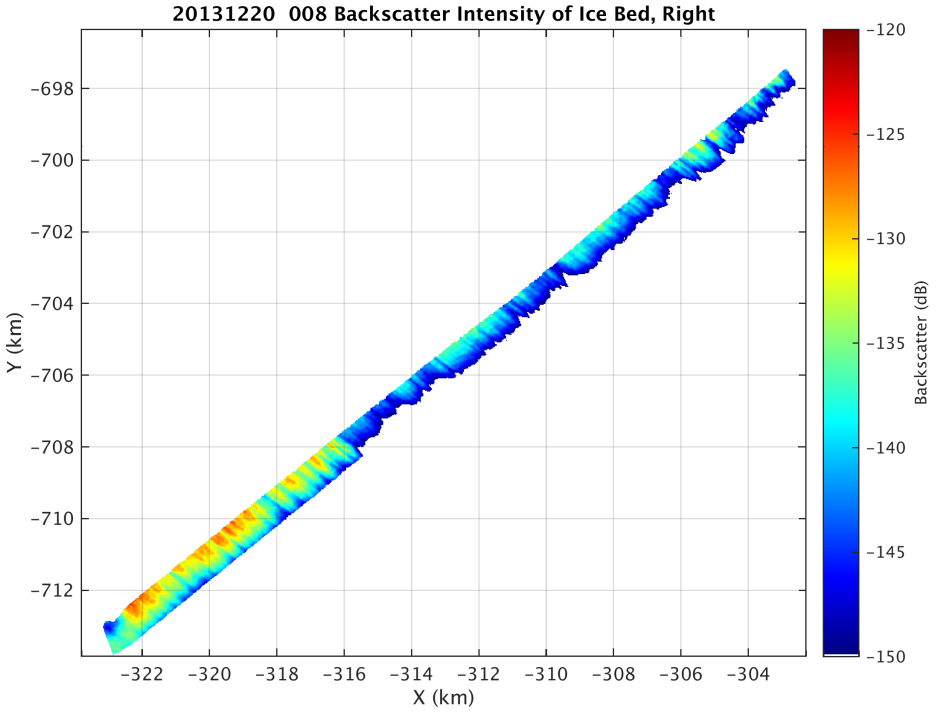
20131220 008 Backscatter Intensity of Ice Bed, Right
Y (km)
X (km)
Backscatter (dB)
-698
-700
-702
-704
-706
-708
-710
-712
-322
-320
-318
-316
-314
-312
-310
-308
-306
-304
-120
-125
-130
-135
-140
-145
-150

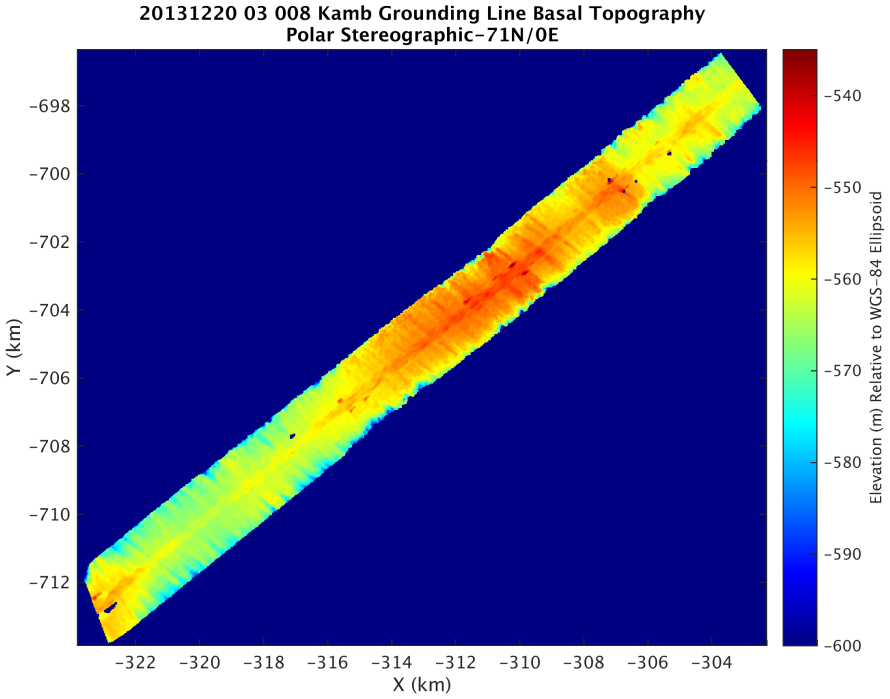

Figure 5-3 Merged DEM 20131220_03_008

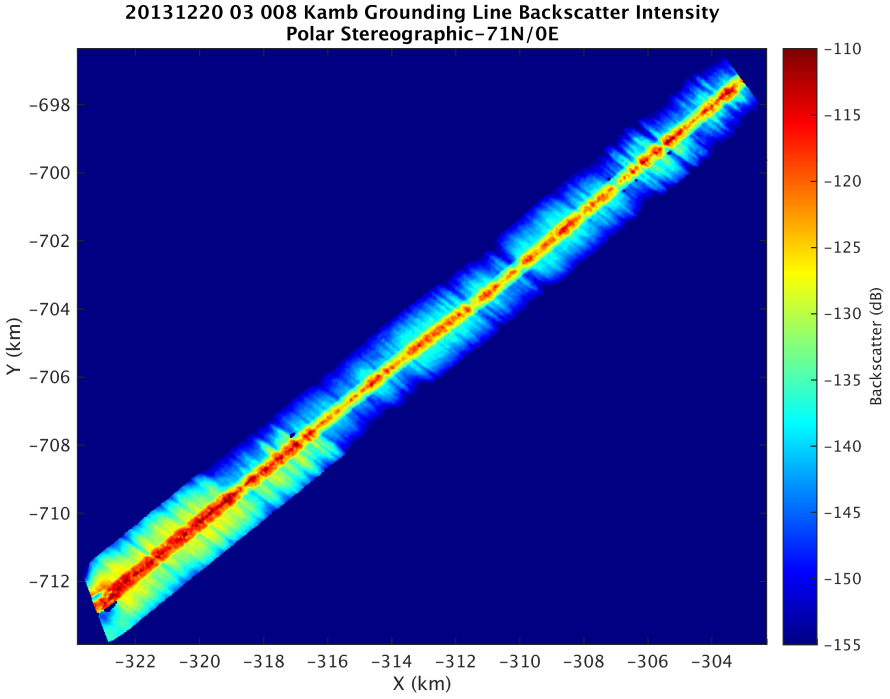

Figure 5-4 Merged backscatter maps 20131220_03_008

5.3.2 Frame 011

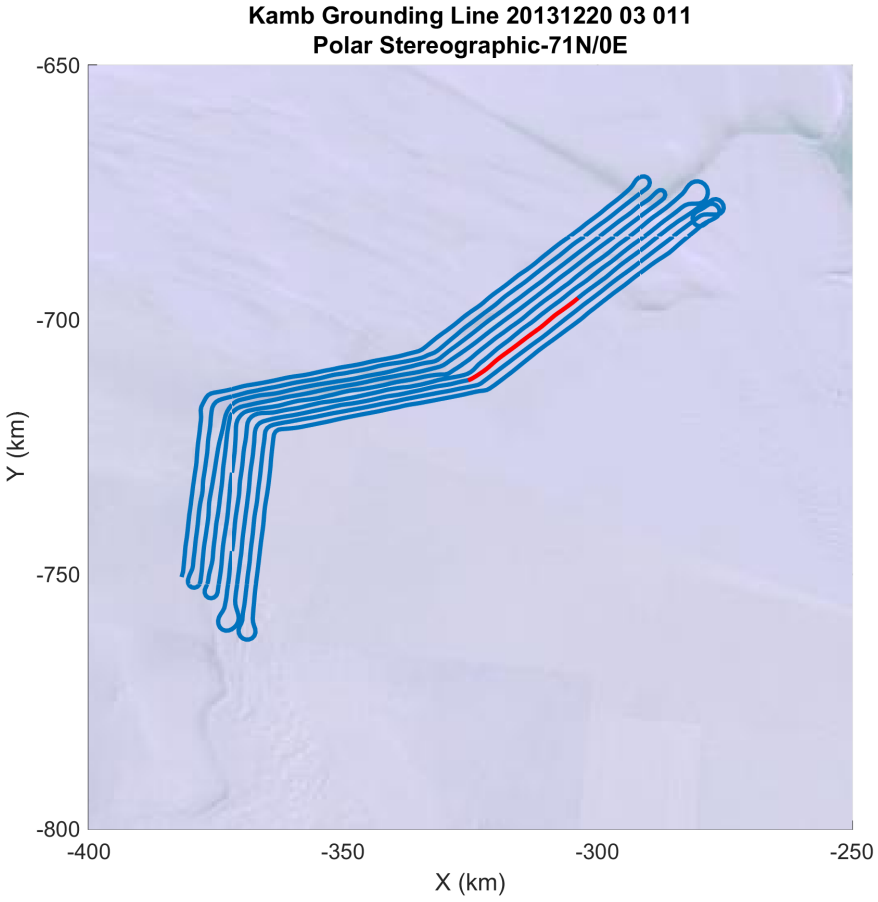

Left Beam

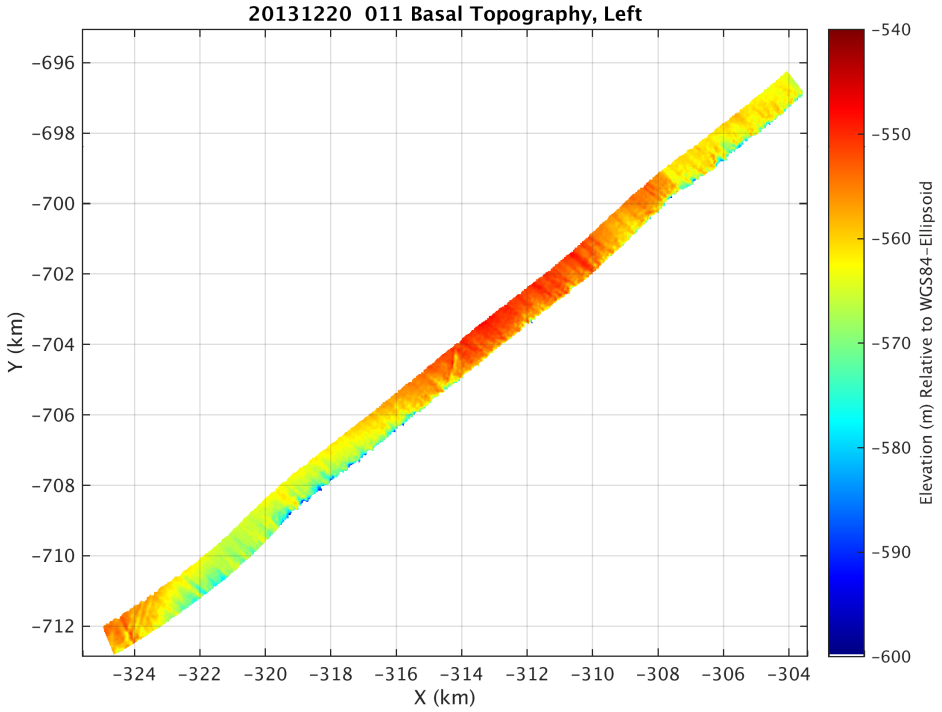
20131220 011 Basal Topography, Left
Y (km)
X (km)
Elevation (m) Relative to WGS84–Ellipsoid
-696
-698
-700
-702
-704
-706
-708
-710
-712
-324
-322
-320
-318
-316
-314
-312
-310
-308
-306
-304
-540
-550
-560
-570
-580
-590
-600

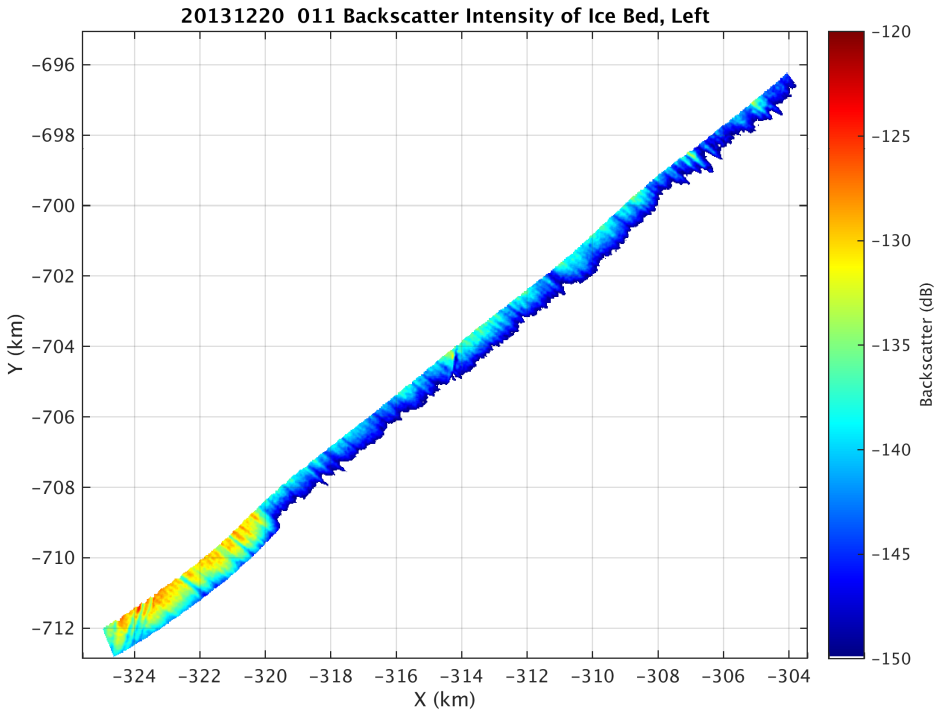
20131220 011 Backscatter Intensity of Ice Bed, Left
Y (km)
X (km)
Backscatter (dB)
-696
-698
-700
-702
-704
-706
-708
-710
-712
-324
-322
-320
-318
-316
-314
-312
-310
-308
-306
-304
-120
-125
-130
-135
-140
-145
-150

Nadir

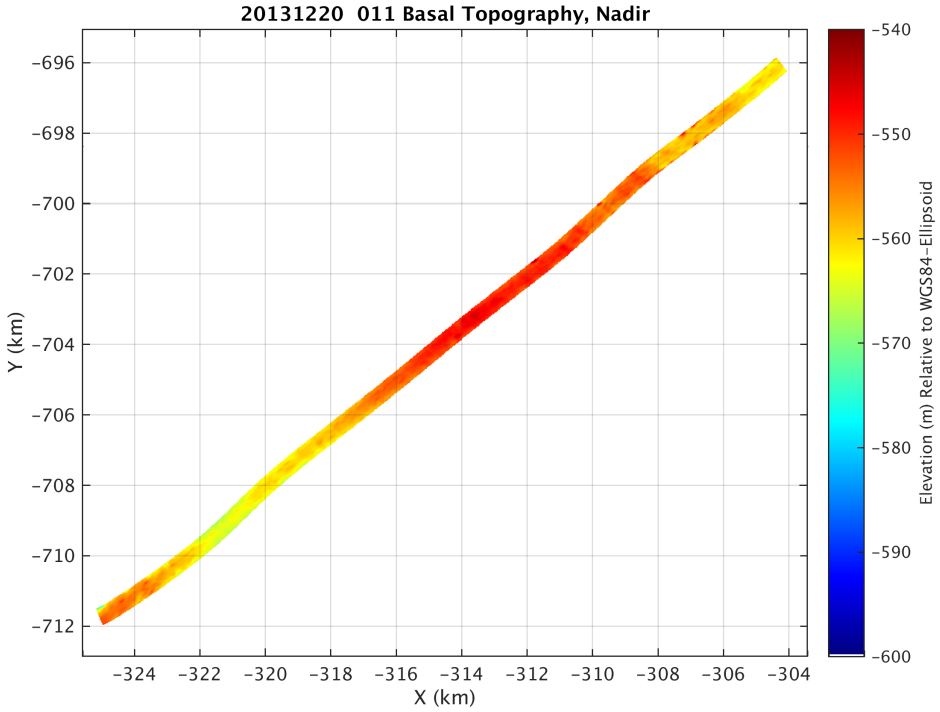
20131220 011 Basal Topography, Nadir
Y (km)
X (km)
Elevation (m) Relative to WGS84–Ellipsoid
-696
-698
-700
-702
-704
-706
-708
-710
-712
-324
-322
-320
-318
-316
-314
-312
-310
-308
-306
-304
-540
-550
-560
-570
-580
-590
-600

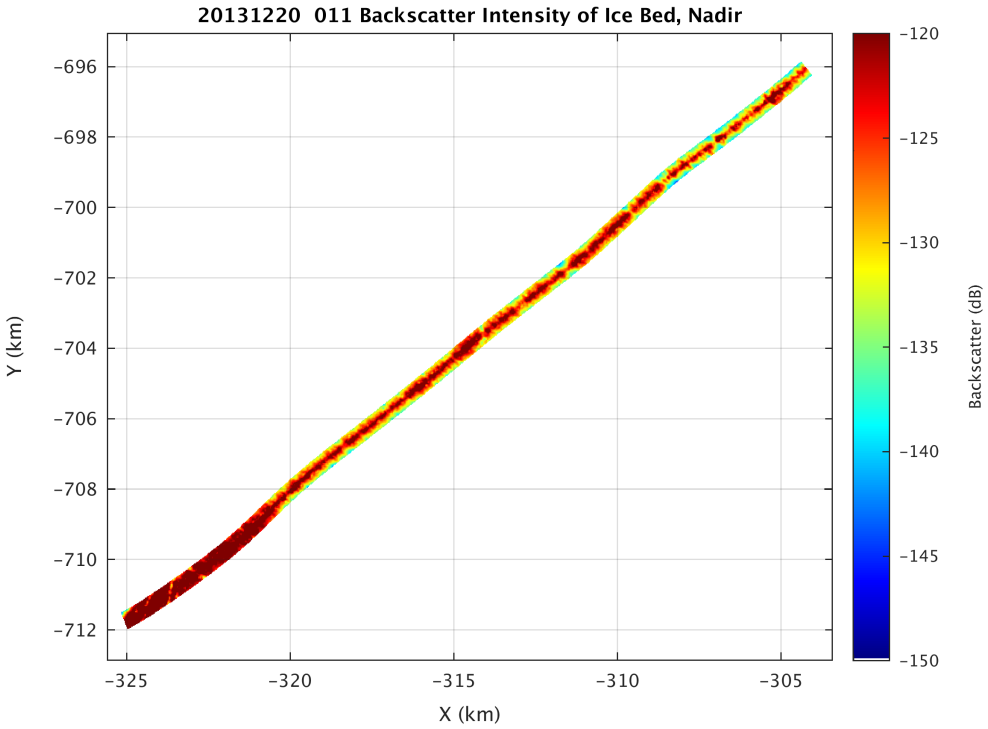
20131220 011 Backscatter Intensity of Ice Bed, Nadir
Y (km)
X (km)
Backscatter (dB)
-696
-698
-700
-702
-704
-706
-708
-710
-712
-325
-320
-315
-310
-305
-120
-125
-130
-135
-140
-145
-150

Right

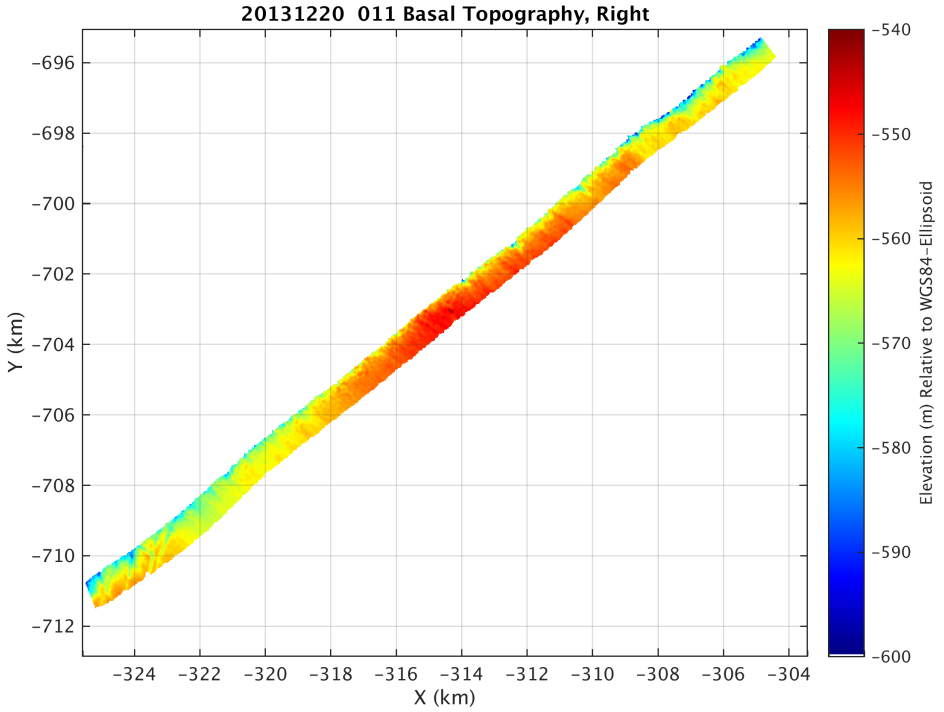
20131220 011 Basal Topography, Right
Y (km)
X (km)
Elevation (m) Relative to WGS84–Ellipsoid
-696
-698
-700
-702
-704
-706
-708
-710
-712
-324
-322
-320
-318
-316
-314
-312
-310
-308
-306
-304
-540
-550
-560
-570
-580
-590
-600

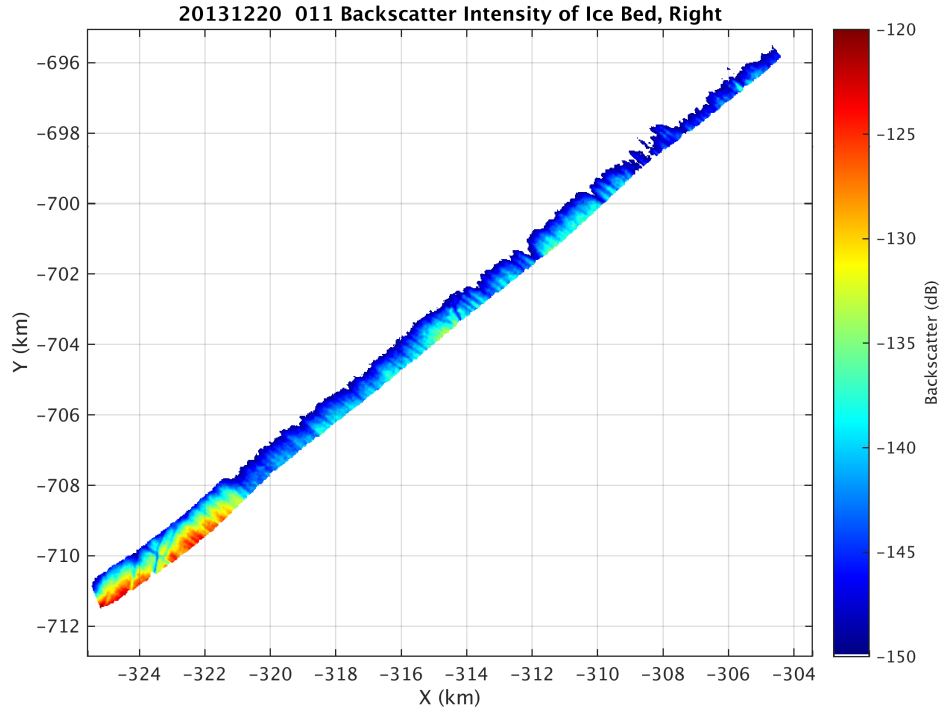
20131220 011 Backscatter Intensity of Ice Bed, Right
Y (km)
X (km)
Backscatter (dB)
-696
-698
-700
-702
-704
-706
-708
-710
-712
-324
-322
-320
-318
-316
-314
-312
-310
-308
-306
-304
-120
-125
-130
-135
-140
-145
-150

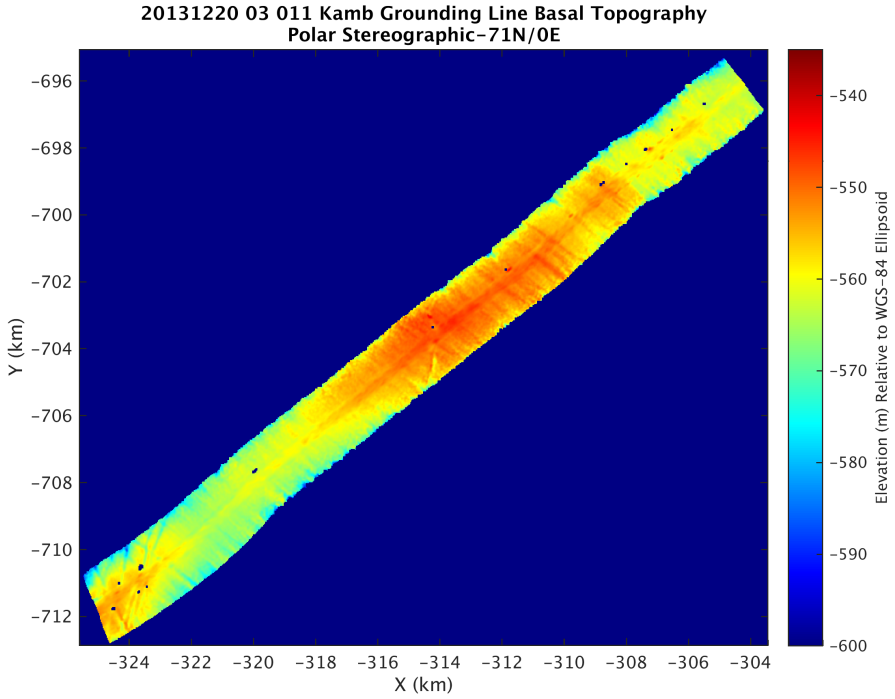

Figure 5-5 Merged DEM 20131220_03_011

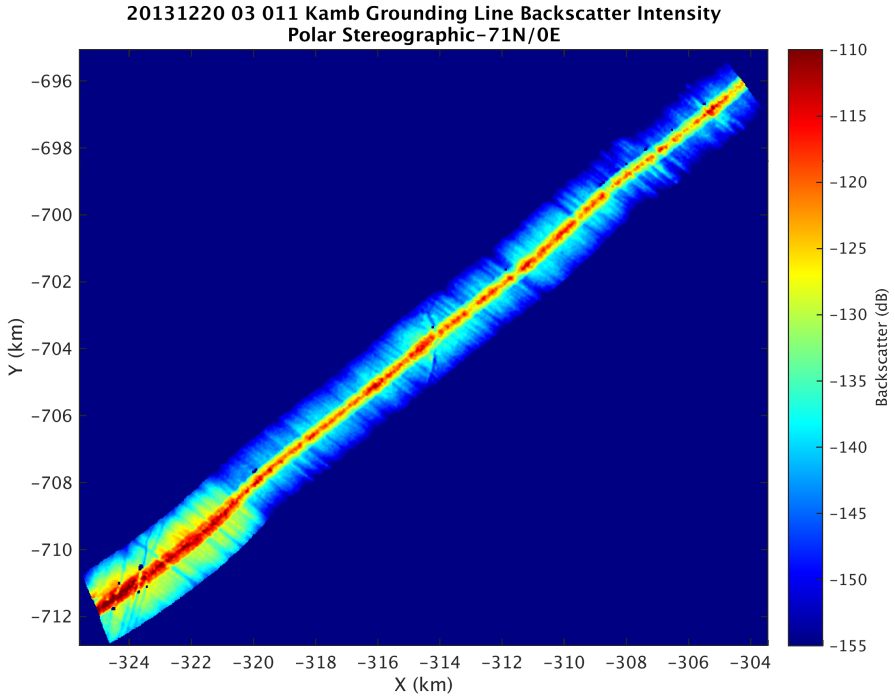

Figure 5-6 Merged backscatter map 20131220_03_011

5.3.3 Frame 016

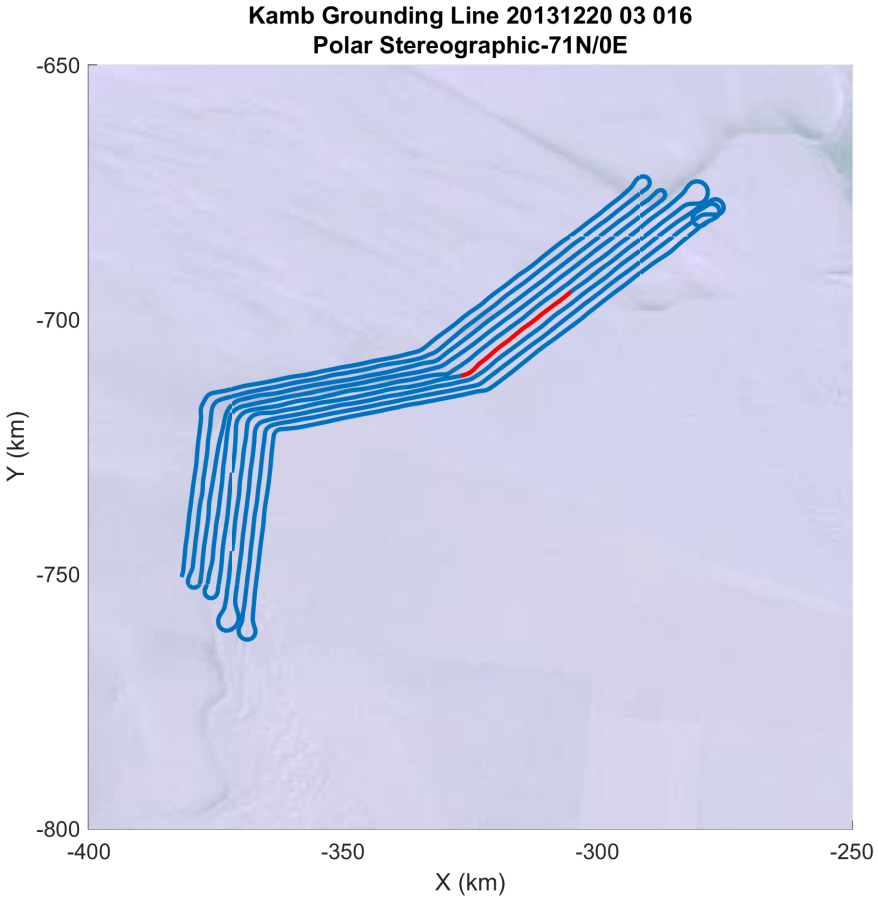

Left

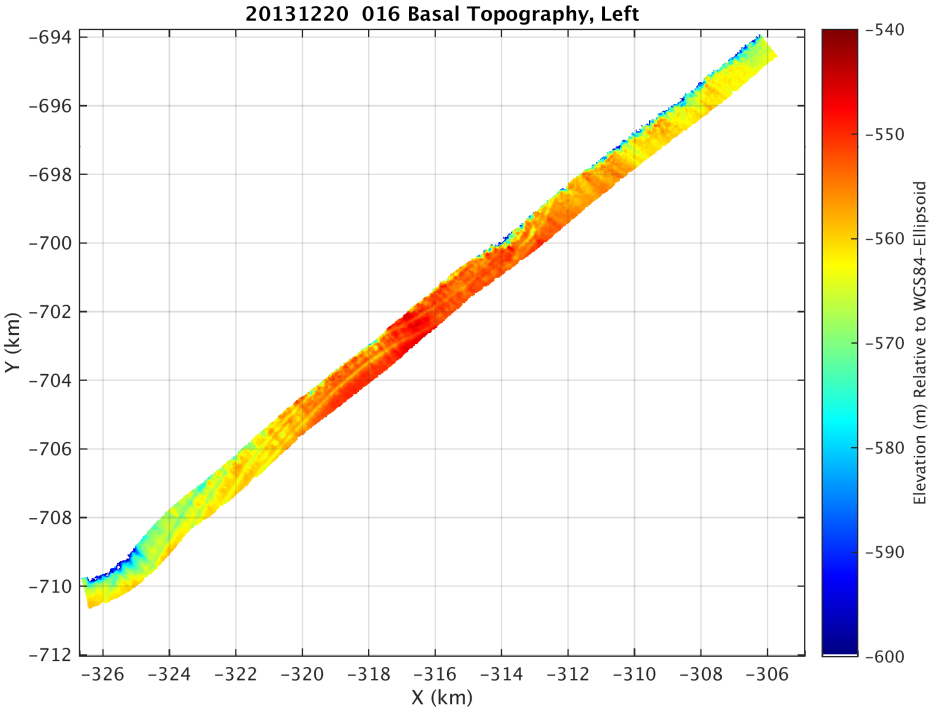
20131220 016 Basal Topography, Left
Y (km)
X (km)
Elevation (m) Relative to WGS84-Ellipsoid
-694
-696
-698
-700
-702
-704
-706
-708
-710
-712
-326
-324
-322
-320
-318
-316
-314
-312
-310
-308
-306
-540
-550
-560
-570
-580
-590
-600

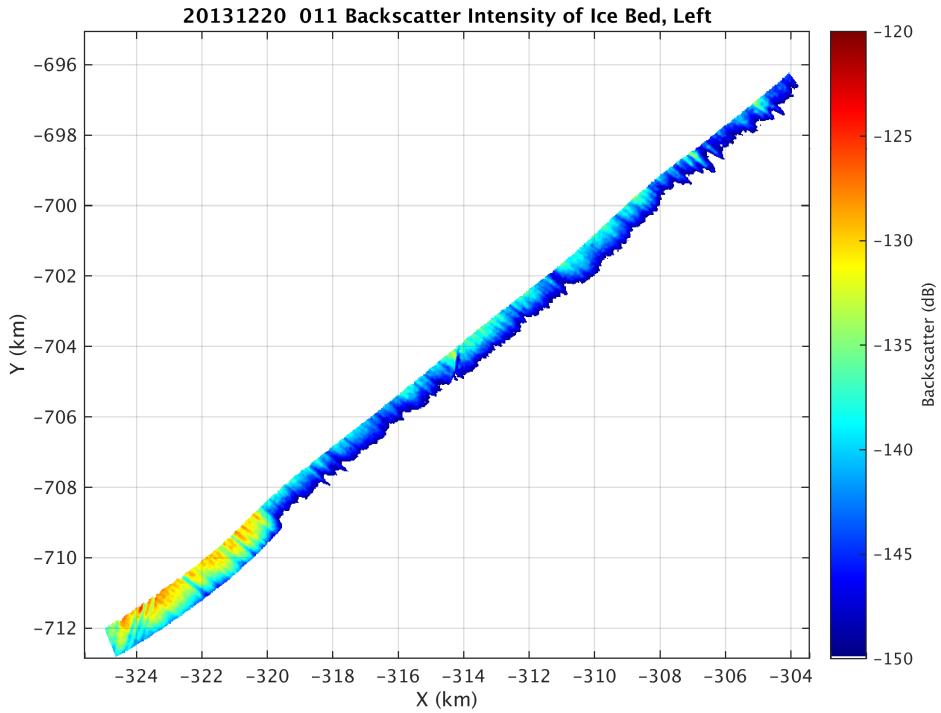
20131220 011 Backscatter Intensity of Ice Bed, Left
Y (km)
X (km)
Backscatter (dB)
-696
-698
-700
-702
-704
-706
-708
-710
-712
-324
-322
-320
-318
-316
-314
-312
-310
-308
-306
-304
-120
-125
-130
-135
-140
-145
-150

Nadir

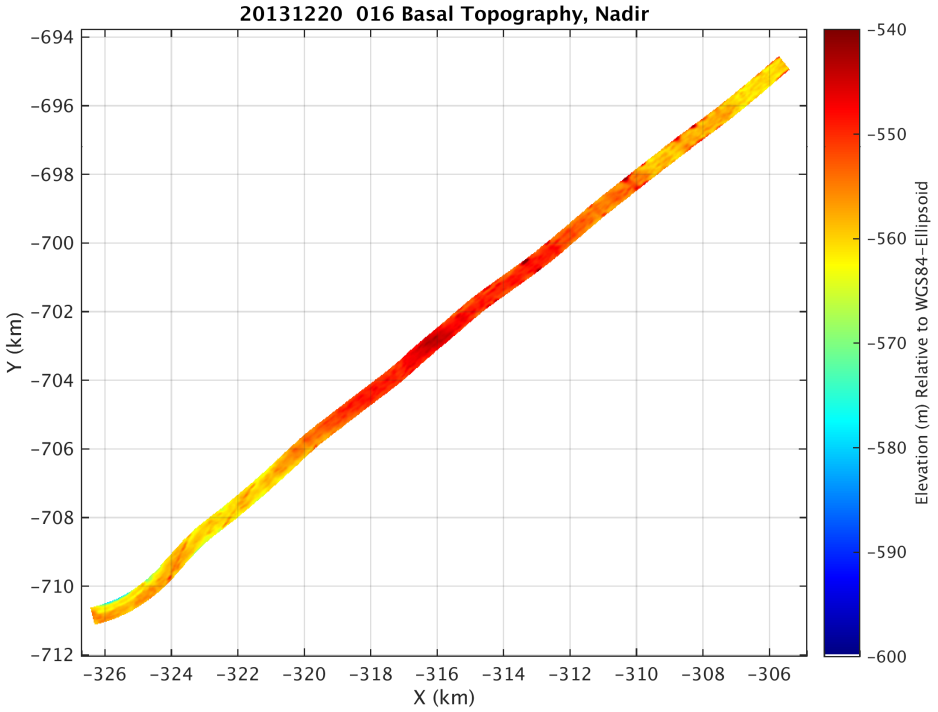
20131220 016 Basal Topography, Nadir
Y (km)
X (km)
Elevation (m) Relative to WGS84-Ellipsoid
-694
-696
-698
-700
-702
-704
-706
-708
-710
-712
-326
-324
-322
-320
-318
-316
-314
-312
-310
-308
-306
-540
-550
-560
-570
-580
-590
-600

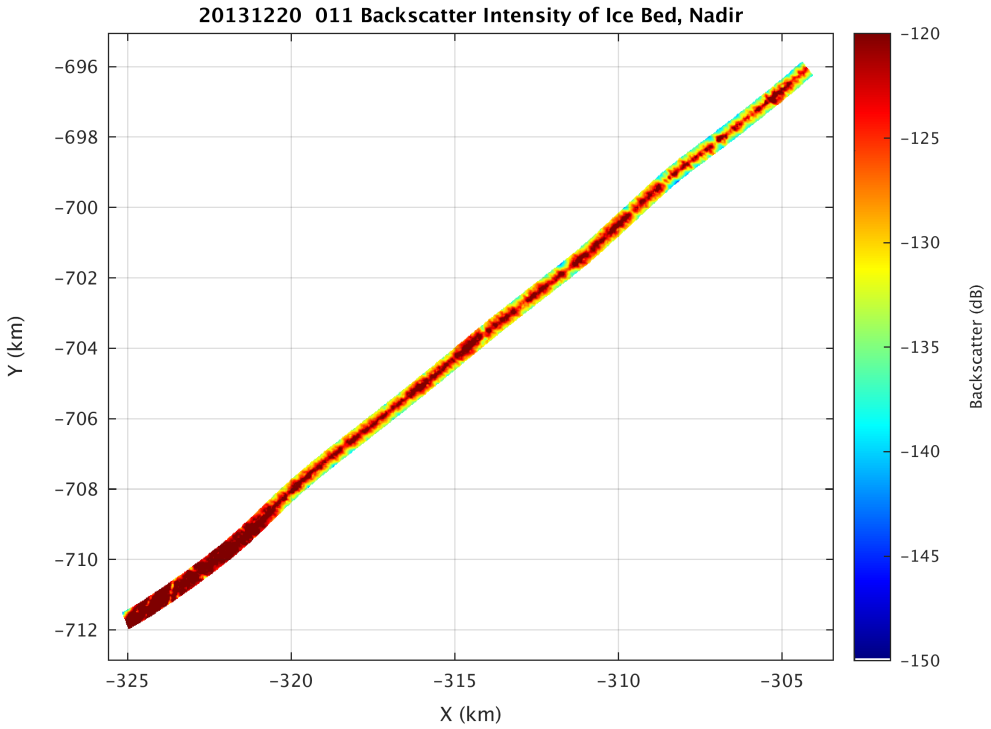
20131220 011 Backscatter Intensity of Ice Bed, Nadir
Y (km)
X (km)
Backscatter (dB)
-696
-698
-700
-702
-704
-706
-708
-710
-712
-325
-320
-315
-310
-305
-120
-125
-130
-135
-140
-145
-150

Right

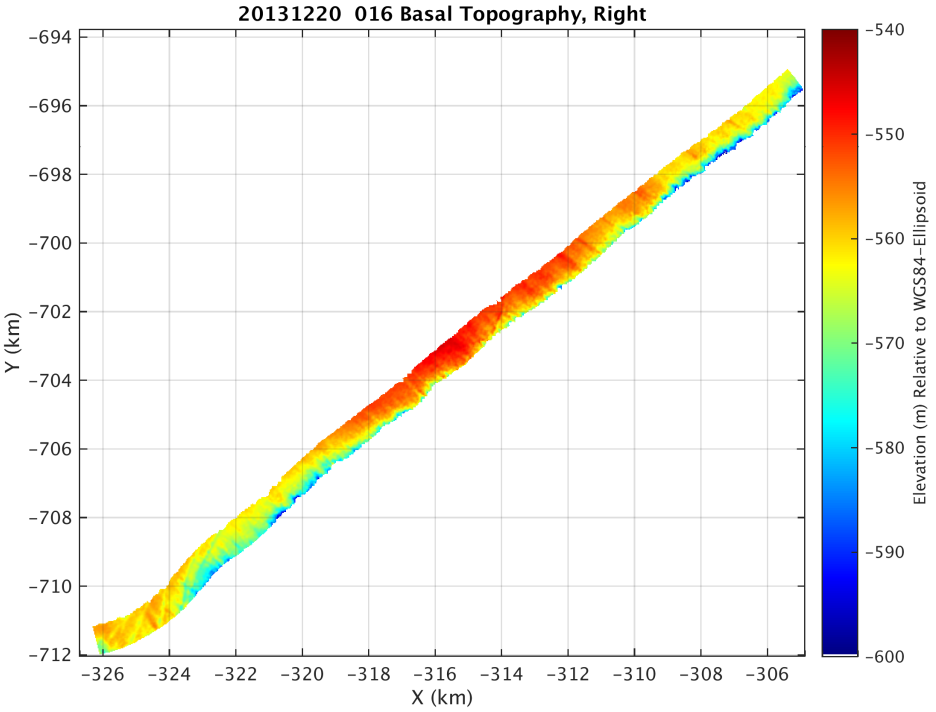
20131220_016 Basal Topography, Right
Y (km)
X (km)
Elevation (m) Relative to WGS84-Ellipsoid
-694
-696
-698
-700
-702
-704
-706
-708
-710
-712
-326
-324
-322
-320
-318
-316
-314
-312
-310
-308
-306
-540
-550
-560
-570
-580
-590
-600

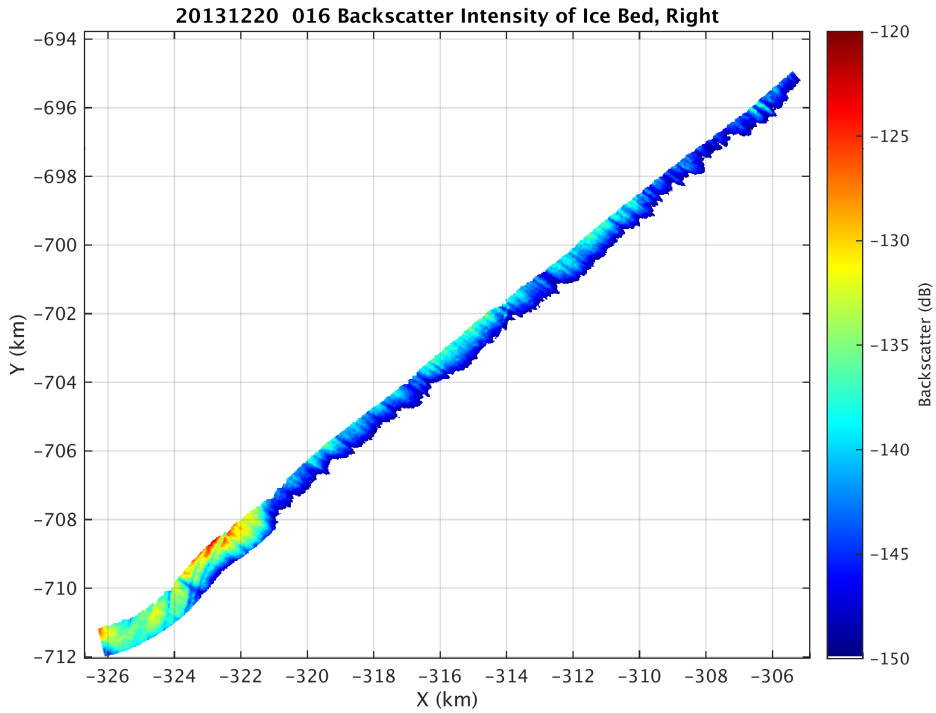
20131220_016 Backscatter Intensity of Ice Bed, Right
Y (km)
X (km)
Backscatter (dB)
-694
-696
-698
-700
-702
-704
-706
-708
-710
-712
-326
-324
-322
-320
-318
-316
-314
-312
-310
-308
-306
-120
-125
-130
-135
-140
-145
-150

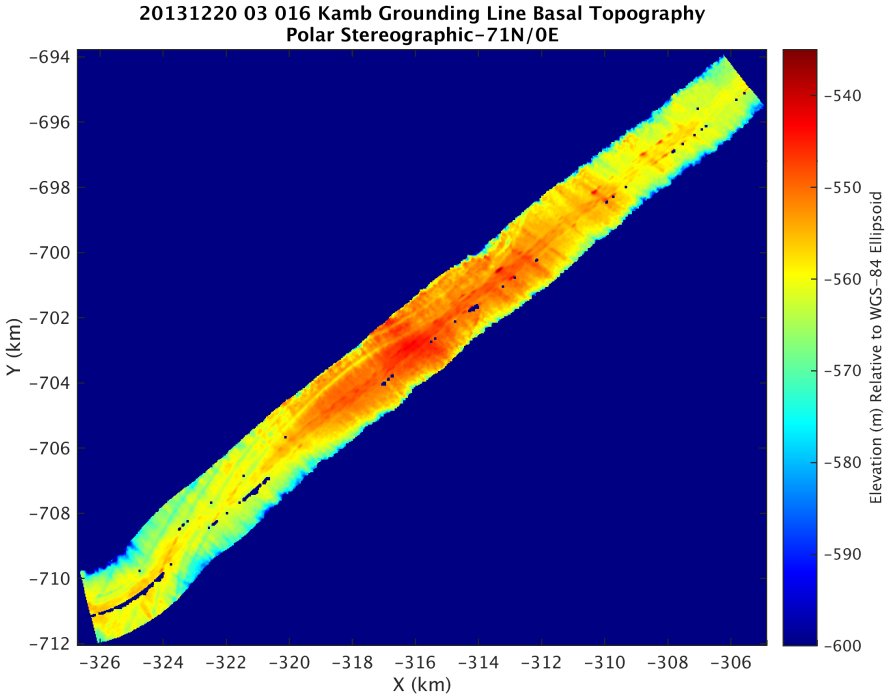

Figure 5-7 Merged DEM 20131220_03_016

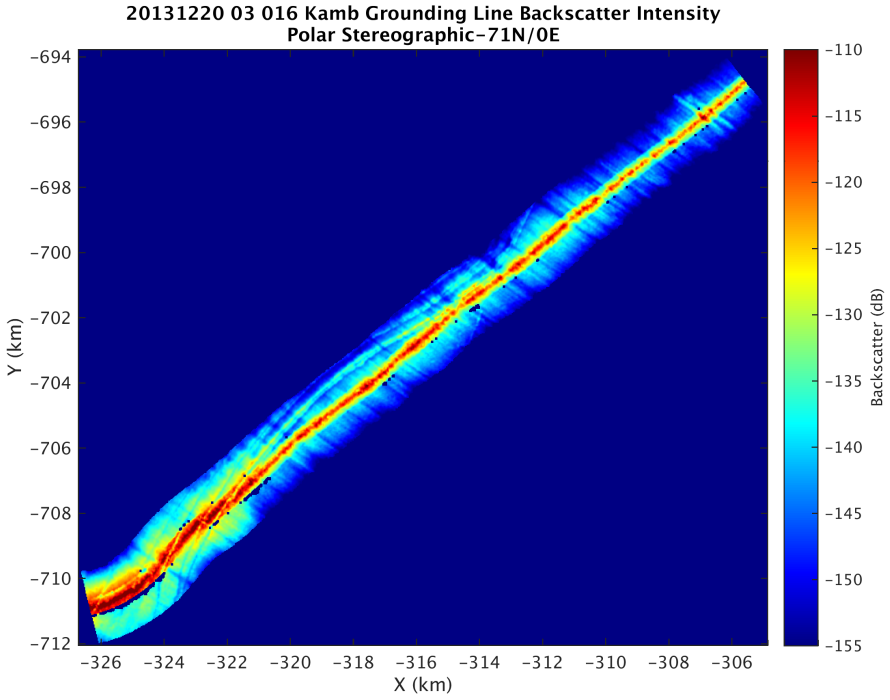

Figure 5-8 Merged backscatter map 20131220_03_016

5.3.4 Frame 019

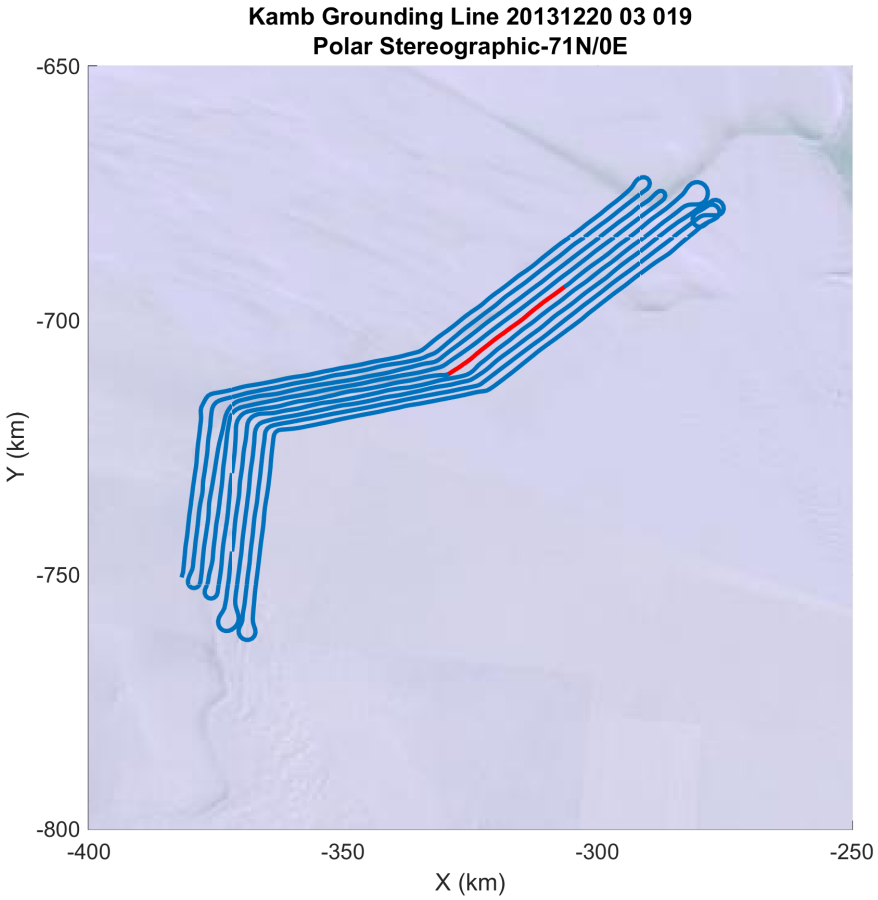

Left

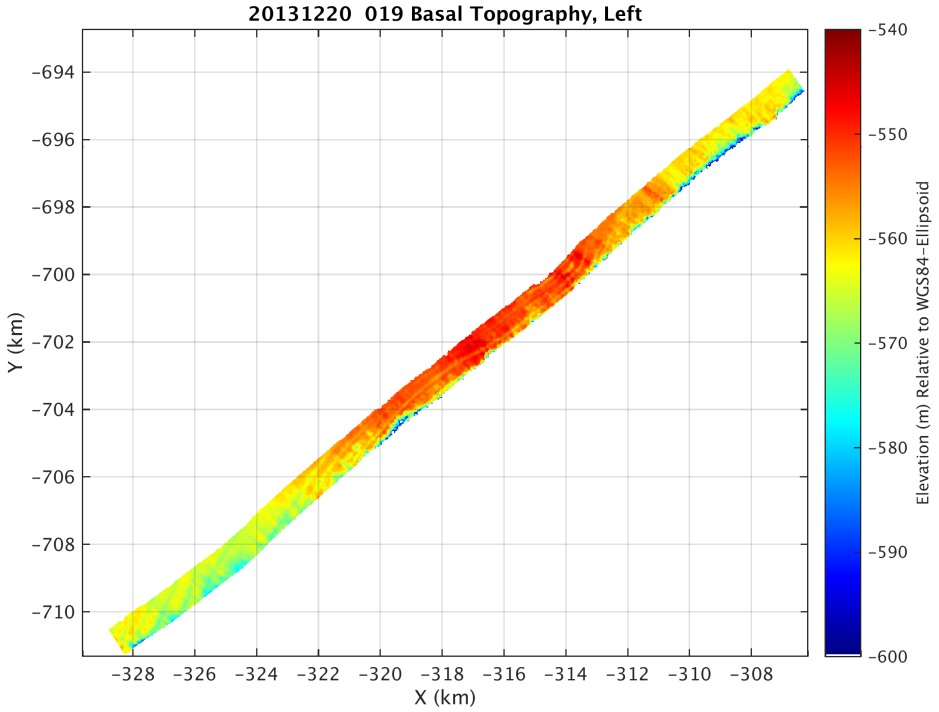
20131220_019 Basal Topography, Left
Y (km)
X (km)
Elevation (m) Relative to WGS84-Ellipsoid
-694
-696
-698
-700
-702
-704
-706
-708
-710
-328 -326 -324 -322 -320 -318 -316 -314 -312 -310 -308
-540
-550
-560
-570
-580
-590
-600

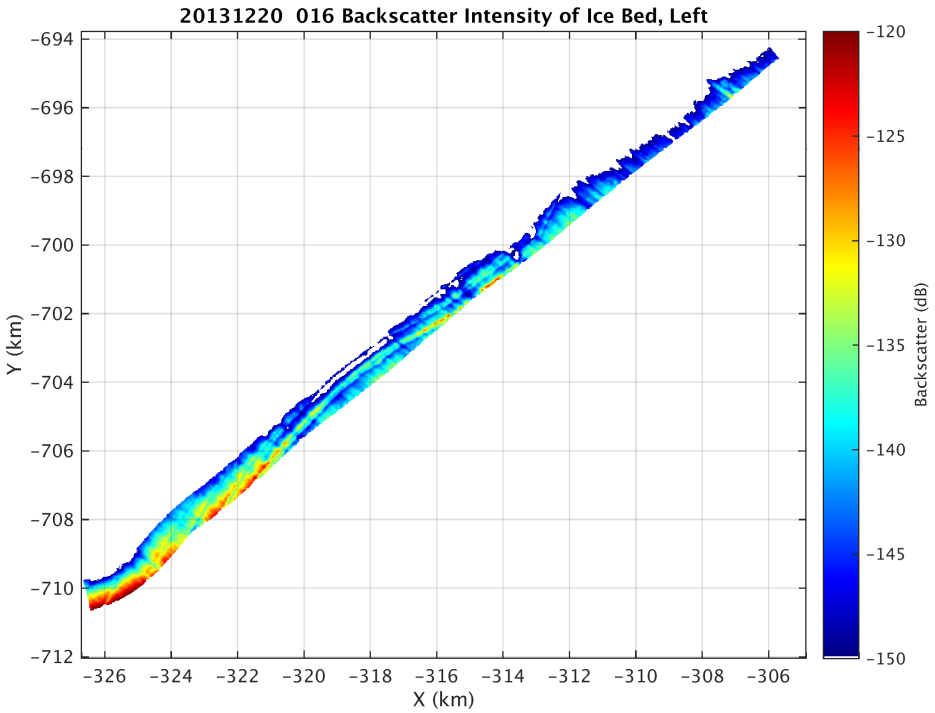
20131220_016 Backscatter Intensity of Ice Bed, Left
Y (km)
X (km)
Backscatter (dB)
-694
-696
-698
-700
-702
-704
-706
-708
-710
-712
-326 -324 -322 -320 -318 -316 -314 -312 -310 -308 -306
-120
-125
-130
-135
-140
-145
-150

Nadir

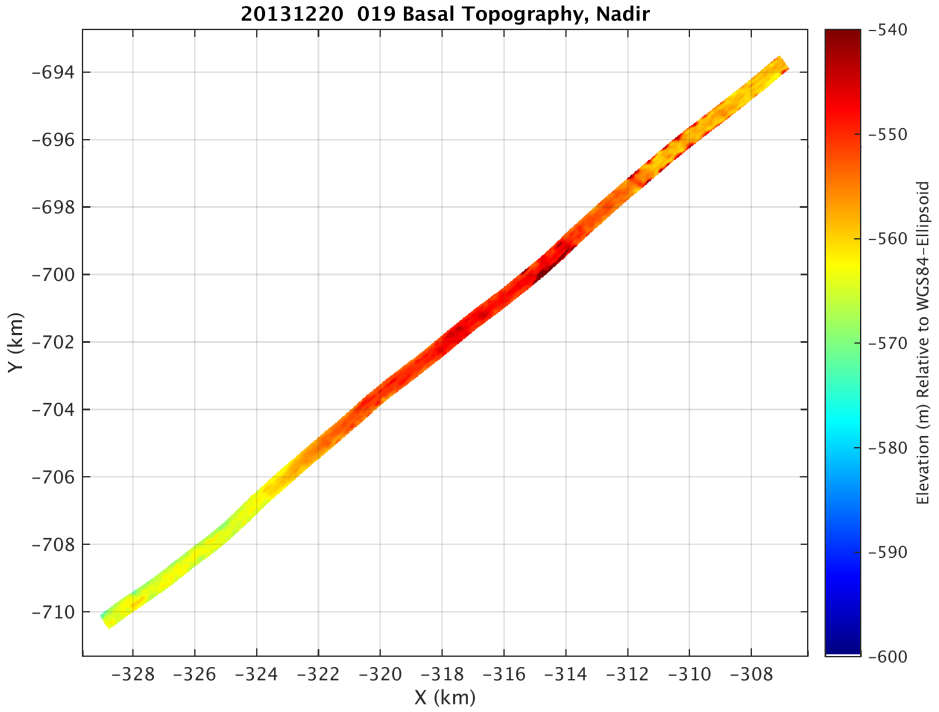
20131220 019 Basal Topography, Nadir
Y (km)
X (km)
Elevation (m) Relative to WGS84–Ellipsoid
-694
-696
-698
-700
-702
-704
-706
-708
-710
-328 -326 -324 -322 -320 -318 -316 -314 -312 -310 -308
-540
-550
-560
-570
-580
-590
-600

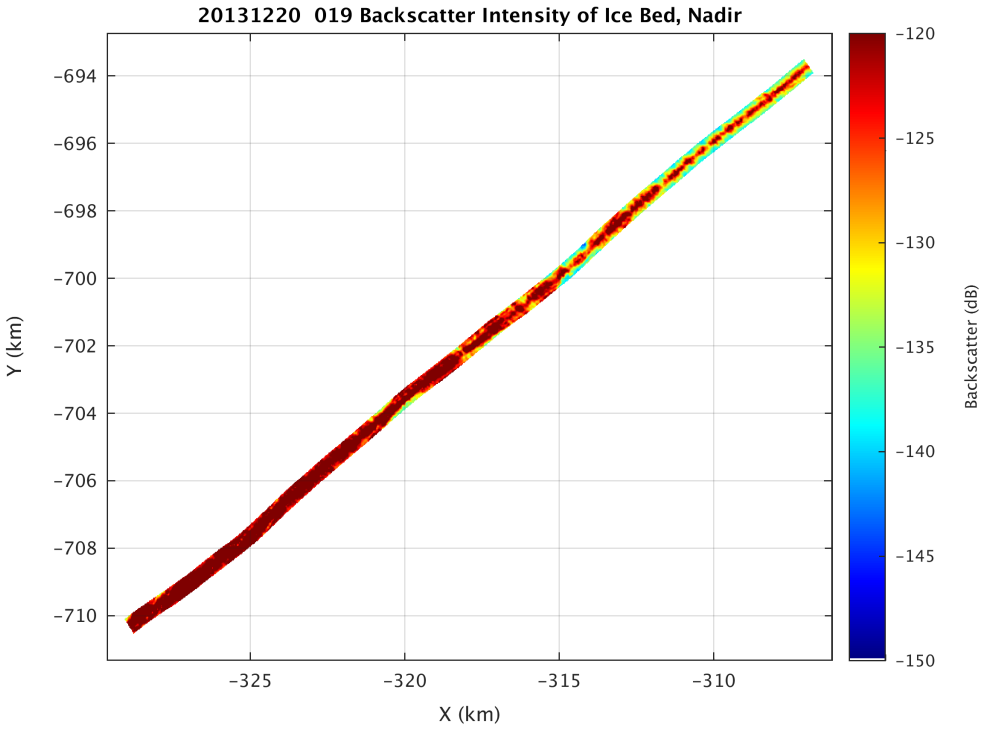
20131220 019 Backscatter Intensity of Ice Bed, Nadir
Y (km)
X (km)
Backscatter (dB)
-694
-696
-698
-700
-702
-704
-706
-708
-710
-325 -320 -315 -310
-120
-125
-130
-135
-140
-145
-150

Right

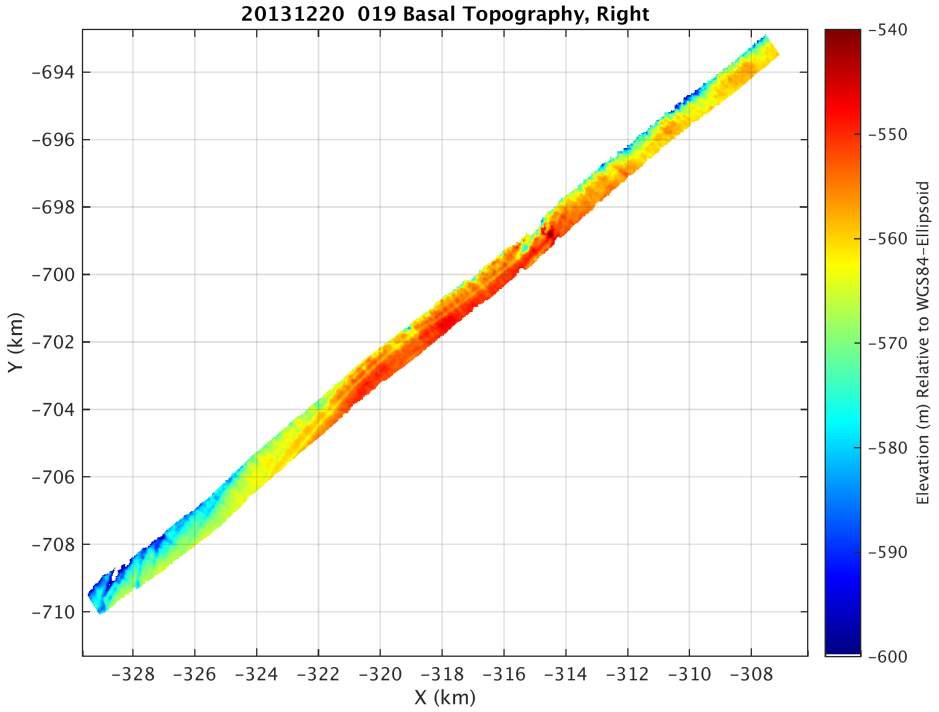
20131220 019 Basal Topography, Right
Y (km)
X (km)
Elevation (m) Relative to WGS84-Ellipsoid
-694
-696
-698
-700
-702
-704
-706
-708
-710
-328 -326 -324 -322 -320 -318 -316 -314 -312 -310 -308
-540
-550
-560
-570
-580
-590
-600

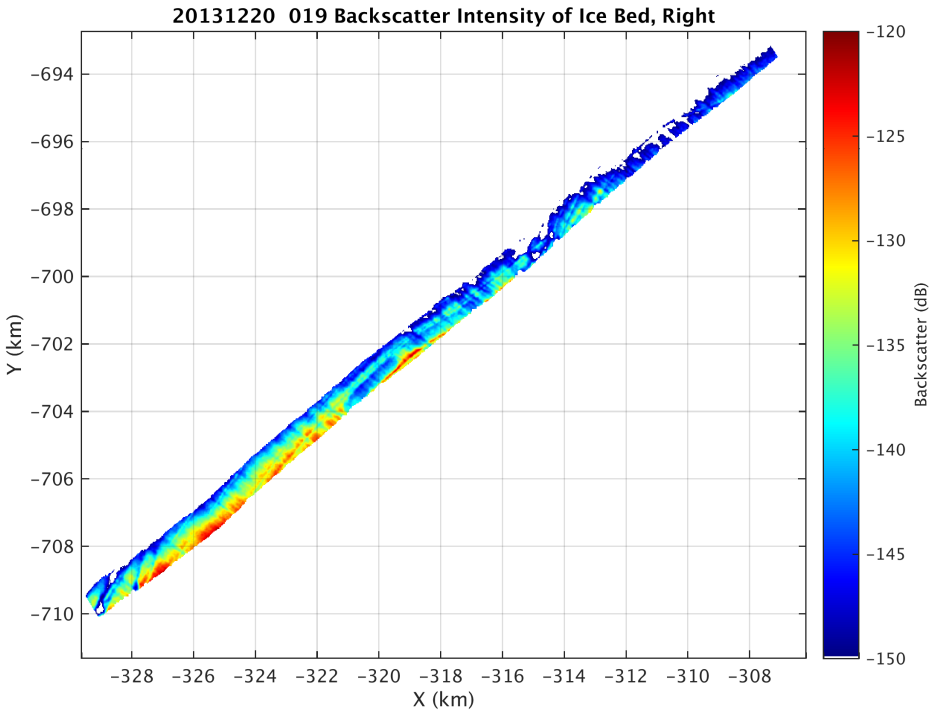
20131220 019 Backscatter Intensity of Ice Bed, Right
Y (km)
X (km)
Backscatter (dB)
-694
-696
-698
-700
-702
-704
-706
-708
-710
-328 -326 -324 -322 -320 -318 -316 -314 -312 -310 -308
-120
-125
-130
-135
-140
-145
-150

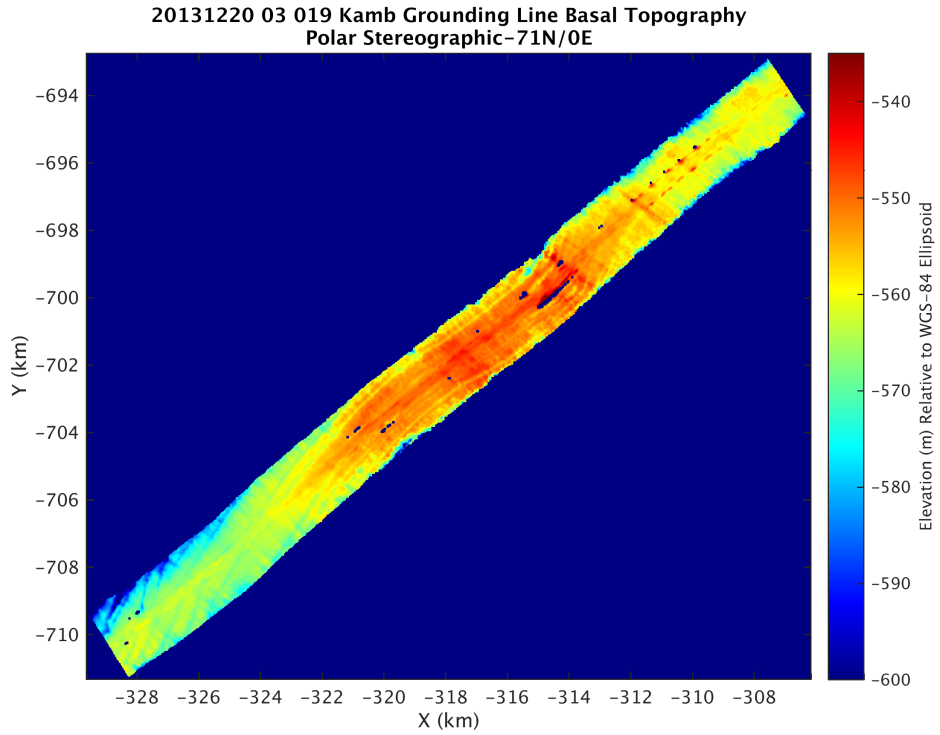

Figure 5-9 20131220_03_019 Merged DEM

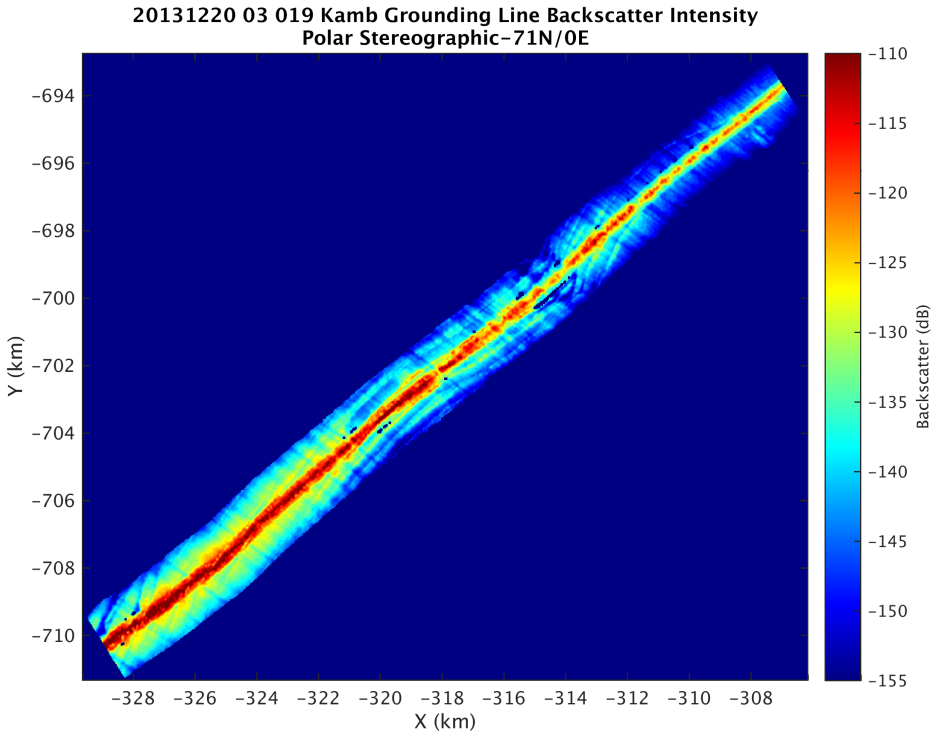

Figure 5-10 Merged backscatter map 20131220_03_019

Discussion

The tomographic images show clear features in certain cases that are being tracked over very long extents. In frame 19 for example, a strong curving channel is visible in the DEM from the right beam for approximately 20 km. A similar type of feature is visible on the left side as well. These features appear to be strongly correlated with the corresponding backscatter for each DEM suggesting that the features are real. Examination of the cross-track depth sounder profiles (described further in the next section) indeed show these bottom crevasse like features. The roughness scale of these rippling features varies less than ten meters in height in many cases between the peaks and valleys. An example of this rippling as measured by the depth sounder in one of the crossing lines used for evaluating the imaging performance is shown in Figure 5-11.

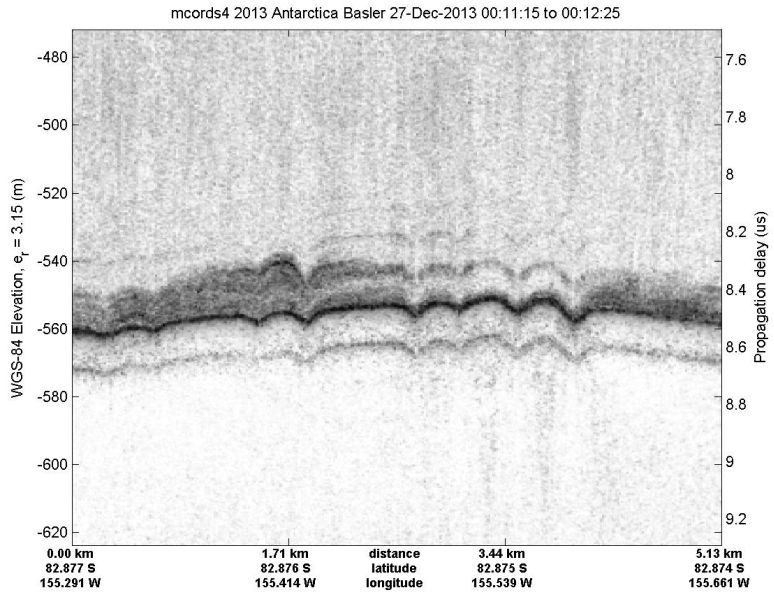

Figure 5-11 Bottom crevassing pattern measured by depth sounder on crossing line

Patterns of striations are also observable in the topography that appear as a horizontal ribbing orthogonal to the platform trajectory. The merged DEM shows continuity of these striations across beams and between parallel frames suggesting a continuous feature. The striations do not appear to coincide with elevation changes in the crossing depth sounder lines however. The continuity of the features suggests that the algorithm is tracking a real feature but it does not appear that these features are due to the basal topography of Kamb and may perhaps be attributable to the complexity of the basal properties of this ice stream that have been verified using video data obtained by means of boreholes drilled in the ice stream [22].

Figure 5-12 and Figure 5-13 show some of the features of Frame 19 in finer detail. These figures show the sidelooking swath of the merged DEM and backscatter map for a 1 by 2 km patch containing one of

these striation patterns. On the DEM we see the topography fall from -557 meters to -561 in the small channel then coming back up to -559 again on the other side. The backscatter of the pixels in this channel are approximately 4 dB lower than the values on the ridges. This channel also appears in the 20131227_06_007 low-altitude crossing line whose echogram was shown in Figure 5-11 and corresponds to the right most valley in the image and served as a validation for this drop in the backscatter.

Two ascopes from this validation are shown in Figure 5-14. The blue line contains the echo from the ridge or bank of the channel which appears at 6.9 μs with a strength of -88 dB. The red ascope contains the echo from the channel crossing. It appears slightly later at 6.94 μs, validating the elevation change seen in the tomographic DEM. The strength of the echo is -99 dB, 10 dB lower than the echo on the ridge. The consistency of this variation of backscatter over the channel in both the depth sounder echoes as well as the tomographic images suggests that the WDOA is in some cases capturing the arrival angles at the swath edges. It also validates the method used for estimating SNR using registration and beamforming. The large attenuation incurred over a small change in elevation may suggest a thin layer of water at the bottom of the channel that attenuates the signal.

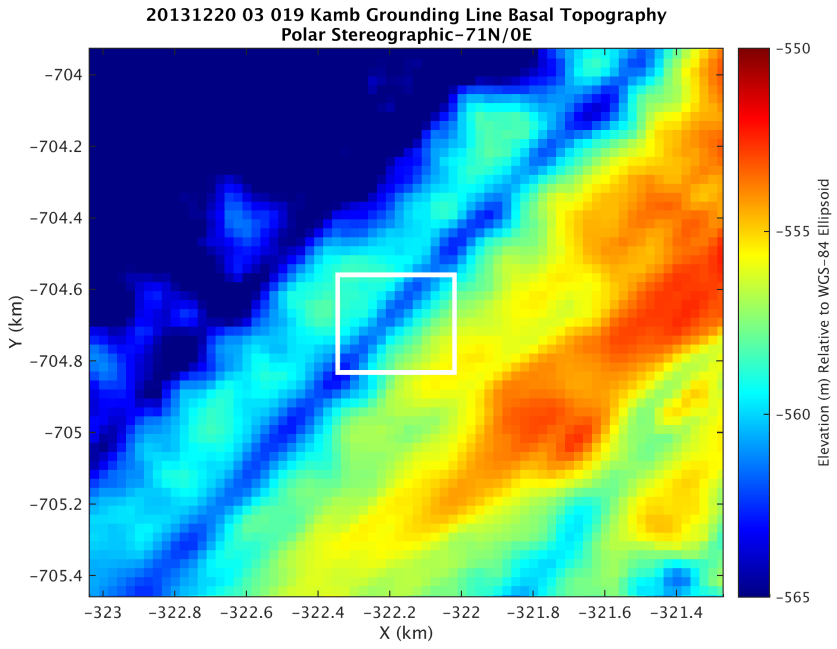

Figure 5-12 Topographic detail of channel observed 20131220 03 019 DEM

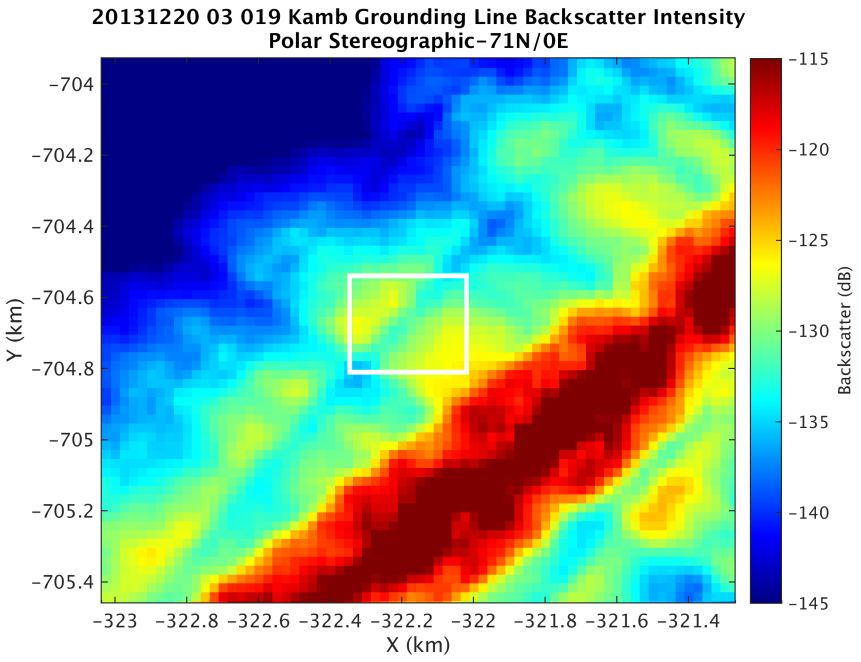

Figure 5-13 Corresponding backscatter of detailed topography shown above

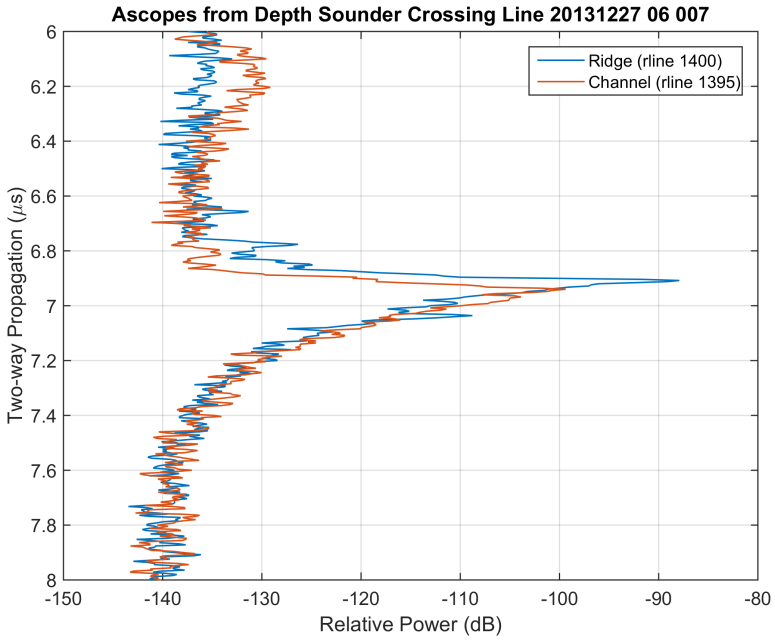

Figure 5-14 Validation of drop in backscatter over channel

The sidelooking beams reveal edge artifacts in their gridded DEMs. The roll off regions show in many cases correlation with low backscatter suggesting a possible correlation between the direction of arrival estimation and the SNR. We would expect to see the edges simply become noisy as the SNR drops off but instead we see dips consistent in elevation. It seems to be an indication of the DOA latching onto the lower

θ constraint at the edges of the swath but it's not clear why it tends to one side. Artifacts are also visible in the nadir swaths. To do surface extraction at nadir, the MLE DOAs are rasterized into tomographic slices by binning them into discrete uniformly spaced arrival angle bins and mapping the estimated power into each pixel. This forms a slice similar to the MUSIC slice shown in Figure 5-15. The samples of the surface are then taken to be the maximum of each column corresponding to DOAs within the field of view similar to that shown in the figure below.

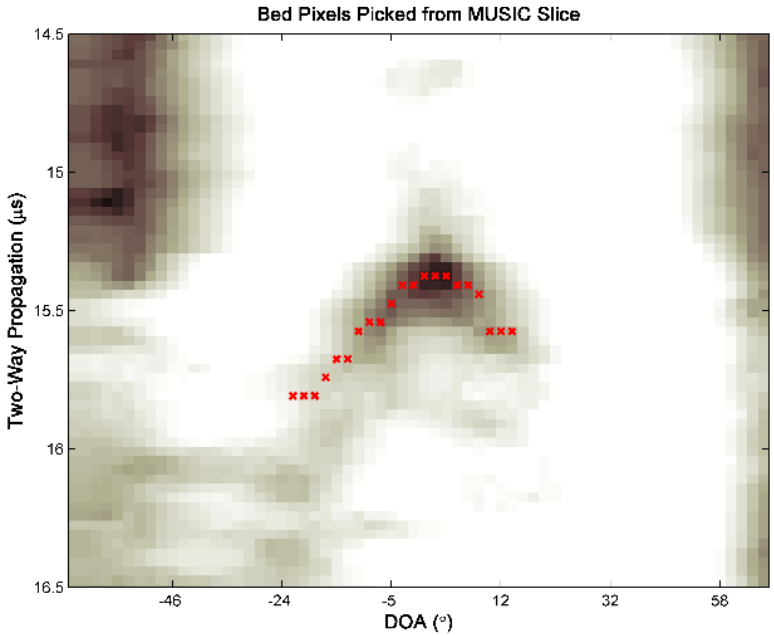

Figure 5-15 Example of a MUSIC slice and pixels picked during surface extraction

When a column does not contain a dominant basal scatterer, the max will be assigned to some other scattering source within the field of view or noise. Sounder echograms from the Kamb grid suggest that in some places layover is likely to be an issue near nadir. Towards the edges of the swath as the SNR drops off, the likelihood of surface clutter dominating increases. The nadir swath in frame 19 shows edge artifacts in the southeast corner that appear to be correlated with lower SNR (compared to the rest of the frame). Here the algorithm is potentially becoming more sensitive to the surface and exhibiting a bias in the topography estimate.

5.4 Crossover Analysis

Two low altitude sounder lines are available for cross over analysis: 20131227_06_007 and 20131227_04_002. The sounder profiles are along the direction of flow of the now terminated ice stream. The map below indicates the entire Kamb Grounding Line grid in blue, the imaged frames in red and the

crossing lines in green. The depth sounder echogram for the more southeastern line is shown along-side the map showing the bed.

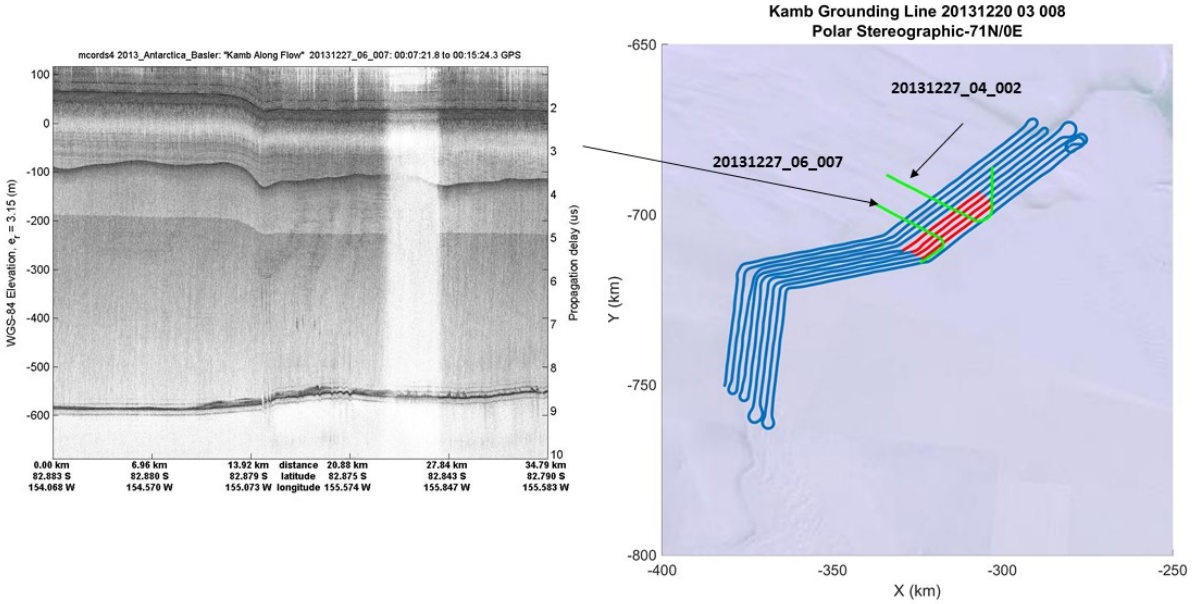

Figure 5-16 Map geolocating Kamb Grounding Line grid, tomography frames and crossing lines (right) along with depth sounder echogram (left). The vertical stripe of weak scattering in the echogram is due to the aircraft turning

The tomographic basal maps have been merged into one image for illustrating the continuous topography as well as the backscatter of the four frames. The depth sounder crossing lines are plotted over the merged DEMs. The sounder bed elevations as well as bed elevations from the tomographic DEMs are all mapped to the same color scale ranging from -600 meters to -540 meters (relative to the WGS-84 Ellipsoid). Sparsity in the tomographic DEM is due to the use of SNR thresholding for suppressing noise during reconstruction of the ice bed topography.

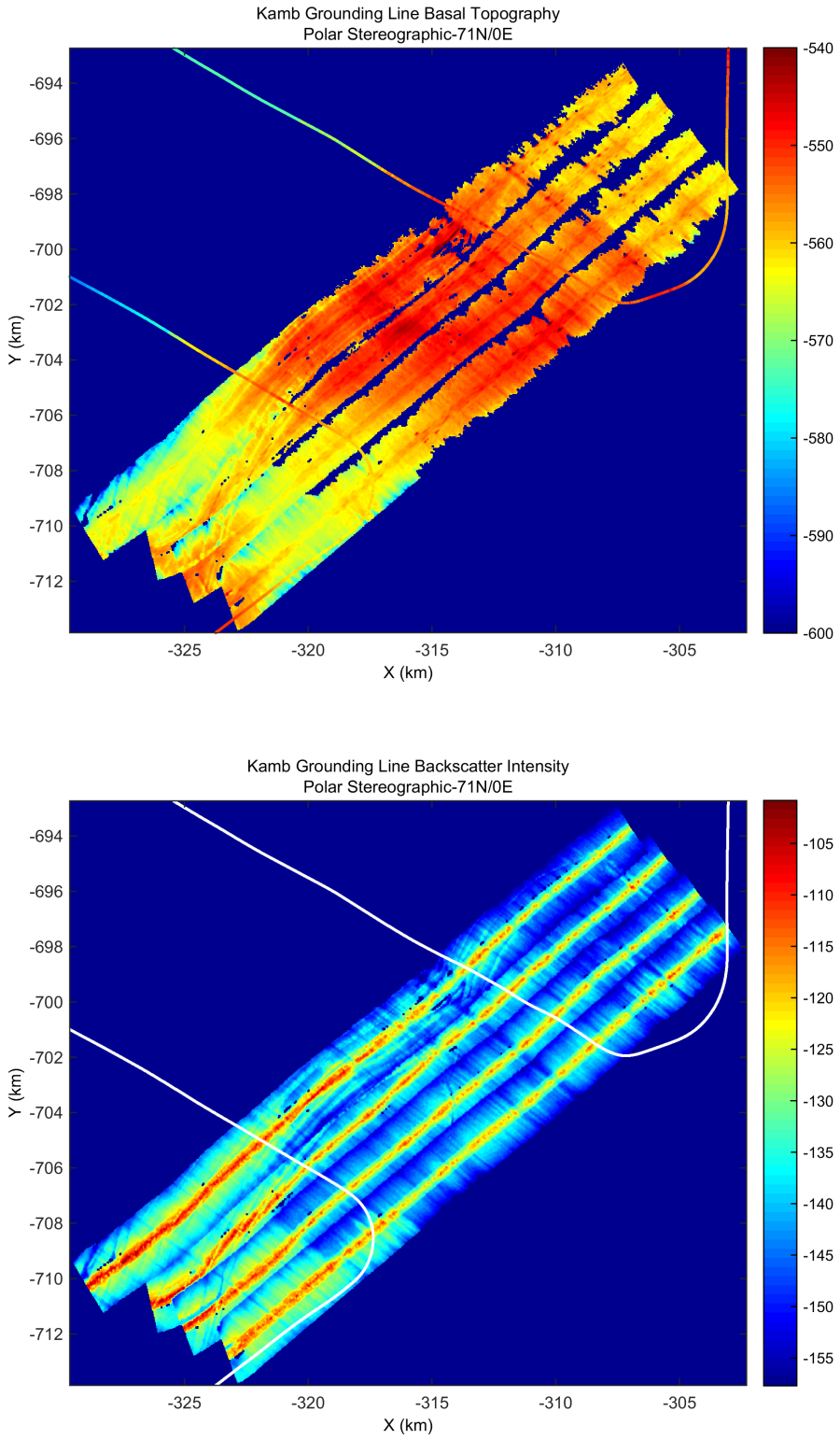

Figure 5-17 Merged swaths from all four frames showing topography (top) and backscatter (bottom)

The sounder profiles from the two low altitude crossing lines are shown in Figure 5-18 and Figure 5-20 respectively. The profiles for each look direction are color coded as indicated. Both profile comparisons show a negative bias of the elevation estimates obtained from the tomography results. The RMS error of the elevation measurements is 5.4 meters for the 20131227_06_007 crossing and 3.8 meters for the 20131227_04_002 crossing. The distribution of the errors are shown in Figure 5-19, demonstrating the negative bias of the tomographic DEMs.

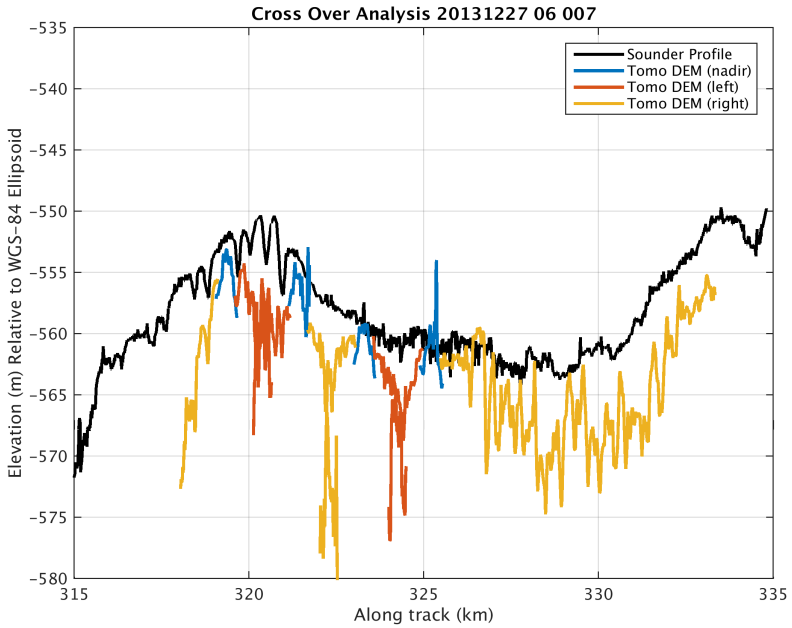

Figure 5-18 Comparison of 2013127_06_007 depth sounder profiles and profiles from tomographic DEMs

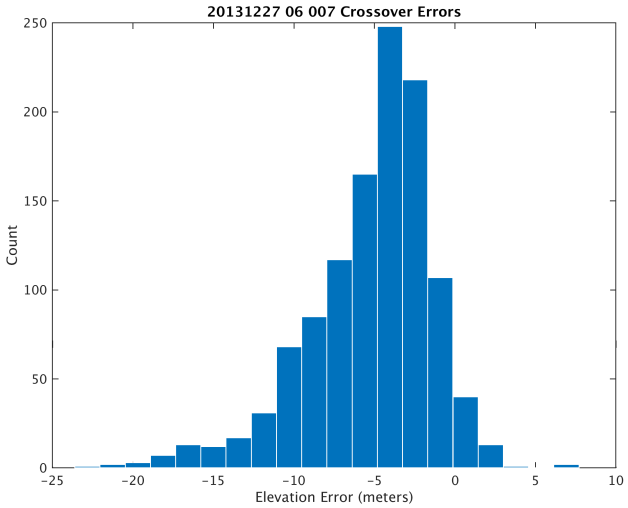

Figure 5-19 Distribution of elevation errors for 20131227_06_007 crossing

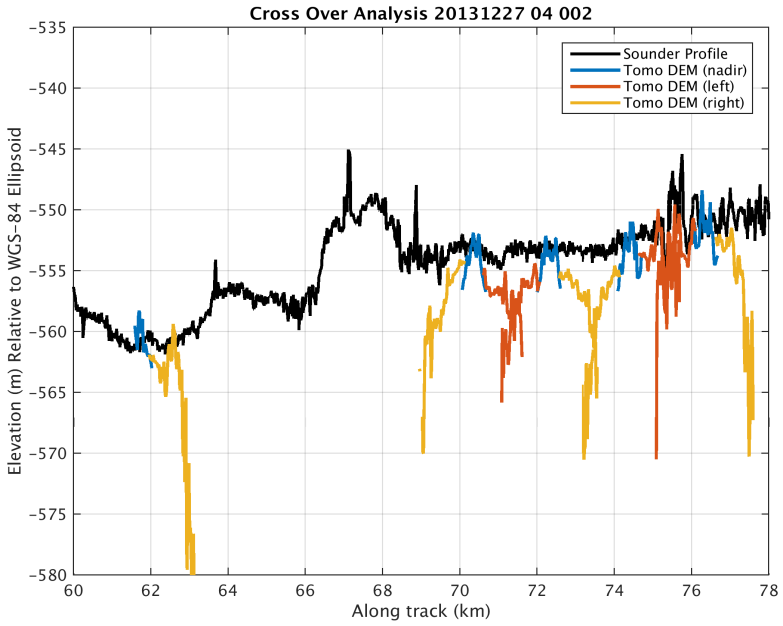

Figure 5-20 Comparison of 2013127_04_002 depth sounder profiles and profiles from tomographic DEMs

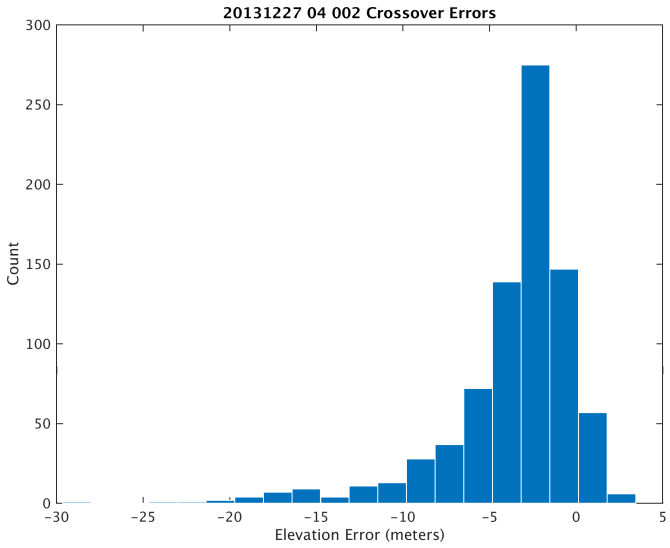

Figure 5-21 Distribution of elevation errors for 20131227_04_002 crossing

The tomographic profiles are obtained by querying each DEM along the depth sounder's crossing line. In a similar fashion, the backscatter map was queried to obtain measurements of backscatter along the flight path of the crossing line. This result demonstrates strong correlation elevation errors and SNR. For each cross over, the comparison of elevation profiles is plotted along with the backscatter along the track. These results are shown in Figure 5-22 and Figure 5-23. The largest elevation errors appear at the edges of the

sidelooking beams where the backscatter has fallen off by approximately 20 dB. The elevation errors do appear to become noisier however.

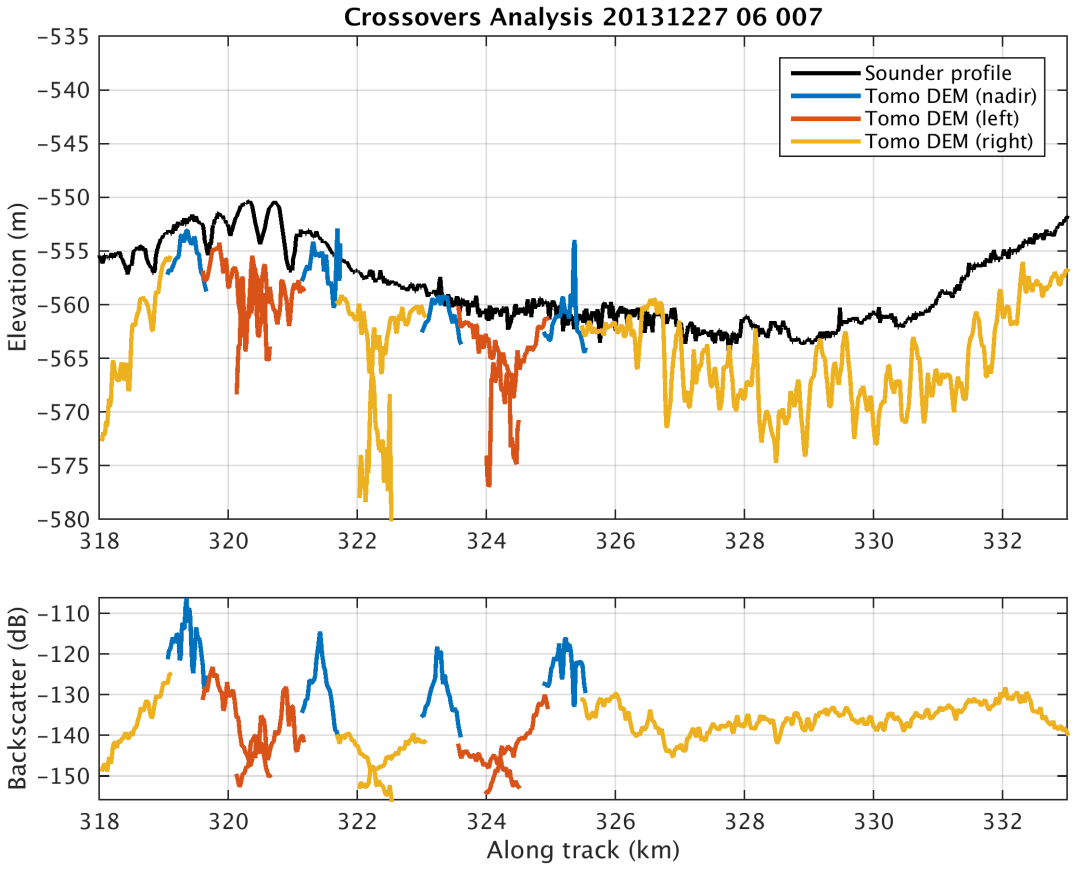

Figure 5-22 SNR dependence of elevation errors 20131227_06_007

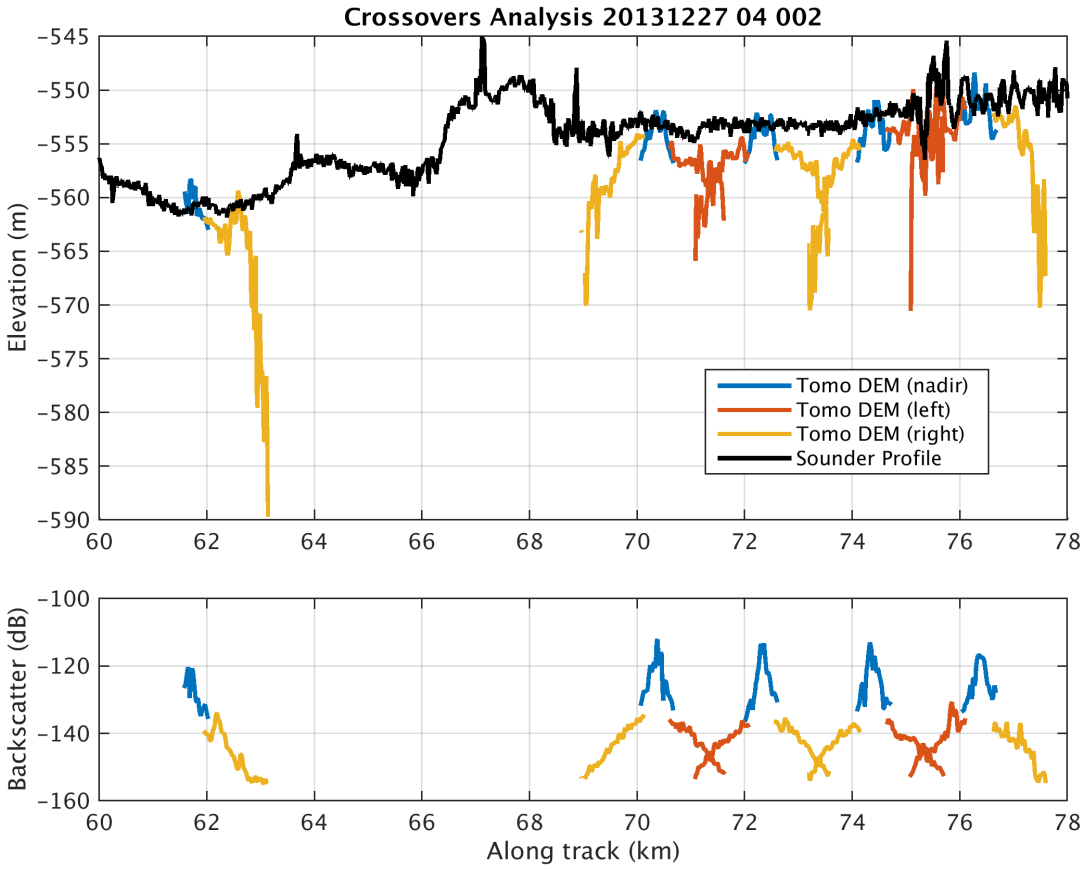

Figure 5-23 SNR dependence of elevation errors 20131227_02_004

Sources of error for the tomographic DEMs include: 1) a possible SNR bias of the WDOA estimator, 2) improper modeling of propagation in firn, 3) steering vector errors, and 4) sloping facets at the surface which affect the refraction into the ice. For this project, a dielectric of 3.15 was used throughout. The possibility of an error in the dielectric is considered using the following figure. For an echo returning from the edge of the swath, we expect a DOA of 30° for $\epsilon_{r-ice} = 3.15$. The figure shows the result of varying the dielectric from 3 to 3.2 and the actual DOA that's obtained. A corresponding elevation error in red is shown where the height above surface is taken to be 1,800 meters and the ice thickness is 570 meters. The result shown suggests that even a small error in the dielectric will produce large errors in elevation at this

altitude. A dielectric error of 0.01 translates to a 1 meter elevation error. Further investigation of this error is left for future work.

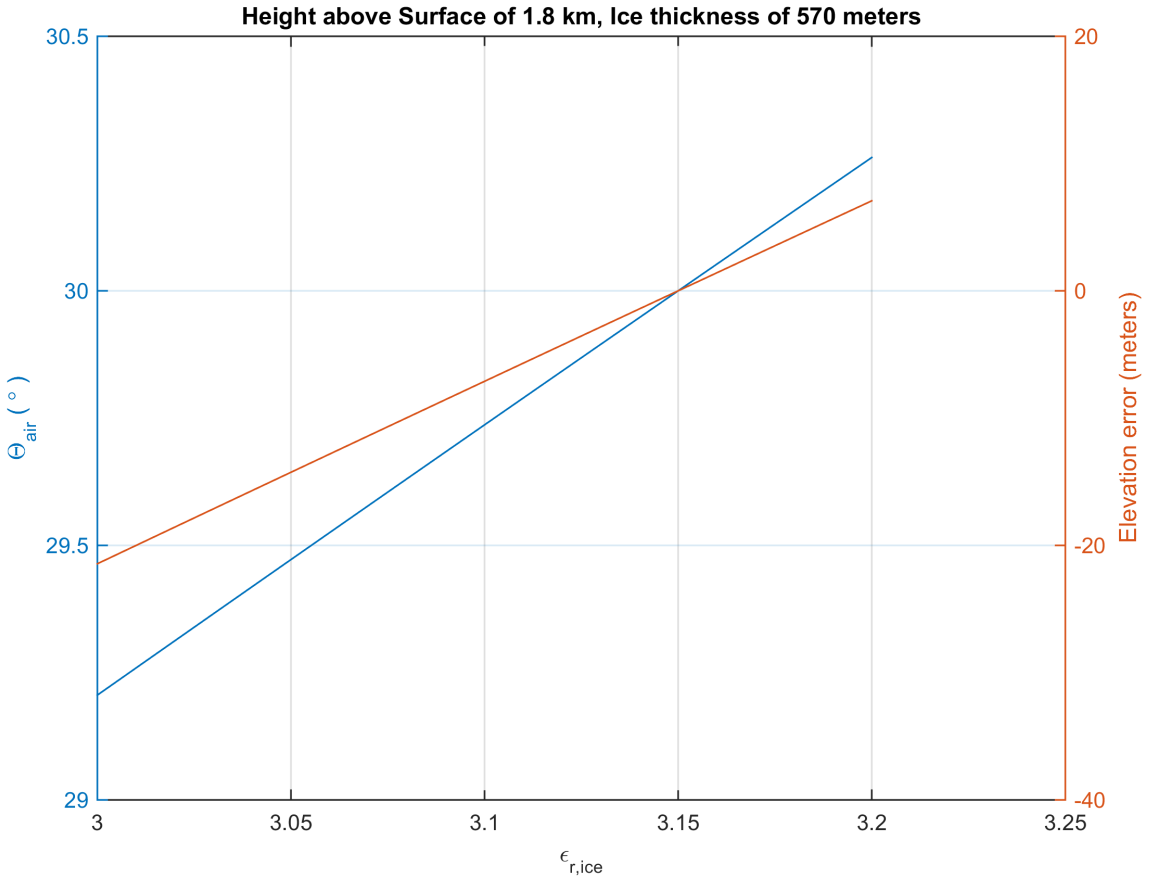

A correction factor was used to amplify the estimated DOAs by a factor of 1.03. The use of the correction factor appears to improve the quality of the merged swaths that are shown in Figure 5-24 below.

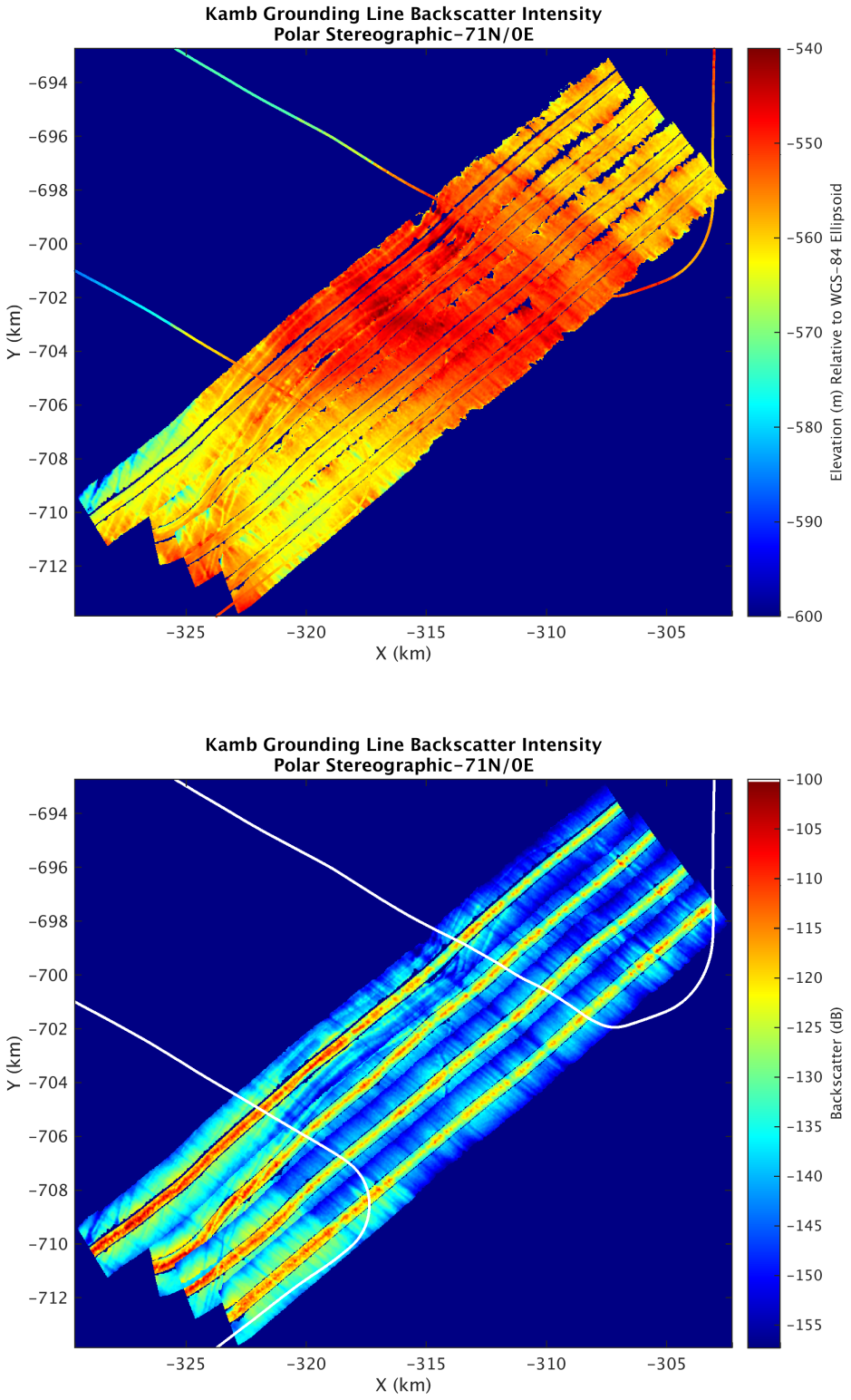

Figure 5-24 Merged tomographic DEMs (top) and merged backscatter map (bottom) after correction

The crossovers with corrections are shown in Figure 5-25 and Figure 5-26. This scaling appears to correct some of the features with sufficient SNR and we see the sidelooking left beam (yellow) aligning more properly with the dips and valleys between along track values 318 and 320 km for example in 20131227_06_007 result. Scaling the DOAs reduced the RMS elevation error to 2.73 meters for the 20131227_06_007 result. The RMS error for the corrected 20131227_04_002 result is 1.71 meters.

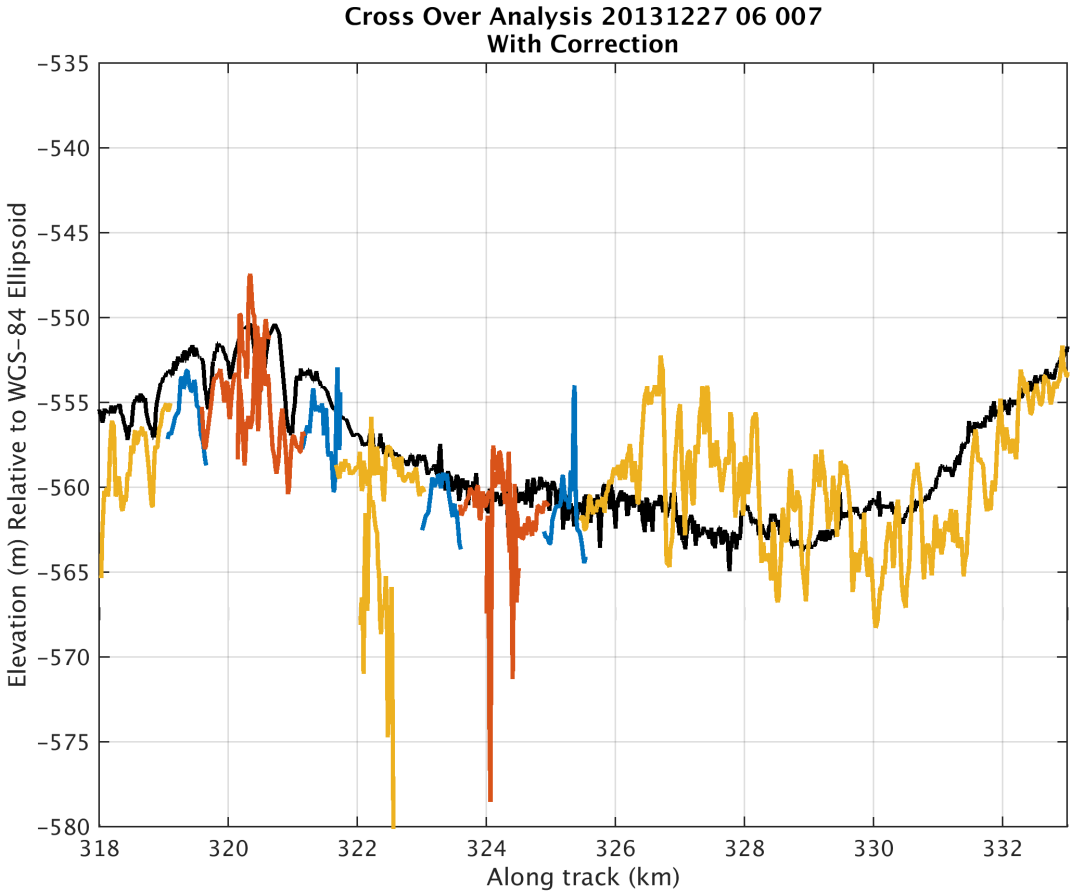

Figure 5-25 Cross over comparison with DOA correction 20131227_04_002

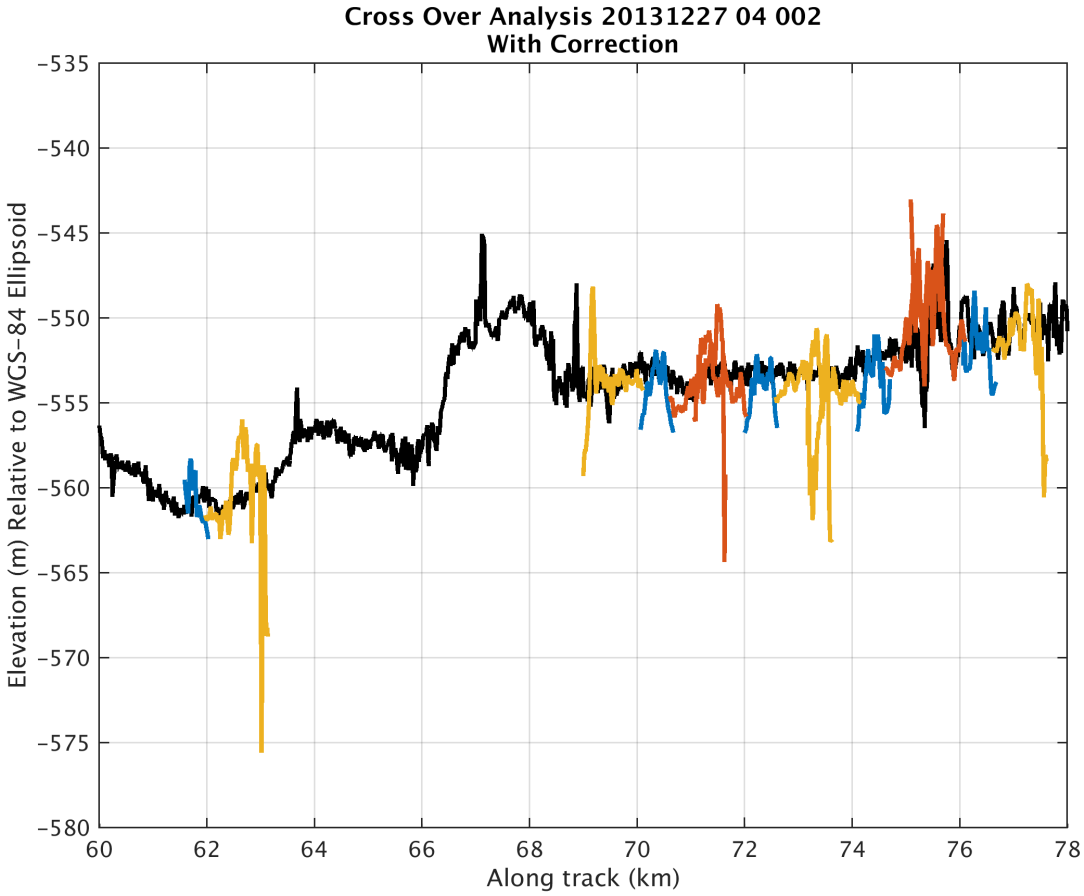

Figure 5-26 Cross over comparison with correction factor 20131227_04_002

5.5 Chapter Summary

This chapter presented tomographic basal maps obtained from wide swath, multibeam data collected over the Kamb Ice stream in West Antarctica. The results demonstrated the use of multiple transmit beams for imaging large areas and also validated that the WDOA algorithm was tracking features off nadir in the sidelooking beams. Detection of small features at the grounding line demonstrated the UWB depth sounder's ability to image the cross track with fine resolution. The results emphasized the scientific utility of this sensor in its ability to capture changes in backscatter of the shallow bottom crevasses. Finally a cross over analysis showed correlation of received SNR with elevation errors possibly due to steering vector errors. Scaling the DOAs by a factor of 1.03 reduced the bias and helped align features between the tomography result and the depth sounder profile and also reduced the RMS elevation error to a value that was closer to the range resolution of the radar. The elevation error is not expected to perfectly correlate

with the range resolution though since part of the resolution is provided by the direction of arrival estimation which is dependent on other factors such as cross track array size and SNR.

Chapter 6

Conclusions

6.1 Summary

A space-time direction of arrival method has been presented for handling wideband geometries in the application of 3D tomographic ice sheet imaging. This technique obtains an estimate of the direction of arrival by fitting a measured space-time data covariance structure to a model of the DCM. The DCM models the complex cross correlation function between two sensors at multiple lags as the cross correlation between the system response functions of each channel that is dependent on target arrival angle and SNR. The method is inherently better suited for targets off to the side that can be more appropriately modeled as point scatterers. Like MLE and MUSIC, the WDOA algorithm requires a priori knowledge of the number of sources as well as the requirement of stationarity of targets over the neighborhood of pixels used to capture the statistics of the data.

One of the advantages of the WDOA over other wideband direction of arrival methods is that it does not require sub-banding the data. Sub-banding degrades range resolution and increases computational complexity. The WDOA does require an observation of W fast time samples to fully model the received signal so a resolution degradation of at most W must be tolerated. But as was mentioned in Chapter 4, the widening factor W is about 10 times smaller the number of required bands N_b for sub-banding with the Basler data set. While the WDOA does degrade resolution, it is not as much of a degradation that is required for a wideband approach such as WBMLE.

The major challenge associated with the WDOA is computational cost as it requires an N_s dimensional search of the solution space to obtain a DOA estimate for every pixel in the scene. Some measures have been taken to alleviate computational cost. DOA constraints have been incorporated to constrain the search and fast time bin restrictions have been integrated to limit processing to those pixels that are most likely to contain basal scattering. The most beneficial improvement in computation speed was realized by writing a native C version of the cost function that is evaluated by fmincon as this eliminated a large amount of overhead required by MATLAB's slow interpreter.

A basic simulator was developed for studying direction of arrival estimation in wideband signal environments. The simulator was used to demonstrate the performance degradation of the narrowband methods in wideband imaging geometries. Both narrowband and wideband Maximum Likelihood Estimators of arrival angle were implemented to this end. The narrowband MLE was verified against results presented in [6], which provided the opportunity to consider the performance of the WDOA in narrowband configurations. The results of the simulations suggested that while the narrowband methods may be sufficient for imaging with the nadir beam, they are inadequate for imaging targets off to the side. Especially at the large incidence angles, the WDOA outperforms narrowband MUSIC and MLE.

Tomographic basal maps of topography and backscatter intensity were generated from multibeam wide-swath data collected by the UWB radar depth sounder when it was operated from the Basler BT-67 aircraft during the 2013 Antarctic mission. MLE was used for imaging near nadir and the WDOA was used to image sidelooking swaths on the left and right sides. The results highlighted the scientific utility of the UWB version of MCoRDS/I for measuring basal characteristics with fine resolution. A cross over analysis showed bias in elevation error that increased at the swath edges. The inclusion of a scaling factor reduced the observed bias. After applying this correction factor, RMS errors were reduced from 5.4 meters to 2.73 meters along the 20131227_06_007 profile and from 3.8 meters to 1.71 meters along the 20131227_04_002 profile.

6.2 Recommendations and Future Work

Without the use of a corrective scaling factor applied to the DOAs, the estimated ice-bed elevation suffered errors that increased at the edges of the swath. Further investigation of this issue should be carried out to isolate the major contributing factor to this observation. To rule out the possibility of an error in the assumed dielectric, the algorithm should be used to reconstruct topography at the air-ice interface. This should be completed preferably where the data are collocated with lidar measurments that can serve to validate the technique.

Simulations and processing have suggested that the performance of any of the direction of arrival techniques is dependent on context and we should be careful to predict which DOA estimator will outperform the other based solely on simulation alone. The comparative performance really should be verified experimentally where large amounts of data are imaged with each method (MLE, MUSIC, WBMLE, WDOA) and crossovers are compared. Ideally, this would be done in conjunction with a detailed crossover analysis for each platform and array. Finally, this project illuminated the need for a robust and smart algorithm for optimal surface extraction. This would be some algorithm that minimizes a global cost function informed by the cost of DOA solutions as well as cost of the surface being extracted.

Works Cited

[1] A. Shepherd, E. Ivins and others, "A reconciled estimate of ice-sheet mass balance," *Science,* vol. 338, no. 6111, pp. 1183-1189, 2012.

[2] T. Stocker and a. o. (eds), IPPC, 2013: Climate Change 2013: The Physical Science Basis. Contribution of Working Group I to the Fifith Assessment Report of the Intergovernmental Panel on Climate Change, Cambridge, UK: Cambridge University Press, 2013.

[3] C. Van der Veen and ISMASS Members, "A need for more realistic ice-sheet models," *SCAR Report,* vol. 30, 2007.

[4] F. Rodriguez-Morales, S. Gogineni, C. Leuschen, J. Paden and a. others, "Advanced multifrequency radar instrumentation for polar research," *IEEE Transactions on Geoscience and Remote Sensing,* vol. 52, no. 5, pp. 2824-2842, 2014.

[5] A. Currie and M. Brown, "Wide-swath SAR," *IEE Proceedings F (Radar and Signal Processing),* vol. 139, no. 2, pp. 122-135, 1992.

[6] I. Ziskind and M. Wax, "Maximum Likelihood Localization of Multiple Sources by Alternating Projection," *IEEE Transactions on Acoustics, Speech and Signal Processing,* vol. 36, no. 10, pp. 1553-1560, 1988.

[7] D. J. Muson, J. O'Brien and W. Jenkins, "A tomographic formulation of spotlight-mode synthetic aperture radar," *Proc. IEEE,* vol. 71, no. 8, pp. 917-925, 1983.

[8] J. Mast and E. Johansson, "Three-dimensional ground penetrating radar imaging using multi-frequency diffraction tomography," *Proc. SPIE, Advanced Microwave and Millimeter-Wave Detectors,* vol. 2275, pp. 196-203, 1994.

[9] S. Valle, L. Zanzi and F. Rocca, "Radar tomography for NDT: comparison of techniques," *Journal of Applied Geophysics,* vol. 41, no. 2-3, pp. 259-269, 1999.

[10] J. Paden, T. Akins, D. Dunson, C. Allen and P. Gogineni, "Ice-sheet bed 3-D tomography," *Journal of Glaciology,* vol. 56, no. 195, pp. 3-11, 2010.

[11] X. Wu, K. Jezek, E. Rodriguez, S. Gogineni, F. Rodriguez-Morales and A. Freeman, "Ice sheet bed mapping with airborne SAR tomography," *IEEE Transactions on Geoscience and Remote Sensing,* vol. 49, no. 10, pp. 3791-3802, 2011.

[12] R. Schmidt, "Multiple emitter location and signal parameter estimation," *IEEE Transactions on Antennas and Propagation ,* vol. 34, no. 3, pp. 276-280, 1986.

[13] H. Van Trees, "Frequency Wavenumber Response and Beam Patterns," in *Optimum Array Processing. Part IV of Detection, Estimation, and Modulation Theory*, New York, John Wiley & Sons Inc, 2002, p. 34.

[14] M. Wax, T. Shan and T. Kailath, "Spatio-temporal spectral analysis by eigenstructure methods," *IEEE Transactions on Acoustics, Speech, and Signal Processing,* vol. 32, no. 4, pp. 817-827, 1984.

[15] H. Wang and M. Kaveh, "Coherent signal-subspace processing for the detection and estimation of multiple wide-band sources," *IEEE Transactions on Acoustics, Speech and Signal Processing,* vol. 33, pp. 823-831, 1985.

[16] E. Claudio and R. Parisi, "WAVES: Weighted average of signal subspaces for robust wideband direction finding," *IEEE Transactions on Signal Processing,* vol. 49, pp. 2179-2190, 2001.

[17] M. Agrawal and S. Prasad, "Broadbband DOA estimation using "spatial-only" modeling of array data," *IEEE Transactions on Signal Processing,* vol. 48, no. 3, pp. 663-670, 2000.

[18] B. Ottersten, P. Stoica and R. Roy, "Covariance Matching Estimation Techniques for Array Signal Processing Applications," *Digital Signal Processing ,* vol. 8, pp. 185-210, 1998.

[19] The MathWorks, Inc., *Optimization Toolbox: User's Guide,* Natick, MA: The MathWorks, Inc., 2015.

[20] M. A. Doron, A. J. Weiss and H. Messer, "Maximum-likelihood direction finding of wide-band sources," *IEEE Transactions on Signal Processing,* vol. 41, no. 1, pp. 411-414, 1993.

[21] S. Vogel, S. Tulaczyk, B. Kamb, H. Engelhardt, F. Carsey, A. Behar, A. Lane and I. Joughin, "Subglacial conditions during and after stoppage of an Antarctic Ice Stream: Is reactivation imminent?," *Geophysical Research Letters,* vol. 32, no. 14, 2005.

[22] H. Engelhardt and B. Kamb, "Videos of Basal Ice in Boreholes on the Kamb Ice Stream in West Antarctica," National Snow and Ice Data Center, Boulder, CO, 2013.

[23] R. Bamler and P. Hartl, "Synthetic aperture radar interferometry," *Inverse Problems,* vol. 14, no. 4, pp. R1-R54, 1998.

[24] H. Van Trees, "8.2 Maximum Likelihood and Maximum a posteriori Estimators," in *Optimum Array Processing. Part IV of Detection, Estimation and Modulation Theory.*, New York, John Wiley & Sons Inc., 2002, pp. 920-939.

[25] M. Zatman, "How narrow is narrowband?," *IEE Proceedings-Radar, Sonar and Navigation,* vol. 145, no. 2, pp. 85-91, 1998.

[26] A. Reigber and A. Moreira, "First demonstration of airborne SAR tomography using multibaseline L-band data," *IEEE Transactions on Geoscience and Remote Sensing,* vol. 38, no. 5, 2000.